
LAB-BASED IN-SITU X-RAY MICROSCOPY –
METHODICAL DEVELOPMENTS AND APPLICATIONS
IN MATERIALS SCIENCE AND MICROELECTRONICS

Von der Fakultät für Mathematik, Naturwissenschaften und Informatik
der Brandenburgischen Technischen Universität Cottbus

zur Erlangung des akademischen Grades

Doktor der Naturwissenschaften
(Dr. rer. nat.)

genehmigte Dissertation

vorgelegt von

Diplom-Ingenieur

Sven Niese

geboren am 28.04.1985 in Radebeul

Gutachter: Prof. Dr. Dieter Schmeißer
Gutachter: Prof. Dr. Ehrenfried Zschech
Gutachter: Dr. Gerd Schneider

Tag der mündlichen Prüfung: 30.04.2015

Kurzfassung

Die Methode der mikroskopischen Abbildung mittels Röntgenstrahlung und diffraktiven Linsen wurde an Synchrotronstrahlungsquellen entwickelt und kürzlich auf Geräte mit Laborquellen übertragen. Der erste Teil dieser Dissertation beschreibt die Herstellung, Charakterisierung und Anwendung von Multilayer-Laue-Linsen (MLL). Der zweite Teil beschreibt einen mikromechanischen *in-situ* Versuch, welcher benutzt wird, um die Rissausbreitung in geeignet präparierten Mikrochips mittels Röntgenmikroskopie in einem bruchmechanischen Experiment namens MicroDCB zu untersuchen.

Die MLL wurden durch mechanische Präparation und Focused-Ion-Beam-Bearbeitung aus WSi₂/Si-Multischichten hergestellt. Die Charakterisierung der Linsen mittels Rasterelektronen- und Röntgenmikroskopie erlaubt die Beurteilung der Qualität des gesamten Multischichtstapels sowie die Erfassung geometrischer Abweichungen einzelner Linsenelemente. Gekreuzte partielle MLL wurden als kompaktes Linsenelement für zweidimensionale Anwendung, d. h., Punktfokussierung von Synchrotronstrahlung oder Vollfeld-Durchlicht-Abbildung, zusammengesetzt. Die optischen Eigenschaften wurden mit je einem auf geometrischer Optik und auf Wellenoptik basierenden Modell simuliert. Die experimentellen Ergebnisse demonstrieren Vollfeldabbildung mit gekreuzten partiellen MLL in einem Labor-Röntgenmikroskop. Die Linsen haben eine Brennweite von 8,0 mm bei der Verwendung von Cu-K α Strahlung. Sub-100 nm Auflösung wurde erreicht und verbleibende Abbildungsfehler werden diskutiert. Keilförmige MLL weisen eine erhöhte Effizienz durch Ausnutzung von dynamische Beugung auf. Es wird eine Herstellungsmethode präsentiert, die eine nachträgliche geometrische Anpassung einer Einzellinse durch das Aufbringen einer verspannten Schicht erlaubt. Damit kann die keilförmige Geometrie unabhängig von der vorliegenden Multilagenbeschichtung erzielt werden. Der resultierende Kippwinkel der Schichten wurde mit Röntgenmikroskopie vermessen. Erste Untersuchungen solcher keilförmigen MLL mittels Synchrotronstrahlung bei $E = 15,25$ keV zeigen eine Erhöhung der Beugungseffizienz um 57 % gegenüber einer gekippten MLL mit gleichen Abmessungen.

Der lange Arbeitsabstand des Röntgenmikroskops vereinfacht die Integration von individuellen Vorrichtungen für *in-situ* Experimente. Der *MicroDCB*-Prüfer wurde entwickelt und gebaut um einen Riss in einem geeignet präparierten Untersuchungsobjekt voranzutreiben. Er ist kompatibel zu dem Röntgenmikroskop und erlaubt tomographische Untersuchungen unter Last. Die Methode wurde insbesondere auf die Untersuchung der Rissausbreitung in on-chip Verdrahtungsebenen von hoch entwickelten Mikrochips angewendet. Stabile Rissausbreitung innerhalb der Metallisierungsebenen wurde

erreicht. Dabei wurden Tomographien an mehreren Lastschritten durchgeführt. Die rekonstruierten Volumendatensätze zeigen keine kritischen Störungen. Es wird erwartet, dass dieser Versuch wertvolle Informationen bezüglich der Rissausbreitung in derartigen heterogenen Materialien liefert, was unter anderem bei Fragestellungen hinsichtlich der Zuverlässigkeit von Produkten der Halbleitertechnik von Interesse ist.

Abstract

The method of microscopic imaging using X-rays and diffractive lenses was developed at synchrotron radiation facilities and it was recently transferred to systems with laboratory X-ray sources. The first part of this thesis focuses on instrumentation, in particular on the fabrication, characterization, and application of multilayer Laue lenses (MLL). The second part describes a micromechanical *in-situ* test that is used to study crack propagation with X-ray microscopy in microchips in a dedicated fracture mechanics experiment called micro double cantilever beam test (*MicroDCB*).

MLLs were fabricated from WSi₂/Si multilayer coatings using mechanical preparation and focused ion beam milling. Initial characterization of the obtained lenses using scanning electron microscopy and X-ray microscopy was used to evaluate the quality of the multilayer stack and particularly to identify geometrical imperfections of individual lens elements. Crossed partial MLLs were assembled as a compact lens device for two-dimensional operation, i.e. point focusing of synchrotron radiation or full-field transmission imaging. The optical properties were simulated using a geometrical optics approximation and a physical optics model. Experimental results verify full-field imaging using crossed partial MLLs with a focal length of 8.0 mm for Cu-K α radiation in a laboratory X-ray microscope. Sub-100 nm resolution is shown and remaining aberrations are discussed. So-called wedged MLLs employ dynamic diffraction to increase the diffraction efficiency. A fabrication process is presented that allows a subsequent geometrical modification of the lens element using a stress layer. Thus, the wedged geometry is realized independently of the multilayer coating. The resulting layer tilt is measured using a laboratory X-ray microscope. First investigations of such wedged MLLs with synchrotron radiation at a photon energy $E = 15.25$ keV show an enhancement of the diffraction efficiency of 57% in comparison to a tilted MLL with the same dimensions.

The long working distance of the X-ray microscope facilitates the integration of customized equipment to perform *in-situ* experiments. The *MicroDCB tester* was designed and built to drive a crack in an appropriately prepared specimen. It is compatible with the X-ray microscope and it allows tomographic studies under load. In particular, the method was applied to investigate crack propagation in the on-chip interconnect stack of advanced microelectronics products. Stable crack propagation at this location was achieved. Subsequent tomographies were acquired at several load steps. The reconstructed datasets show no critical distortions. This test is assumed to provide valuable information about crack propagation such heterogeneous structures, what is of interest to address reliability issues.

Contents

1. Preface	1
2. X-ray microscopy	5
2.1. Limits of microfocus X-ray imaging	5
2.2. X-ray lenses for focusing and imaging applications	8
2.3. Laboratory-based transmission X-ray microscopy	13
2.4. Crack visualization by X-ray microscopy	15
3. Multilayer Laue lenses	23
3.1. State of the scientific knowledge	23
3.2. Fabrication and assembly of MLLs	24
3.3. Geometrical characterization of the multilayer stack and individual MLLs	32
3.4. Simulation of the optical properties	39
3.5. One-dimensional imaging with a single partial MLL	45
3.6. Full-field imaging with crossed partial MLLs	52
3.7. Characterization of MLLs using synchrotron radiation	59
3.8. Wedged MLLs	64
4. In-situ 3D investigations of crack propagation	73
4.1. Challenges of the mechanical stability of recent microelectronics products	73
4.2. Micro double cantilever beam test – MicroDCB	75
4.3. Experimental integration of the MicroDCB tester into an X-ray microscope	78
4.4. Specimen selection and preparation	81
4.5. Application to microelectronic products	86
4.6. Examples of further applications	96
5. Conclusions and outlook	99
A. Listings	103
B. Source codes	107
C. Technical drawings	121
Bibliography	125
List of publications	135

Contents

Curriculum Vitae	139
Danksagung	141
Erklärung	143

List of Figures

2.1. Microfocus X-ray imaging.	8
2.2. Fresnel zone plate, front view and cross section.	9
2.3. Comparison of optimal thicknesses along the optical axis for diffractive X-ray lenses.	11
2.4. MLL geometries for single MLLs.	12
2.5. Optical path of a laboratory X-ray microscope.	13
2.6. Mass absorption coefficient μ as a function of atomic number Z at 8.05 keV.	14
2.7. Comparison of contrast modes in XRM.	16
2.8. Optical path in Zernike phase contrast.	16
2.9. Description of contrast modes in XRM.	17
2.10. Computed tomography: acquisition of a projection $I_\theta(t)$	19
3.1. MLL apertures and focal lengths at 8.0 keV.	25
3.2. 1D scheme of a typical optical path of a scanning X-ray microscope.	26
3.3. Steps of the mechanical preparation.	28
3.4. FIB milling of a single MLL.	29
3.5. Crossed partial MLLs: model, SEM micrograph, and photograph.	31
3.6. Evaluation of a complete MLL.	32
3.7. Measured thicknesses of the multilayer stack for PS 6056 and PS 6359.	33
3.8. <i>ImageJ</i> plugin <i>Measure Layer Thickness</i> : demonstration at thick layers.	35
3.9. Results of the advanced SEM analysis to measure layer thicknesses.	35
3.10. Characterization of an MLL with laboratory XRM.	36
3.11. $\Delta\theta$ evaluation of an MLL comparing two FIB strategies.	38
3.12. Screenshot of <i>RayT</i>	40
3.13. The model for the physical optics simulation in case of a point source.	42
3.14. Simulation of 1D and 2D PSF.	44
3.15. Simulation of the effect of a drift during layer deposition.	44
3.16. Simulation of a focal series for an MLL of PS 6056 at 20 keV.	45
3.17. Photograph of the X-ray microscope <i>NanoXCT-100</i>	46
3.18. Tilt series of the MLL <i>5741-0</i>	47
3.19. First observation of the one-dimensional imaging capability of an MLL.	48
3.20. One-dimensional imaging of a grating with one MLL of lens <i>6056-C2</i>	49
3.21. Simulated image on the detector of a grating that is imaged with a complete or half cylindrical lens.	50

List of Figures

3.22. Vertical composition of individual images of both partial MLLs of a complete MLL.	51
3.23. Simulated images on the detector for imaging with crossed cylindrical lenses.	53
3.24. <i>RayT</i> simulations for imaging with crossed cylindrical lenses.	54
3.25. Bright-field image of crossed MLLs on the larger scintillating screen.	55
3.26. Radiographs of the center of the Siemens star test pattern <i>X50-30-0</i>	56
3.27. Radiographs of the test pattern <i>ATN/XRESO-50HC</i>	57
3.28. Radiographs of the center of the test pattern <i>ATN/XRESO-50HC</i>	58
3.29. SEM micrograph of the new test pattern for knife-edge scans.	61
3.30. Advanced evaluation of a series of knife-edge scans.	61
3.31. X-ray live camera images of MLLs.	63
3.32. Reconstructed PSF by ptychography of different crossed MLLs.	63
3.33. Modification of a flat MLL to a wedged MLL by deposition of a compressively stressed layer on one side.	65
3.34. Results of the FEA.	66
3.35. Fabrication and characterization of <i>6056-W1</i> and <i>6056-W2</i>	67
3.36. $\Delta\theta$ maps and line plots of two wedged MLLs.	68
3.37. Collections of images acquired with the X-ray live camera for three MLLs.	70
3.38. Intensity plots of X-ray camera images of <i>6359-SW2</i> and <i>6359-SF3</i>	71
4.1. SEM micrograph of a FIB cross section of a typical microprocessor chip.	73
4.2. Relationship of relative permittivity and mechanical properties of ILDs.	74
4.3. Drawing to illustrate a DCB test with asymmetric beams.	76
4.4. <i>DTS Delaminator</i> with DCB specimen.	78
4.5. Drawing of the MicroDCB test.	79
4.6. CAD drawings.	80
4.7. Photographs of the <i>MicroDCB tester</i> inside two X-ray microscopes.	81
4.8. Dicing pattern to prepare numerous specimens at once.	83
4.9. Drawing of a sandwich-like MicroDCB specimen.	83
4.10. Photograph showing the PAM with the <i>MicroDCB tester</i> and reverse-action tweezers.	85
4.11. Methods to notch a specimen.	86
4.12. High-resolution XRM investigations of microprocessors.	87
4.13. Comparison of potentially reconstructed circular cross sections of a MicroDCB specimen at tomographies with the 10 \times and 40 \times FZP.	88
4.14. Stitched image of a specimen inside the mount of the <i>MicroDCB tester</i>	90
4.15. Stitched radiograph of a MicroDCB specimen under load.	91
4.16. Projections of the tomography at different angles.	92
4.17. Four virtual cross sections of the reconstructed volume.	92
4.18. MicroDCB experiment at a sample of type B.	93
4.19. Tomography of the volume containing the crack front.	95

List of Figures

4.20. In-plane cross sections in the BEOL stack.	96
4.21. Nafion tear test at three load steps.	97
4.22. Bending test of a MEMS device using the <i>MicroDCB tester</i>	97

List of Tables

3.1. Used multilayer coatings and their properties.	27
3.2. Used parameters of the precision saw and for FIB milling.	28
3.3. SEM parameters to measure layer thicknesses.	34
3.4. Major parameters for the physical optics simulation.	43
3.5. Materials parameters used as input for FEA.	64
4.1. Measured displacement of the sample holder in dependence of the position of the piezo actuator.	80
4.2. Attenuation lengths l_{att} and index of refraction $n = 1 - \delta - i\beta$ at 8.05 keV of several materials [Gul10c; Gul10b].	81
4.3. Used parameters of the precision saw to prepare MicroDCB specimens and of the low pressure plasma system to clean their surfaces.	83
A.1. Overview of the fabricated MLLs.	103
A.2. List of beamtimes at synchrotron radiation facilities	105

Acronyms and symbols

ART	algebraic reconstruction technique
BEOL	back end of line
CAD	computer-aided design
CCD	charge coupled device
CMOS	complementary metal oxide semiconductor
CMP	chemical mechanical polishing
CT	computed tomography
CTE	coefficient of thermal expansion
DCB	double cantilever beam
EDF	ESRF data format
ESRF	European Synchrotron Radiation Facility
FEA	finite element analysis
FFT	fast Fourier transform
FIB	focused ion beam
FWHM	full width half maximum
FZP	Fresnel zone plate
IC	integrated circuit
ILD	interlayer dielectrics
MEMS	microelectromechanical system
MLL	multilayer Laue lens
NFL	nanofocusing lens
OSA	order selecting aperture
PAM	pre-alignment microscope
PETRA	Positron-Elektron-Tandem-Ring-Anlage
PIN	positive intrinsic negative
PSF	point spread function
SEM	scanning electron microscopy
TEM	transmission electron microscopy
ULK	ultra low-k
USB	universal serial bus
XRM	X-ray microscopy
XRR	X-ray reflectometry

List of Tables

X-ray physics and multilayer Laue lenses

β	see n
DOF	depth of focus
Δr_n	width of the n^{th} zone
$\Delta\theta$	relative layer tilt
δ	see n , or resolution
E	photon energy
f	focal length
η	1 st order diffraction efficiency
θ	angle
h	height of the multilayer stack of an MLL
I	intensity
λ	wavelength
M	magnification
μ	mass absorption coefficient
N	maximum zone number
NA	numerical aperture
n	refractive index, $n = 1 - \delta + i\beta$, or zone number (zone plate law)
r	radius (zone plate law), or radius (wafer)
ρ	density
σ	cross section
t	thickness of an MLL in beam direction
w	width of an MLL

MicroDCB

a	length of a crack
E	Young's modulus
F	force
G	energy release rate
G_c	critical energy release rate
h	height of a beam
I	second moment of area
κ, k	relative permittivity
ξ	ratio of the heights of both beams
o	opening of the crack at the mount
σ	mechanical stress
t	thickness of a beam

1. Preface

Since Röntgen discovered X-radiation in 1895 [Rön98], X-rays have been widely used in many areas of application in everyday life as well as in science and industry. X-ray diffraction patterns revealed both, that X-rays are part of the electromagnetic spectrum and the crystalline structure of many materials. Beside the development of diffractive and spectroscopic methods, a main application is imaging. Already Röntgen proposed to use microfocus X-ray tubes for radiographs with increased resolution. The interpretation of these transmission micrographs depends strongly on the investigated specimen. Simple objects with some distinct features are usually easy to identify. In case of complex structured specimens, a three-dimensional representation of the specimen is desired. Radon developed the mathematical principle called *Radon transformation* in 1917 to calculate the projection of a two-dimensional function and its inverse transformation [Rad17], which is the basis for computed tomography (CT). As this transformation is a computationally intensive task, it lasted to the availability of powerful computers, until CT was used for routine investigations, e.g. in medicine or for industrial process and quality control.

Existing X-ray micro-CT systems are based on a point-source projection of the object to an X-ray sensitive screen, which provides a primary magnification based on the intercept theorem. Therefore, the resolution of those systems is limited by the size of the X-ray source and the resolution of the detector system, reaching sub-micron resolution for dedicated systems. Using X-ray lenses to realize microscopy based on a real optical magnification, one can push the resolution down to tens of nanometers. Key requirements for this method are bright X-ray sources and precisely manufactured X-ray optics. Therefore, X-ray microscopy (XRM) was developed at synchrotron radiation facilities using Fresnel zone plates (FZP), which are typically patterned by electron beam lithography and subsequent etching. Due to these advanced prerequisites, XRM was developed rather late compared to visible light microscopy and electron microscopy. Hence, the achievable resolution in X-ray imaging is not diffraction limited according to the Abbe theorem, but it depends mainly on the available methods to fabricate such optics. A more comprehensive survey on the history of XRM can be found in [KJ09]. First dedicated XRM beamlines were installed around 1990 [Rar+90]. Laboratory systems using X-ray tubes with high-power rotating anodes became commercially available recently [Tka+06]. The studies of this thesis were mainly focused on laboratory X-ray microscopy using Cu-K α radiation.

Multilayer Laue lenses (MLL) are a recently published approach [Mas+04] to push the

1. Preface

achievable resolution of X-ray optics down to 10 nm and below, what allows more detailed materials investigations. The enhanced properties are achieved by a different procedure to fabricate the individual zones of the diffractive lens. To date published results show their application at synchrotron radiation facilities, where the incident X-ray beam is focused to a small spot for scanning transmission X-ray microscopy experiments. The equivalent in geometrical optics of a single MLL is given by a cylindrical lens. That means, two MLLs have to be crossed to obtain a two-dimensionally operating optics, which is comparable to a spherical lens. Both MLLs are typically mounted to different stages and subsequently aligned with respect to each other [Naz+13]. In this thesis, a different approach is presented in chapter 3 that consists of a compact assembly of both lenses. This device was integrated into a laboratory X-ray microscope and full-field imaging is shown. In addition, the X-ray microscope was used to characterize the fabrication process and the resulting quality of the MLLs using the built-in FZPs.

The diffraction efficiency can be significantly enhanced, if dynamic diffraction is employed. This means, all zones along the height of the multilayer stack have to fulfill the Bragg condition. Thus, the tilting angle of each zone has to increase linearly as a function of the height. This geometry can be achieved, if a strong gradient is incorporated during the deposition of the multilayer [Con+08]. A different approach is presented in this thesis, which employs an elastic deformation of a conventional flat MLL due to the application of a stress layer. This approach is expected to be more flexible, because the geometrical modification is independent of the present multilayer coating. The resulting tilt can be measured using the laboratory X-ray microscope with a similar approach as it was used to characterize flat MLLs.

✱

Almost every material that is used for a certain application contains flaws and cracks. Crack growth during the life cycle depends on applied loads, geometry, and materials properties itself. Fracture caused by an overload might result in an instantaneous breakage, and therefore, in a failure of the device. Among other things, this scenario is avoided if the device is correctly designed and fabricated, i.e. no critical flaws exist at the beginning. In case of fatigue, much smaller loads can cause crack growth to critical dimensions – e.g. in cyclic operation. Hence, the lifetime and consequently the reliability of the device is directly affected. The initial motivation investigating these questions of *fracture mechanics* was related to construction materials where failure can result in serious physical damage. The methods were later applied to functional materials and devices. In particular, leading-edge microelectronic products consist of a variety of materials, which are combined to a complex system. Hence, the propagation of cracks is directly influenced by the geometry of the stack and the materials used.

Crack propagation can be studied in well-known macroscopic tests at standardized specimens to obtain specific parameters such as the fatigue strength or the critical energy

release rate G_c [RHB08]. As a result, the distribution of the investigated parameter is obtained. In addition, a *post-mortem* analysis of the fractured surface might reveal details of the kind of crack propagation. Heterogeneous structures offer various options to influence or even stop crack propagation. Therefore, a direct *in-situ* observation is needed to understand the mechanism of crack propagation and the materials related impact. Respective non-destructive methods allow the three-dimensional structure of a crack to be imaged, which is buried in the volume of the specimen. In particular, X-ray microfocus radiography and tomography as well as ultrasonic testing are used for such experiments. X-ray microfocus tomography provides an isotropic spatial resolution down to about 1 μm . Ultrasonic testing is able to detect cracks with a significantly smaller opening. However, the lateral resolution is limited to few ten microns and the specimen must fulfill some conditions. The interpretation on heterogeneous specimens – in particular the differentiation between a crack and other interior interfaces – might be difficult, or interfaces with a large change in impedance may prevent any detection.

X-ray microscopy offers the capability to perform these experiments at a significantly better resolution. Hence, microcracks and crack tips can be directly observed and devices with sub-micron or even nano-scale features can be tested. In particular, the application of Zernike phase contrast highlights phase boundaries – and therefore cracks. The relatively large working distance of a laboratory X-ray microscope allows the integration of customized in-situ testing devices. A miniaturized set-up of the double cantilever beam test (DCB) was developed in this thesis to study crack propagation in an X-ray microscope: the *MicroDCB test*.

The characterization of microelectronic products is regarded as one application of this method. The non-destructive investigation of corresponding regions of interest offers new opportunities to support process development, as well as to identify and to localize defects. Crack propagation in the so-called back end of line (BEOL) stack of a chip – the on-chip wiring – can be studied with CT using the *MicroDCB tester*, which was developed in this thesis (chapter 4). Such studies are in particular of interest to evaluate damage mechanisms in on-chip interconnect stacks that can be critical regarding the reliability of the product. Particularly, recently introduced interlayer dielectric materials show worse mechanical properties as a side effect of a better electrical performance.

2. X-ray microscopy

This chapter provides an overview of different approaches to realize X-ray imaging. The basic principles of obtaining radiographs with conventional microfocus X-ray tubes are given in the first section. The application of X-ray lenses allows better resolutions as the point source projection is replaced by a true optical magnification, which is shown in section 2.2. In the subsequent section, the laboratory X-ray microscope is presented. Finally, two methods to investigate heterogeneous specimens and in particular cracks – computed tomography and Zernike phase contrast – are introduced. They are of particular relevance for the MicroDCB experiment (chapter 4).

2.1. Limits of microfocus X-ray imaging

X-rays are part of the electromagnetic spectrum in the high photon energy range beyond ultraviolet light and they overlap with gamma radiation to some extent. Unlike gamma rays that are generated at atomic nuclei, the origin of X-rays are electron or positron processes: strong acceleration and the decay of excited states of inner shells [Att99].

In general, accelerated charged particles such as electrons radiate electromagnetic waves. This is one basic principle of X-ray sources. Synchrotron radiation facilities are specialized electron or positron storage rings, which were developed from former instruments in particle physics as dedicated highly brilliant X-ray sources. A circulating electron or positron beam is routed through insertion devices, such as bending magnets or more advanced undulators and wigglers, where it is forced onto a sinusoidal path with high radial accelerations leading to an intensive X-ray emission. In X-ray tubes, which represent typical laboratory sources, electrons with a kinetic energy of several 10 keV are targeted to an anode material. The electrons are decelerated in the electric field of the atoms and emit the so-called bremsstrahlung in a continuous spectrum.

The second process is especially important for X-ray tubes, as the incident electrons may ionize the atoms by bouncing out inner shell electrons. The subsequent disexcitation leads to either the emission of an Auger electron or X-ray fluorescence in a discrete spectrum that is characteristic for the anode element. For instance if an electron of the L-shell fills up a vacancy of the K-shell, a $K\alpha$ photon is emitted corresponding to the common nomenclature. A further classification may be done based on the azimuthal quantum number to describe the splitting of e.g. $K\alpha_1$ and $K\alpha_2$ lines. Deploying this effect, X-ray tubes can be used to generate monochromatic radiation with a reasonable flux, if the desired photon energy is separated from the bremsstrahlung and other characteristic

2. X-ray microscopy

energies by using monochromatizing elements. However, available photon energies are limited to the characteristic radiation of some metals like copper, tungsten, molybdenum, and chromium, which are suitable anode materials.

The wavelength λ of a given photon energy E is equal to $\lambda = \frac{hc}{E}$, leading to the following conversation for practical purposes, thus

$$\lambda = \frac{1.24 \text{ nm}}{E/\text{keV}} \quad . \quad (2.1)$$

The *interaction of X-rays with matter* can easily be described as a transverse wave propagation of the electric field \mathcal{E} along \mathbf{x} , with \mathbf{k} being the wave vector:

$$\mathcal{E} = \mathcal{E}_0 \exp(i(\mathbf{k}\mathbf{x} - \omega t)) \quad . \quad (2.2)$$

The magnitude of \mathbf{k} is related to the complex refractive index n of the penetrated matter:

$$n = \frac{c}{\omega} k = 1 - \delta + i\beta \quad . \quad (2.3)$$

Due to the negligible refraction compared to visible light, the refractive index decrement δ usually describes the difference to 1 for the real part of n . With $\text{Re}(n) < 1$, total external reflection occurs at grazing incidence according to Snell's law. The imaginary part β describes the attenuation and is defined by the cross section of the photons with matter. Both quantities are connected by the Kramers-Kronig relations. In general, three processes contribute to the total cross section σ :

$$\sigma = \sigma_{\text{pa}} + \sigma_{\text{cs}} + \sigma_{\text{pp}} \quad . \quad (2.4)$$

Electron/positron pair production (σ_{pp}) requires photon energies of at least twice the rest mass of an electron $m_e c^2$ increased by some momentum transfer to the nucleus. Therefore, it is $\sigma_{\text{pp}} = 0$ for most X-ray applications. The photo absorption by electrons (σ_{pa}) is most important, yielding ionized atoms. It is obvious, that the photon energy must be greater than the ionization energy of the corresponding element with the atomic number Z for a selected electron. This leads to dedicated absorption edges. Beside those abrupt increases, the photo absorption cross section can be approximated by

$$\sigma_{\text{pa}} \propto Z^3 E^{-3} \quad . \quad (2.5)$$

Inelastic scattering of photons at weakly bonded electrons is called Compton scattering. It is especially important above 100 keV, as it can be deduced from the Klein-Nishina formula, which specifies its cross section σ_{cs} . The wavelength of the incident photon is changed by

$$\Delta\lambda = \lambda_{\text{C}}(1 - \cos\phi) \quad , \quad \lambda_{\text{C}} = \frac{h}{m_e c} = 2.43 \cdot 10^{-12} \text{ m} \quad . \quad (2.6)$$

2.1. Limits of microfocus X-ray imaging

with ϕ being the scattering angle and λ_C being the Compton wavelength of an electron.

Considering a *linear propagation through matter*, equation 2.2 results in an exponential decay of incident intensity I_0 (Beer-Lambert law):

$$I = I_0 \exp\left(-\int \mu \rho \, ds\right) \quad , \quad \mu = \frac{N_A}{\sum_i x_i A_i} \sum_j x_j \sigma_j \quad . \quad (2.7)$$

To apply it later to computed tomography, this notation [Tho+01] allows a variation of either the composition of matter, described by the atomic weight A and the mole fraction x , or its density ρ during transmission along a path s . N_A is the Avogadro constant. The *mass absorption coefficient* μ depicts one important applicable coefficient to describe X-ray absorption imaging. It is connected to the imaginary part of the refractive index:

$$\mu \rho = \frac{4\pi}{\lambda} \beta \quad (2.8)$$

A comprehensive collection of necessary coefficients for materials compounds as dependence of photon energies is provided on the website of the Center for X-ray Optics [Gul10c; Gul10b], which is based on tables by Henke et al. [HGD93].

Especially hard X-rays have the capability to penetrate all kinds of matter, what enables investigations of internal structures without any need for physical dissection of the specimen. The common way to obtain such a radiograph consists of the application of an X-ray tube and an appropriate detector using point projection of the specimen that is placed in between (Fig. 2.1). Formation of contrast is primarily given with the absorption of the bremsstrahlung along each ray. Especially materials science and engineering desires enhanced resolution, which is achieved using microfocus X-ray tubes. The electron beam is focused with additional magnetic lenses to a small spot onto the anode material in those devices. Therefore, the resolution of such lensless systems can be derived from geometrical considerations that involve the size of the X-ray focus F , the pixel resolution of the detector p , and the distances from the source to the object d_{SO} and from the source to the detector d_{SD} , respectively. The magnification M is given by

$$M = \frac{d_{SD}}{d_{SO}} \quad . \quad (2.9)$$

Schena et al. give an estimation for the best magnification of such a projection system [Sch+05a]:

$$M = \frac{2p}{F} + 1 \quad . \quad (2.10)$$

However, the practical limit of the resolution of those systems is little below $1 \mu\text{m}$ [Cnu+06; Bru+08; MG13]. Current area detectors for X-rays featuring high resolution are realized as scintillating screens that are imaged with a visible light microscope to a CCD detector. The resolution of this set-up is limited by the Abbe criteria for visible

2. X-ray microscopy

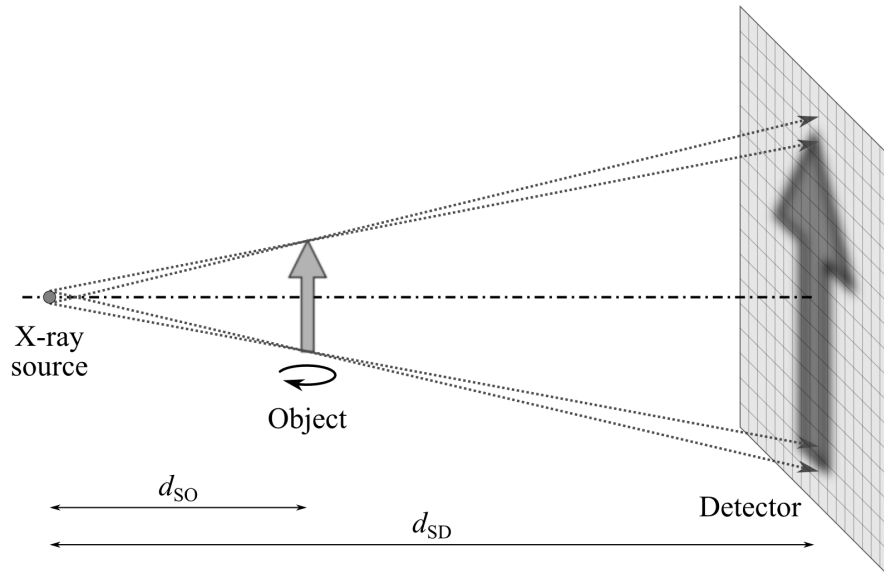


Figure 2.1.: Microfocus X-ray imaging: a magnified image of the object is projected to the detector (cone beam set-up).

light and the thickness of the scintillator that often leads to a trade-off between the shallow depth of focus of the microscope and a suitable quantum efficiency [Koc+98]. Though an electron beam can be focused to spot sizes of a single nanometer as known from scanning electron microscopes, one has to consider some further aspects for X-ray generation. The electron beam has typical depths of penetration of several microns and expands laterally with increasing depth due to scattering. Thin membranes of an anode material can be used to confine the X-ray source at lower X-ray yield. However, power density increases if smaller focus sizes are realized. Finally, such approaches are typically limited by the achievable X-ray intensity and the need to place the specimen at short distance to the potentially hot X-ray source [Wit07; Lal+13]. These limitations are avoided, if X-ray lenses are used for true optical imaging.

2.2. X-ray lenses for focusing and imaging applications

Several types of X-ray optics have been developed, which can be used for focusing and imaging applications [Wit07; SA10]. The X-ray source is typically demagnified to a secondary focus for scanning X-ray experiments. A line focus or a point focus is obtained, if the optic operates in one or two dimensions, respectively. X-ray mirrors in Kirkpatrick-Baez design [KB48] or Montel geometry [Mon57] may be used for this purpose. X-ray lenses such as Fresnel zone plates or compound refractive lenses can be used alternatively. In addition, they allow true optical full-field imaging of a specimen to a screen. One-dimensionally operating lenses are equivalent to cylindrical lenses in geometrical optics. Thus, two of them have to be aligned perpendicularly in series – or being *crossed* – to obtain a lens assembly that provides two-dimensional focusing or imaging.

Compound refractive lenses

Applying classical refractive lenses to X-rays is most often limited by an adverse ratio of refraction and extinction. A series of individual refractive lenses can act as a converging lens for hard X-rays at $E \gtrsim 10$ keV. Rotationally symmetric parabolic elements can be fabricated from aluminum or beryllium by a pressing technique [Len+99]. One-dimensionally operating lenses can be etched in silicon [Sch+03]. They are referred as nanofocusing lenses (NFL). In the latter case, a better control on the curvature allows smaller spot sizes, but two lenses with matched focal lengths have to be arranged perpendicularly in series to obtain a point focus.

Fresnel zone plates

Fresnel zone plates (FZP) represent the state-of-the-art X-ray lenses. They are fabricated by electron beam lithography and subsequent etching on a thin membrane that is typically coated with gold. The achievable aspect ratio can be enhanced, if zone plates are stacked [Fen+07; Wer+09]. They consist of a set of concentric rings, whose radii r_n follow the zone plate law (Fig. 2.2). The zone plate law can be deduced from geometric considerations for a *thin* FZP to realize phase shifts of π for adjacent zones due to different optical path lengths, if the X-ray source is located in infinite distance [Att99]:

$$r_n = \sqrt{n\lambda f + \frac{n^2\lambda^2}{4}} \simeq \sqrt{n\lambda f} \quad \text{if } f \gg \frac{n\lambda}{4} . \quad (2.11)$$

With $\lambda \propto E^{-1}$, it is $f \propto E$ for a given zone plate layout. Hence, an existing zone plate might be used at different photon energies, but it possesses a rather high chromatic aberration as well. Therefore, a monochromatic illumination is preferred. Simple zone plates for application with visible light are made out of alternately opaque and transparent materials to get constructive interference at the focus position of all rays passing

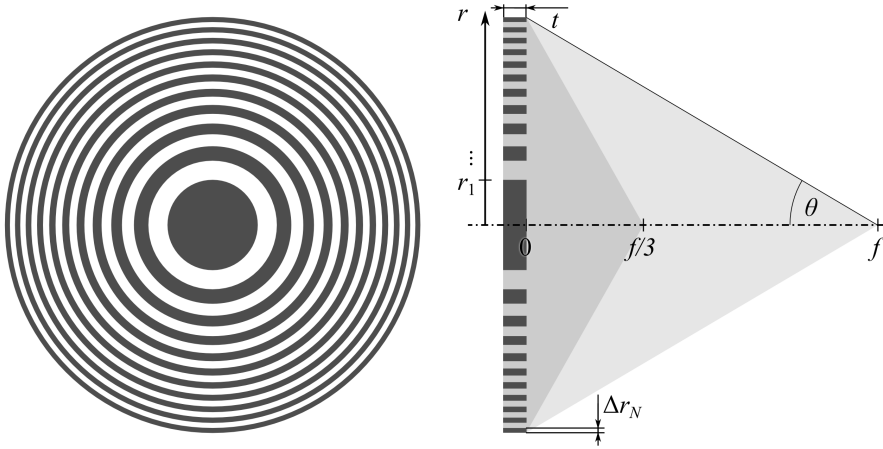


Figure 2.2.: Fresnel zone plate, front view and cross section with 3rd and 1st order focus at $f/3$ and f , respectively.

2. X-ray microscopy

the transparent zones. Beside this 1st order focus, higher order foci exist at shorter focal lengths. In general, only odd orders get intensity in case of a symmetric zone plate and negative – divergent – orders exist as well. The intensity of the m^{th} order focus equals $1/(m^2\pi^2)$. Thus, the efficiency for 1st order focusing and imaging is limited to about 10%, while only 1.1% can be expected in the 3rd order and 25% are transmitted in 0th order without being focused. Though the application of higher orders implicates an enhanced resolution, because the numerical aperture is increased as a consequence of the shorter focal length, such set-ups are limited to synchrotron radiation facilities to account for the low efficiency [Reh+09].

It is likewise possible to select both materials as well as the thickness t of the lens along the optical axis in such a manner, that incident rays obtain an additional phase shift of π at every second zone due to different refractive index decrements δ_1 and δ_2 :

$$\frac{\lambda}{2} = t_{\text{phase}} |\delta_1 - \delta_2| \quad . \quad (2.12)$$

Such FZPs that employ phase shifts are preferred, because opaque zones can hardly be realized for hard X-rays and they offer a larger effective aperture. This leads to an increase of the electric field at the focus by a factor of two and to four times larger intensities/efficiencies. Absorption and phase shift can be considered to optimize the efficiency even further and an ideal thickness that is slightly less than t_{phase} can be calculated as described in [Kir74].

The achievable resolution δ_{FZP} according to the Rayleigh criteria depends on the width of the outermost zone Δr_N , if all inner zones are present, i.e. those are existent and not blocked by e.g. a beamstop. The depth of focus DOF depends on the numerical aperture $\text{NA} = \sin \theta$ (cf. Fig. 2.2) and the wavelength [Att99], thus

$$\delta_{\text{FZP}} = \frac{0.610\lambda}{\text{NA}} = 1.22\Delta r_N \quad , \quad (2.13)$$

$$\text{DOF} = \pm \frac{\lambda}{2(\text{NA})^2} = \pm \frac{2(\Delta r_N)^2}{\lambda} \quad . \quad (2.14)$$

However, eq. 2.13 is valid for a *thin* zone plate with a round aperture. Real optics need to have a significant extent along the optical axis to satisfy eq. 2.12, what leads to volume diffraction effects if zone widths approach single nanometers. On the one hand, this is a limiting factor to the achievable resolution, because small foci can only be obtained with $t \ll t_{\text{phase}}$ at negligible efficiency or a significant broadening of the focus occurs [Yan+10]. On the other hand, diffraction at parabolically curved zones can be used to obtain local Bragg conditions [Sch06]. Such lenses do not limit the resolution. They allow an enhanced efficiency that exceeds the limits of thin zone plates. The zones act as a grating in Laue geometry, which has to be described by the theory of dynamic diffraction. Therefore, the optimal thickness is in this case dependent on the Pendellösung, with χ being the susceptibility of each material [Yan+10]:

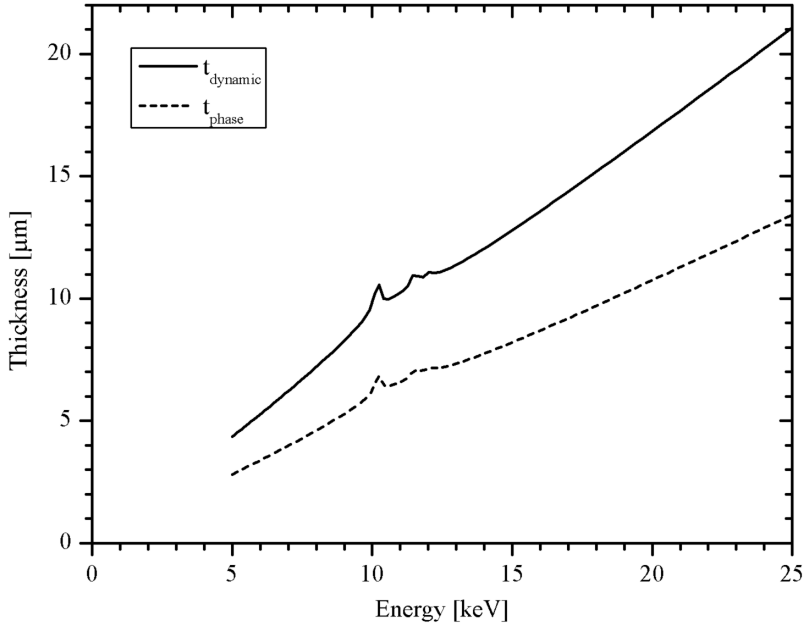


Figure 2.3.: Comparison of optimal thicknesses along the optical axis for diffractive X-ray lenses, based on phase shifts (t_{phase} , eq. 2.12) and volume diffraction (t_{dynamic} , eq. 2.15) for the WSi_2/Si system. Refractive indices are taken from [Gul10b].

$$t_{\text{dynamic}} = \frac{\pi \lambda}{2 |\chi_A - \chi_B|} . \quad (2.15)$$

Dynamic diffraction can only be deployed for thin zones with $\Delta r_n \lesssim 20 \text{ nm}$ [Yan+10]. Fig. 2.3 illustrates the different thicknesses that are needed to satisfy both approaches.

Multilayer Laue lenses

Multilayer Laue lenses (MLL) represent another class of diffractive X-ray optics [Mas+04]. MLLs are fabricated by thin film deposition as a multilayer stack with layer thicknesses satisfying eq. 2.11 on an appropriate flat or circular substrate, e.g. a silicon wafer or a wire. Subsequently, the actual lens has to be cut and thinned to the desired thickness in beam direction. This approach has several advantages over FZP fabrication. First of all, almost no layer thickness (zone width) limitation is of relevance to limit the resolution (eq. 2.13), because single nanometer thick layers can be deposited with high accuracy [MB06]. Second, aspect-ratio of individual zones is not bounded above. Especially for hard X-ray applications, optimal thicknesses (eqs. 2.12 and 2.15) can be realized to gain efficiency. Third, an MLL is realized as a compact stack with beneficial heat dissipation properties and long term stability compared to FZPs with free-standing zones.

A *single MLL*, which is obtained from a multilayer stack being deposited on a flat substrate, operates one-dimensionally. It corresponds to a cylindrical lens in refractive optics. Hence, two single lenses have to be assembled to *crossed MLLs* to obtain two-

2. X-ray microscopy

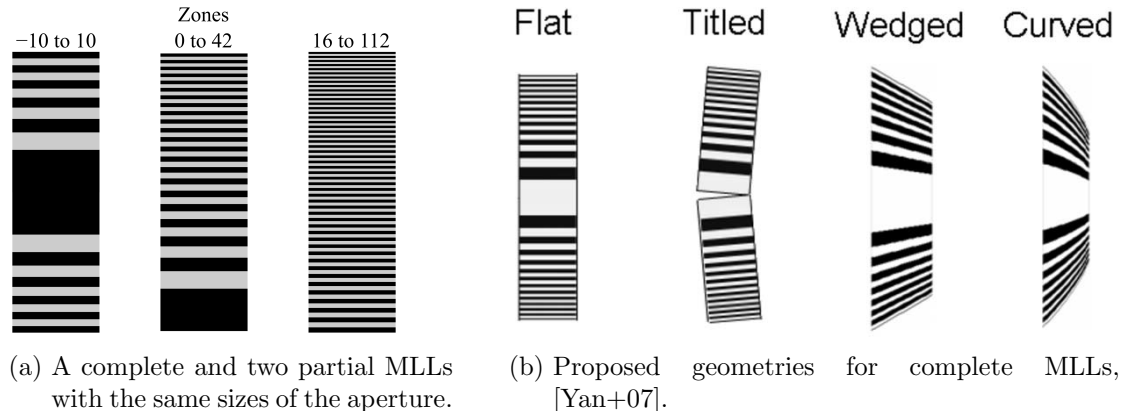


Figure 2.4.: MLL geometries for single MLLs: Complete and partial MLLs differ in the choice of the zone numbers. Flat, tilted, wedged, and curved MLLs differ in the geometrical arrangement of the zones with respect to the optical axis.

dimensional focusing or imaging [Mas+04]. In most cases, only one half of the multilayer stack starting at the thinnest zones and approaching the optical axis is fabricated on the substrate, and a *partial MLL* is obtained (Fig. 2.4a). This approach is related to manufacturing boundary conditions comprising the control of interface roughness, accumulated thickness drifts, and stress. Two of such *partial MLLs* can be assembled to a *complete MLL*, whose zones are symmetrically with respect to the optical axis [Liu+07].

The considerations regarding resolution and efficiency that have been presented for zone plates are valid for MLLs as well. The resolution in first order application is not directly connected to the width of the thinnest zone Δr_N in case of partial MLLs. The estimation based on the numerical aperture is slightly changed due to the rectangular aperture, yielding a value larger than $1.22\Delta r_N$ [Yan+10]:

$$\delta_{\text{MLL}} = \frac{0.50\lambda}{\text{NA}} \quad . \quad (2.16)$$

For example, it is $\delta_{\text{MLL}} = 2\Delta r_N$ for a partial MLL that is cut at the optical axis. To avoid negative impacts of volume diffraction on flat MLLs; tilted, wedged, and curved layer geometries are proposed [Yan+07; Kan+08], see Fig. 2.4b. A flat partial MLL does not differ physically from a tilted partial MLL. Thus, the tilted geometry can be realized with a proper alignment of the lens. Wedged and curved MLLs require a special geometry of the multilayer stack. This means, the geometry has to be made during fabrication of the lens [Con+08]. Both geometries assimilate, if the focal length is large compared to the thickness of the lens in beam direction ($f \gg t$).

Methods to fabricate circular MLLs¹ – i.e. a wire core is coated with a multilayer – are currently developed [RNS82; Kam+03; Koy+11]. Such lenses equal Fresnel zone plates with high-aspect ratios, if a section with a certain thickness is cut from the resulting

¹sometimes referred as multilayer zone plates

wire. However, their fabrication is more challenging than the fabricated of MLLs due to the requirement of almost perfectly round wires and expected accumulations of flaws of the deposition process, once the outermost – thinnest – layers are reached.

2.3. Laboratory-based transmission X-ray microscopy

Major parts of the studies of this thesis involved a *NanoXCT-100* (*Xradia Inc.*, Pleasanton, CA, USA²). It is the first and – including its successor – to date only commercially available full-field transmission X-ray microscope for laboratory usage. Other X-ray microscopes are set-up at synchrotron radiation facilities for scanning and/or full-field transmission X-ray microscopy. In general, XRM at photon energies $E \gtrsim 2$ keV is referred as hard X-ray microscopy, which is the focus of this thesis. Soft X-ray microscopy has particular requirements, for instance regarding sample preparation and vacuum, which it is of special interest for investigations of soft matter [Att99; Gut+13].

The rotationally symmetric optical path of the microscope is shown in Fig. 2.5. As it is well known from visible light microscopy, it can be divided in an illumination system – consisting of light source, condenser, and apertures – and the imaging system, which images the object with a lens to a scintillating screen.

The illumination system has to satisfy three requirements: First, the field of view inside the object plane needs to be uniformly illuminated with sufficient intensity. Second, no direct beams of the illumination have to hit the screen, because zero-order beams that pass the zone plate straight would otherwise create background. Third, monochromatic radiation is preferred to suppress chromatic aberrations.

²since July 2013 *Carl Zeiss X-ray Microscopy Inc.*, Pleasanton, CA, USA

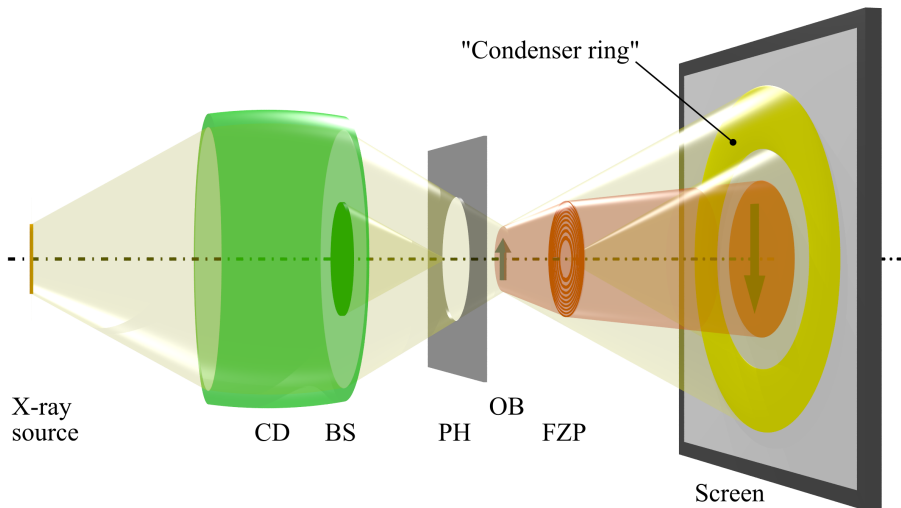


Figure 2.5.: Optical path of a laboratory X-ray microscope. Not diffracted X-rays are shown in yellow, diffracted X-rays are shown in orange. CD – condenser, BS – beamstop, PH – pinhole, OB – object, FZP – Fresnel zone plate.

2. X-ray microscopy

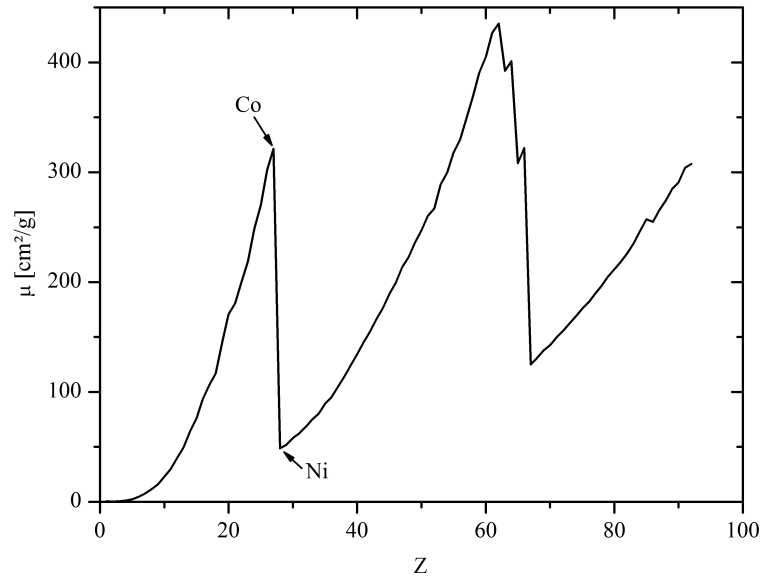


Figure 2.6.: Mass absorption coefficient μ as a function of atomic number Z at 8.05 keV. Data taken from [HS96].

Integral part is a capillary condenser, whose inner surface follows a rotational ellipsoid. It transfers the X-ray source focus by external total reflection to the object plane in equal size [YDW07]. Hollow cone illumination is realized in combination with a beamstop and a pinhole to block remaining direct beams from the source. Hence, the size of the X-ray focus needs to be as large as the field of view, which equals $(67\ \mu\text{m})^2$. An X-ray tube with a rotating anode is chosen to ensure a large flux of photons. Copper and chromium are currently available anode materials. Their $K\alpha$ lines at 8.05 keV and 5.41 keV, respectively, are chosen for X-ray imaging.

Moderate monochromatization is realized by the capillary condenser that cuts off photon energies well above the selected energy, whereas soft X-rays are absorbed by air along the beam path. A $K\beta$ filter – a thin Ni foil – can be used to advance the ratio of $K\alpha$ to $K\beta$ intensity. Remaining bremsstrahlung will be defocused and adds to the background intensity of the radiographs.

The system includes two FZPs with focal lengths of 18 mm and 75 mm, and corresponding fields of view of $16.5 \times 16.5\ \mu\text{m}^2$ and $66.5 \times 66.5\ \mu\text{m}^2$. The actual image on the scintillating screen has a size of $680 \times 680\ \mu\text{m}^2$. Thus, the respective magnifications are approximately $40\times$ and $10\times$. The image is subsequently magnified by a visible light microscope to a 1024×1024 px CCD camera. There is another, ten times larger scintillating screen for system alignment purposes. It shows the not diffracted part of the hollow cone illumination as a ring encircling the FZP image, henceforward called *condenser ring* (cf. Fig. 2.5).

The presented set-up can be used for acquisition of radiographs assuming parallel beam imaging. Contrast formation is defined by absorption of incident X-rays according

to the Beer-Lambert law (eq. 2.7). The fixed photon energy of the system involve some constraints compared to microfocus X-ray systems and X-ray microscopes at synchrotron beamlines with variable photon energy that have to be accounted in specimen selection and preparation. Albeit photon energies above 2 keV are usually denominated as *hard X-rays* in XRM, the method is still operating in the region of absorption edges of relevant elements. This fact is exploited in abnormal imaging in synchrotron XRM, taking at least two radiographs slightly above and below an absorption edge. The difference in absorption is then mainly defined by the presence of the selected element. However, absorption properties at fixed photon energies are constant as well. The mass absorption coefficient as a function of atomic number at 8.05 keV (Cu-K α radiation) is shown in Fig. 2.6. Its strong variation causes significant changes in the attenuation length for different materials.

The contrast of light materials can be enhanced by *Zernike phase contrast* if an annular phase plate is placed in the rear focal plane [SRG88]. This imaging mode is also used to highlight phase boundaries such as cracks. Its application will be described in the next section.

2.4. Crack visualization by X-ray microscopy

Radiographs image the attenuation of X-rays that transmit the object. Features that are extended in three dimensions can easily be detected, if their size is larger than the resolution. A tomographic investigation might be necessary, if the object has a complicated heterogeneous structure. Crack propagation in such specimens will be investigated in the *MicroDCB* studies presented in chapter 4. Cracks are typically small compared to the size of the specimen and primarily characterized by interfaces. On the one hand, microcracks can be resolved due to the better resolution of X-ray microscopy compared to microfocus X-ray imaging. Furthermore, the application of Zernike phase contrast enhances the crack visualization.

Zernike phase contrast

As already mentioned, there is a second imaging mode beside absorption contrast available. It is called Zernike phase contrast. Its theory was developed by Frits Zernike [Zer35; Zer55]. This method was first established in biology and medicine to image objects that appear transparent or homogeneous in conventional visible light microscopy [KL41]. The method was later transferred to XRM [SRG88; Tka+06]. It is in particular beneficial for this study to increase the visibility of cracks. In principle, adjacent regions with a different refractive index are imaged with an increased intensity. Thus, cracks will get decorated due to the abrupt change of electron density and consequently the refractive index at the interface air/material. Fig. 2.7 shows a crack inside a silicon

2. X-ray microscopy

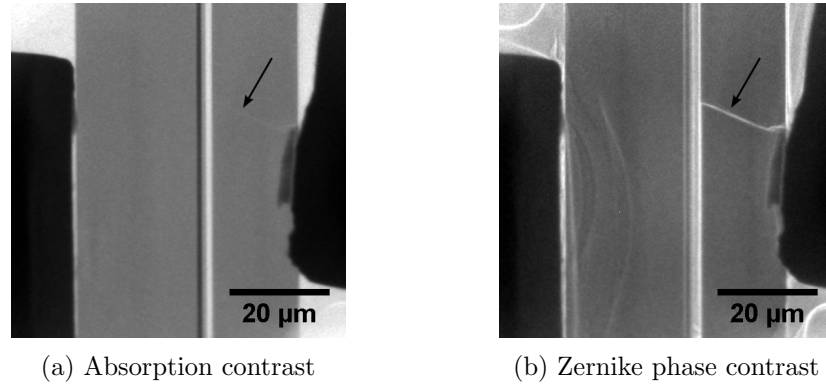


Figure 2.7.: Comparison of contrast modes in XRM. The arrow in each radiograph points to a crack in the vertically oriented silicon beam, which is highlighted in Zernike phase contrast.

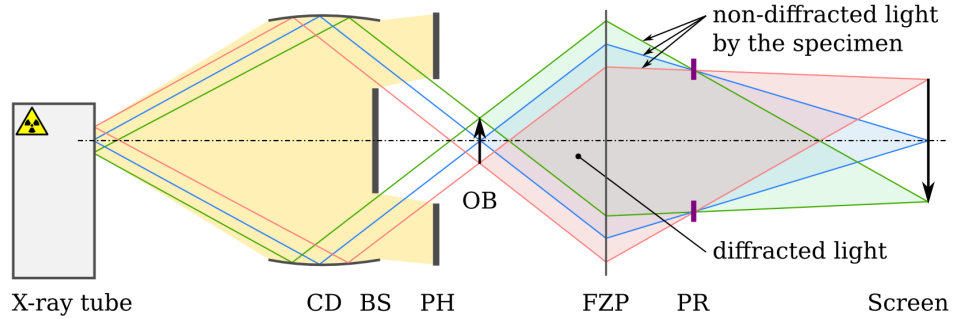


Figure 2.8.: Optical path in Zernike phase contrast. CD – condenser, BS – beamstop, PH – pinhole, OB – object, FZP – Fresnel zone plate, PR – phase ring.

beam in a failed MicroDCB experiment. Its visibility is significantly enhanced, if Zernike phase contrast is used.

The origin of Zernike phase contrast will now be briefly discussed. Fig. 2.8 shows schematically the optical path of a laboratory X-ray microscope. A hollow cone illumination is mandatory to separate the image from zero-order beams at the image plane, because diffractive lenses show a limited efficiency. Fortunately, this special type of illumination is also required for Zernike phase contrast³. An annular phase plate (“phase ring”) is placed in the rear focal plane and centered with respect to illumination and FZP. It typically attenuates transmitted X-rays and retards their phase by $\pi/2$ to obtain positive phase contrast. If no object is present, all light passes the phase ring and a regular bright field is obtained in the image plane. Its intensity is reduced to approximately 50% due to the attenuation of the phase ring. X-rays are scattered if an object is placed inside the optical path. Some fraction of the light that was perceptibly scattered will not pass the phase ring, and therefore, no additional phase shift occurs. The FZP acts as a collecting lens. Thus, all light that was emitted from a certain position at the object plane will be focused to the corresponding position at the image plane and both

³Although in this case a special phase contrast condenser is used. The hollow cone is more confined at lower X-ray flux in comparison to the use of the absorption contrast condenser.

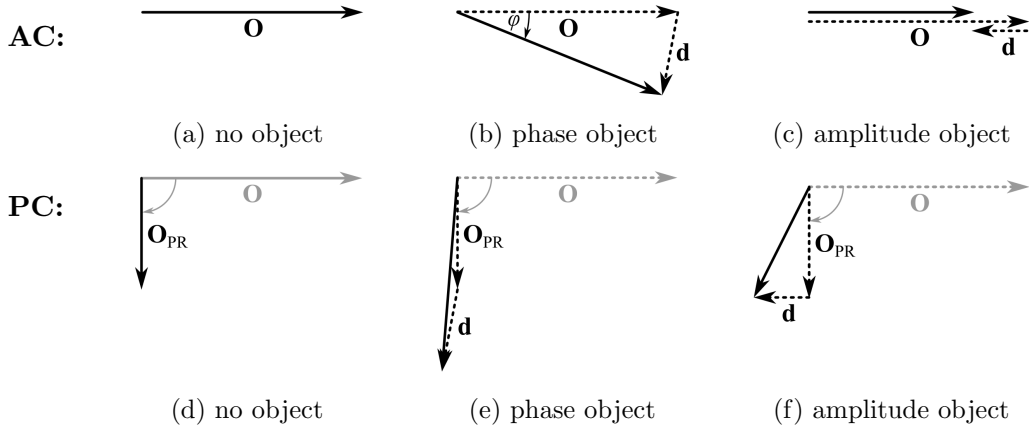


Figure 2.9.: Description of contrast modes in XRM: each wave is represented as a vector in polar coordinates. The resulting vector is drawn with a solid line for absorption contrast (AC) and Zernike phase contrast (PC). Vector decomposition is drawn as a dashed line. \mathbf{O} refers to zero-order, \mathbf{d} to diffracted light (sum of all higher orders). Zero-order light \mathbf{O}_{PR} is attenuated and retarded by $\pi/2$ due to the phase ring. Adapted from [KL41].

parts of the wave eventually interfere there.

The origin of phase contrast is best understood, if Fourier optics and Fraunhofer diffraction are considered. The hollow cone illumination leads to an off-axis incidence of each ray into the object plane. Those rays are transferred to a certain radius in the rear focal – Fourier – plane, according to their angle of incidence with respect to the optical axis. This area is covered by the phase ring. Any object causes Fraunhofer diffraction and other orders than the previously described zeroth order occur and they are scattered to other directions, passing the rear focal plane elsewhere. Zernike suggested to decompose any wave that is emitted from a position in the object plane in a zero-order component \mathbf{O} describing the bright field, and a second component \mathbf{d} that contains the information about the influence of the object regarding phase and amplitude changes, i.e. the sum of all other orders.

An illustration containing vector representations is shown in Fig. 2.9. No higher orders occur if no object is present (Fig. 2.9a) and the observed intensity equals the length of \mathbf{O} . The incoming wave gets a phase shift by φ in case of a pure phase object (Fig. 2.9b) and \mathbf{d} is oriented almost perpendicular to \mathbf{O} . Both vectors are antiparallel for a pure amplitude object (Fig. 2.9c). Though \mathbf{d} is non-zero in both latter cases, a contrast is just observed if the length of the resulting vector is changed, i.e. in case of the amplitude object.

The additional phase ring exclusively affects \mathbf{O} in amplitude and phase. The resulting vector is \mathbf{O}_{PR} (Fig. 2.9d). Vector addition with the corresponding \mathbf{d} vector of the phase object and amplitude object yields different resulting vectors in case of Zernike phase contrast. In particular, an increased length is observed for the phase object (Fig. 2.9e). The enlargement equals the length of \mathbf{d} being proportional to the phase shift of the

2. X-ray microscopy

object for small φ .

Thus, Zernike phase contrast visualizes phase shifts due to the object. However, the recorded intensity is not strictly characterized by this effect in case of an extended pure phase object. This is most probably caused by the fact, that the hollow cone illumination features a certain distribution of angles of incidence and that the phase ring has to have a certain width. Lower orders of the Fraunhofer diffraction pattern are as well influenced by the phase ring, leading to a short range effect being especially effective at phase boundaries rather than the center of an extended homogeneous area. This artifact is known as shade-off [Mur+].

The final radiograph is still characterized by absorption contrast. It is overlaid by effects of Zernike phase contrast, highlighting areas with different refractive indices. Hence, the measured intensity at a certain position is also affected by its vicinity. The theoretical assumptions of tomography are therefore not fulfilled. However, tomographic reconstructions typically yield decent results and “artifacts” caused by phase contrast are well restored in the three-dimensional representation of the object. Radiographs and tomographic reconstructions can therefore not easily be quantified without prior knowledge of the specimen, and a simple threshold operation to separate different phases will not be productive. But such radiographs are typically easy to interpret for humans and regions with different phases can be identified.

Computed tomography

It is the nature of transmission microscopy that the information – i.e. the measured intensity – at each position inside a radiograph is a projection of all features that the corresponding ray passed during its way through the object. The analysis of a single radiograph will not be sufficient to get a requested information in many cases, because several features are superimposed and cannot be distinguished. In some cases, it is possible to shrewdly orient the specimen with respect to certain features and to acquire radiographs with different views. For example, this is done in medical application where two orthogonal views are taken to analyze an injured bone or joint. If this approach does not yield satisfying results, a more sophisticated analysis like computed tomography (CT) is used. Here, a large number of projections at several angles are recorded and complete cross sections of the object are reconstructed with dedicated algorithms. It may be remarked at this point, that radiographs visualize the transmitted intensity according to custom in materials science. Any object appears dark with respect to its attenuation. CT reconstructs the attenuation coefficient. Thus, any object appears bright with respect to its attenuation, and the contrast appears somehow inverse.

A comprehensive introduction to principles of CT is given in [KS88]. Each XRM image equals a parallel beam projection of the object due to the application of an X-ray lens. This is one major difference to X-ray microtomography, where a cone beam projection is present. Each image is discretized in pixels with n_y rows and n_x columns.

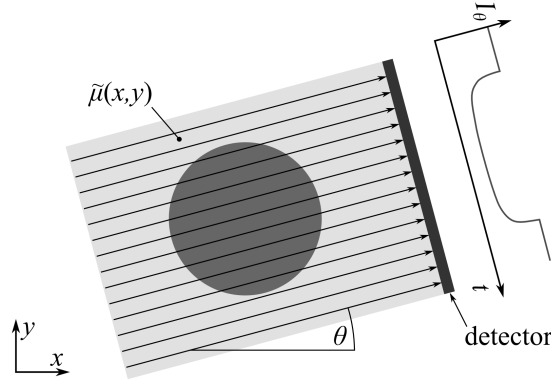


Figure 2.10.: Computed tomography: acquisition of a projection $I_\theta(t)$.

Typically, a semi circle or full circle is scanned with a constant angular step size for each angle θ . Here, the rotational axis is oriented vertically with respect to the image. The reconstruction will be performed for each row of all images separately, corresponding to a single slice of the resulting reconstructed volume.

The following derivation of the line integral $P_\theta(t)$ is based on eq. 2.7. A slice is described with a Cartesian coordinate system (x, y) . Mass absorption coefficient μ and density ρ can be combined for simplification to

$$\tilde{\mu}(x, y) = \mu(x, y)\rho(x, y) \quad . \quad (2.17)$$

Hence, the intensity along a row of a projection is given by line integrals for each position t , thus

$$I_\theta(t) = I_0 \exp \left[- \int_{(\theta,t)\text{line}} \tilde{\mu}(x, y) \, ds \right] \quad . \quad (2.18)$$

The equation can be rewritten in the following way:

$$P_\theta(t) = - \ln \frac{I_\theta(t)}{I_0} = \int_{(\theta,t)\text{line}} \tilde{\mu}(x, y) \, ds \quad . \quad (2.19)$$

$P_\theta(t)$ is a Radon transform of $\tilde{\mu}(x, y)$. Johann Radon showed already in 1917 that $\tilde{\mu}(x, y)$ can be found with an inverse transform [Rad17]. However, this requires an extensive computation and practical applications require modern computer systems that had not been available for decades. The reconstruction can be accelerated, if the *Fourier slice theorem* is used. It states that the one-dimensional Fourier transform of a projection $P_\theta(t)$ of a two-dimensional function equals the intensity along a line through the origin of the two-dimensional Fourier transform of the function, if the line is parallel to the projection. Hence, the function can then be estimated with an inverse two-dimensional Fourier transform, if enough projections are known.

The Fourier transform of the projection is in general given by

2. X-ray microscopy

$$S_{\theta}(w) = \int_{-\infty}^{\infty} P_{\theta}(t) \exp(-2\pi i w t) dt \quad , \quad (2.20)$$

with w being the frequency. As already mentioned, the original data is discretized into pixels. Thus, fast Fourier transform (FFT) operations can be used to efficiently calculate the discrete Fourier transform. Kak and Slaney list the following steps to eventually perform the reconstruction of a single slice [KS88]:

- Sum for each of the K angles, θ , between 0 and 180°
 1. Measure the projection, $P_{\theta}(t)$
 2. Fourier transform it to find $S_{\theta}(w)$
 3. Multiply it by the weighting function $2\pi|w|/K$
 4. Sum over the image plane the inverse Fourier transforms of the filtered projections (the backprojection process).

The weighting process in step (3) is necessary to compensate for the change from the polar coordinate system of $S_{\theta}(w)$ that is directly being backprojected to a Cartesian coordinate system in this procedure – i.e. the data is filtered in Fourier domain. Therefore, this method is often referred as *filtered backprojection*. It is possible to modify the filter to achieve a smoothing of the reconstructed data. E.g., the linear wedge filter can be multiplied with a Gaussian function that will damp higher frequencies and it will therefore reduce noise. This function is often called *apodization function*.

At first glance, it is not obvious why the backprojection step is preferred to a direct inverse two-dimensional Fourier transform of the processed slice. A fundamental reason according to Kak and Slaney is the reduction of artifacts, if the necessary interpolation is performed in space domain rather than Fourier domain. Another advantage is given by the fact, that each single line projection $P_{\theta}(t)$ is backprojected individually into the volume. Hence, it is not necessary to compose the complete two-dimensional Fourier transform of any slice at any time. This is important for different scanning geometries like cone beam projection or a tilted rotational axis to investigate flat specimens [Krü+11; Hel+04]. Rays cross several slices in those cases and an assignment of $S_{\theta}(w)$ to a single slice is not easily possible. Last but not least, it is possible to do an *online reconstruction*. In this case, the processing of each projection can immediately start after its acquisition and the reconstructed volume will be available almost directly after all projections are measured [Krü14].

Two software packages are used to perform the reconstruction. *XMReconstructor 9.0* (*Xradia Inc.*, Pleasanton, CA, USA) is shipped with the X-ray microscope *NanoXCT-100*. It uses a proprietary algorithm that is assumed to basically implement an enhanced version of the algorithm described above. The Yorick [Mun10] library *reko.i* was provided to the author as source code [Krü14]. It is a direct implementation of the presented

2.4. Crack visualization by X-ray microscopy

algorithm. It serves as a verification of the commercial algorithm and can easily be extended to realize new features, such as a tilted rotational axis [Krü+11].

Filtered backprojection is a powerful method to numerically solve the inverse Radon transformation. The method is quite robust, i.e. it is not especially sensitive to noise. It does not require prior knowledge of the specimen, making it a universal approach for reconstruction. On the other hand, it requires a complete sampling of the object in terms of signal processing – leading to a large number of projections. Existing knowledge of the specimen cannot be used to improve the reconstruction. For example, if the specimen consists of few homogeneous phases like a matrix, another randomly distributed material, and pores/air, it makes sense to confine the values of $\tilde{\mu}(x, y)$ to three distinct values rather than allowing arbitrary numbers. *Algebraic algorithms* – e.g. the algebraic reconstruction technique (ART) [KS88; Ban08] – are iterative methods to numerically solve this problem in space domain. They can take advantage of prior knowledge and it was shown, that it is in principle possible to reduce the amount of data that is needed for reconstruction (e.g. [BS07]).

In any case, it is a necessary condition that all projections are properly aligned, i.e. each radiograph is centered with respect to the rotational axis and the vertical position of the object is kept constant. Unlike for X-ray microtomography, the resulting XRM dataset does not fulfill this condition. XRM based tomography is therefore facing similar issues like TEM based tomography in consequence of the high resolution and limited accuracy of all mechanical components [Ban08]. It is assumed for XRM, that the angle of rotation of the object has a negligible error and that the rotational axis is oriented vertically with respect to the radiograph. Hence, the correction reduces to vertical and horizontal translations of each projection. A marker – e.g. a small spherical gold particle –, which is put onto the surface of the specimen, is typically used to determine the offsets. Currently, there are two methods available to perform the alignment. First, *XMController* allows any distinct feature to be manually tracked. Its center has to be defined with the cursor by a simple “point and click” procedure. The obtained positions are then fitted to a virtual sinusoidal movement and deviations are used as corrections. Second, an ImageJ [Ras13] plugin called *Bead Aligner* [KN13] features a semi-automated tracking of particles. The center of gravity of the particle is automatically determined in each projection. Manual assistance and correction is supported if the algorithm fails. Resulting offsets can be directly written to the *TXRM* file⁴.

⁴The TXRM file format is used by Xradia to store all projections of a tomography and its metadata (e.g. axis positions and exposure times) in a single data file.

3. Multilayer Laue lenses

Multilayer Laue lenses (MLL) are a novel type of diffractive lenses that are especially applicable for hard X-rays. Their technological advantages compared to Fresnel zone plates (FZP) are summarized in chapter 2.2. These novel X-ray optics are still in early development. Therefore, research has been focused on their feasibility to act as focusing optics at synchrotron radiation facilities.

In this thesis, contributions are made to the development of MLLs for application in scanning XRM. It will further be shown that MLLs can be used in full-field XRM. An approach to realize wedged MLLs is presented as well.

3.1. State of the scientific knowledge

The major advantage of MLLs compared to FZPs is the absence of any aspect-ratio limitation even for very thin individual zones, promising higher efficiencies and better resolutions in particular for hard X-rays. But there are at least two issues that have to be solved to obtain optics with enhanced capabilities. The first issue is related to the height of the multilayer stack that defines the absolute aperture of the lens. Recently published apertures are rather small what implicates short focal lengths to realize appropriate nano foci. Second, wedged or even curved layer geometries have to be fabricated to exploit their full potential in terms of efficiency and to obtain foci in a single-digit nanometer range.

In this sense, lenses for hard X-rays might be ranked on the basis of various properties and this paragraph summarizes current experimental results. The focal diameter is the most obvious quantity. Hard X-rays have been focused to a 7 nm line focus at 20 keV with X-ray mirrors and an in-situ wave-correction approach [Mim+09] and recently to an 11 nm line focus at 12 keV with an MLL [Hua+13]. In terms of two-dimensional focusing or imaging, 5 nm were demonstrated with a combination of a Kirkpatrick-Baez mirror and a multilayer zone plate with an ultra-short focal length of 50 μm [Dör+13], 20 nm resolution in full-field imaging have been demonstrated with FZPs [Che+11], a $25 \times 40 \text{ nm}^2$ focus was obtained with crossed MLLs [Yan+11], and crossed compound refractive lenses obtained $47 \times 55 \text{ nm}^2$ [Sch+05b]. The latter ones can be improved with an adiabatically focusing geometry, i.e. the aperture of the serial lenses is subsequently adjusted to the diameter of the beam. In this case, a focus size of 2 nm is expected [SL05] and 17 nm were demonstrated [Pat+12]. However, the actual focus is located in close distance to the exit of such a lens. Hence, this approach is currently limited to improve

3. Multilayer Laue lenses

the resolution in one focusing direction unless rotationally symmetric lens elements can be fabricated.

The eventual working distance is an important parameter for experiments. Small values might result in additional restrictions to sample size or to the opportunity to use additional equipment such as in-situ devices or environmental chambers. Naturally, the working distance w is restricted by the focal length f . The working distance is decreased if an order selecting aperture (OSA) downstream the lens has to be used [YC12], or if the lens itself has a significant extent along the optical axis in case of compound refractive lenses or some MLLs with very short focal lengths [Ruh+12; LRK10; Kan+08]. Finally, the total flux at the focus position, side lobes of the focus as well as other parasitic radiation increasing background, and the depth of focus have to be considered. Durability and efforts for adjustment are of practical relevance.

Fig. 3.1 summarizes published apertures and focal lengths of several MLLs until the begin of the year 2012, when the experiments with MLLs presented in this thesis started. For the purpose of comparison, all focal lengths are converted to a photon energy E of 8.0 keV (eq. 2.11). It is obvious that no aperture exceeds 13 μm , what is small against typical sizes of FZPs, which can have diameters $\geq 100 \mu\text{m}$. The size of the laterally coherent area of the beam of a 3rd generation synchrotron radiation source is in the order of 150 μm . Therefore, a major part of the usable radiation needs to be blanked and the overall yield of such a lens is intrinsically low, though it might have a good efficiency related to its aperture. Most MLL designs have a very short focal length to be able to get sizes of the focus better than 30 nm. No publication is known to the author showing that MLLs are applicable as lenses in full-field X-ray microscopy.

Hence, the preparation of MLLs with large apertures and applicable focal lengths is a major aim of this working group. Apertures of three of our multilayer depositions are shown for comparison in Fig. 3.1. It may be noted, that an MLL with a comparable size of the aperture of 43.4 μm was published recently [Hua+13].

3.2. Fabrication and assembly of MLLs

The fabrication of MLLs is based on thin film deposition of alternating layers of two different materials with different refractive indices onto an atomically flat substrate. The thickness of those layers is given by the zone plate law (eq. 2.11). The choice of lens parameters and materials is influenced by many factors, such as desired resolution, working distance, global diffraction efficiency, and manufacturing requirements. Those considerations were mainly conducted by Dr. S. Braun and A. Kubec (*Fraunhofer IWS Dresden*, Germany, [KB14]) who delivered the multilayer coatings. They will be discussed briefly in the next subsections. A single MLL is then fabricated with mechanical preparation and focused ion beam (FIB) milling. Scanning electron microscopy (SEM) is used to monitor the preparation. Finally, two of these single MLLs can be assembled to crossed MLLs or a complete MLL.

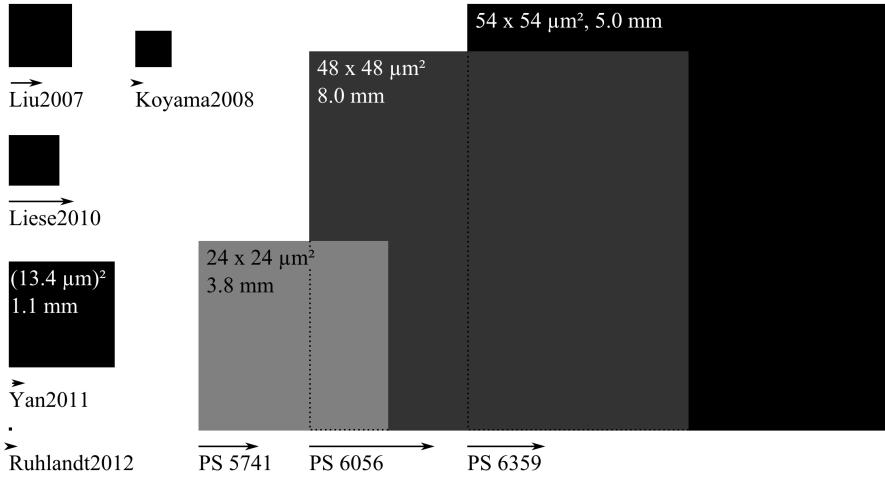


Figure 3.1.: Size of MLL apertures visualized as squares and corresponding focal lengths at 8.0 keV: published experimental results until begin of 2012 (left-hand side) and properties of our MLLs (right-hand side). The lengths of the arrows are sized to the focal lengths.

Considerations about appropriate design parameters

Focal length and aperture are the key parameters of each lens. They eventually define which and how many layers have to be fabricated. To identify reasonable values, the entire optical path has to be taken into account. In terms of *full-field imaging*, the image has to be separated from non-diffracted beams of the illumination at the image plane and it has to be large enough to be acquired by an X-ray detector. Those conditions are fulfilled in the X-ray microscope *NanoXCT-100* (compare Fig. 2.5). The distance from the object to the screen d_{OS} is 750 mm and the field of view of the high resolution 1024×1024 px X-ray detector w_{Det} equals $666 \mu\text{m}$ at $0.65 \mu\text{m}$ pixel size. The magnification M is the ratio of the field of view inside the object plane w_{Obj} and the detector: $M = w_{Det}/w_{Obj}$. Finally, the focal length is derived from the lens equation, thus

$$f = \frac{d_{OS}}{M + 2} \quad (3.1)$$

For example, for $w_{Obj} = 10 \mu\text{m}$ one obtains $M = 66.6$ and $f = 10.9$ mm. The resolution of the MLL should be in the order of the pixel size of the radiograph to avoid empty magnification.

There are significant differences in *scanning XRM* compared to full-field imaging, i.e. if an incoming laterally coherent parallel X-ray beam will be focused. A typical optical path is shown in Fig. 3.2 where an OSA is used to separate the first order beams from all other orders. Size and position of this aperture can be determined with simple geometrical considerations. While the separation from higher orders is typically not critical due to their larger divergence, separation from non-diffracted zero-order beams is crucial. As can be seen in the scheme, the OSA can move more closely to the lens, if

3. Multilayer Laue lenses

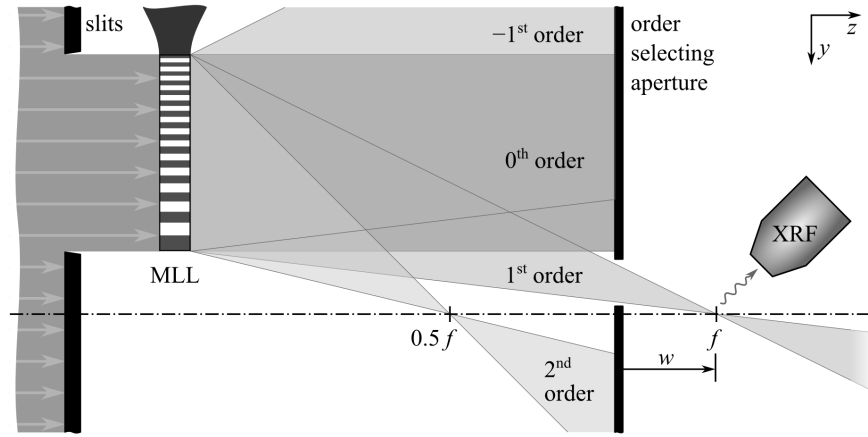


Figure 3.2.: One-dimensional scheme of a typical optical path of a scanning X-ray microscope. The incident beam is cropped with a slit system to exclusively illuminate the aperture of the MLL. An order selecting aperture (OSA, e.g. a pinhole) is used to stop direct beams and higher orders. The specimen is placed at the focus position f , having a working distance w from the OSA. An X-ray fluorescence (XRF) detector can be placed aside the specimen. Far field detectors and X-ray cameras are positioned further downstream.

the aperture of the MLL is present in some distance of the optical axis, i.e. innermost zones are missing. This approach increases the working distance between OSA and focus, which is a favorable situation regarding layer deposition. The challenging deposition of the innermost, thicker layers can be omitted (see next subsection). Hence, more thinner layers with less variations in layer thickness have to be fabricated to obtain the same total aperture, and therefore resolution. On the other hand, thinner layers are more sensitive to volume diffraction effects causing additional constraints. This issue is discussed in more detail in [YC12].

To summarize, focal lengths of several millimeters are preferred to get suitable working distances for focusing and reasonable magnifications for imaging. At the same time, it is necessary to realize heights of the multilayer stack of several ten microns, which define the total aperture of the lens, to achieve high resolution and to collect or to focus as much photons as possible.

Multilayer deposition

Magnetron sputtering is the method of choice for thin film deposition regarding the high requirements of an MLL [KB14]. This deposition technique allows a precise control of the absolute value of layer thickness, if the deposited materials are amorphous. Amorphization is achieved by a slight ion bombardment during layer formation with kinetic energies of few eV. Hence, small differences of thickness in the range of few picometers from layer to layer can be realized with an error of accumulated thickness deviations of substantially less than 1.0% at total deposition times of 50 h and more. Layer roughness

Table 3.1.: Used multilayer coatings and their properties. Focal lengths are given for 8.0 keV and 20.0 keV. The aperture equals the height of the multilayer stack. The given resolution is the theoretically achievable value.

Name	Materials	Focal length [mm]		Zone numbers	Zone thicknesses [nm]	Resolution [nm]	Aperture [μm]
		8.0 keV	20.0 keV				
PS 5741	MoSi ₂ /Si	3.8	9.4	5 – 1000	180 – 12.1	25.0	24.0
PS 6056	WSi ₂ /Si	8.0	20.0	50 – 2500	79.1 – 11.1	29.4	47.8
PS 6359	WSi ₂ /Si	5.0	12.5	512 – 7000	19.5 – 5.3	15.0	54.0

is well controlled even for thousands of layers. The root mean square value of interface roughness and interdiffusion length¹ is 0.3 to 0.4 nm. A slight radial decrease of layer thickness was allowed for each coating. This property will later be used to match focal lengths of assembled crossed MLLs. The combination of MoSi₂ and Si is known to have excellent properties for X-ray mirrors. The multilayer coating is deposited onto a \varnothing 150 mm silicon wafer that is finally annealed to reduce internal stresses [KB14]. Further details on the used magnetron sputtering process are provided in [Bra+13].

Using these considerations, three coatings have been fabricated and provided by *Fraunhofer IWS Dresden*. Their basic properties are listed in table 3.1. MoSi₂/Si was subsequently replaced by WSi₂/Si to increase the difference in refractive index decrements. A linear drift correction approach based on the previous experience was applied to the recipe for deposition PS 6359 to reduce the error of accumulated thickness deviations.

A known limitation of the used magnetron sputter system is the limited dynamics of variations in layer thickness in one run. That means, if the system is optimized for thin layers and a slight gradient of layer thickness, significant deviations occur at thicker layers having larger gradients. Another limitation is caused by the simultaneous coating of the deposition chamber itself during deposition. The probability of flitter particles to flake off increases with process time. In worst case, arching occurs and the deposited film is globally affected due to a new ignition of the plasma.

Fabrication of a single MLL

The subsequent procedure to eventually obtain an MLL is similar to other published approaches [LRK10; Kan+07]. The wafer with the deposited multilayer coating is cleaved to small pieces and thin stripes are cut using a precision saw. Then, the actual lens element is prepared with FIB milling, and the stripe is mounted onto a holder for further characterization and application. This procedure will now be discussed in detail.

The relative position to the wafer center of each cleaved wafer piece is marked. A *DAD 321 (DISCO corporation, Tokyo, Japan)* dicing saw is used to cut 70 μm thick stripes out of the wafer piece that is temporarily fixed onto an object holder with a suitable mounting adhesive. The cut depth is set to be less than the wafer thickness.

¹The interface roughness is given by the surface roughness of any deposited layer. Interdiffusion of adjacent materials additionally broadens the transition to the subsequent layer.

3. Multilayer Laue lenses

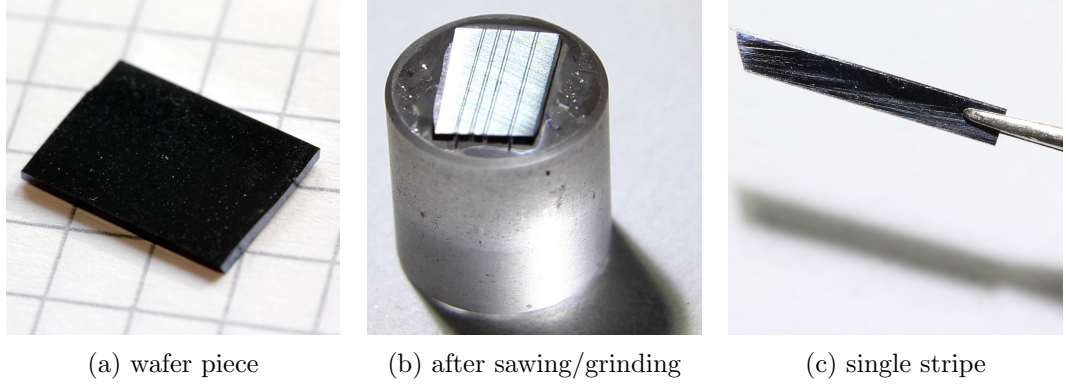


Figure 3.3.: Steps of the mechanical preparation. A wafer piece (a) is processed with the dicing saw. Backside grinding is used (b) to detach the single stripes from the substrate. The resulting stripe is handled with tweezers (c).

Table 3.2.: Used parameters of the precision saw and for FIB milling.

Dicing saw Disco DAD 321		SEM/FIB NVision 40	
Parameter	Typical value	Parameter	Typical value
Blade type	Z09-SD2000-Y1-60	Ga ⁺ beam	30 keV, 27 nA
Spindle rev.	30000 min ⁻¹	Depth	55 μm
Mode	manual single cut	Width	> 60 μm
Cut depth	500 μm	Dwell time	automatic
Feed rate	0.6 mm/s	Additional tilt	3.0°
Water flow	0.5 l/min		

For a crossed lens, two stripes have to be cut in a distance of Δr along the radius (cf. eq. 3.3). Subsequently, the wafer piece is transferred upside down to another object holder. Backside grinding is used to detach the free standing stripes from the remaining substrate. Acetone and water are used for dissolving the adhesive and final cleaning. Such a stripe can be divided in shorter parts, what is of particular interest to prepare crossed lenses (Fig. 3.5c) or complete MLLs (Fig. 3.6b). Fig. 3.3 shows several steps of the mechanical preparation. The parameters of the dicing saw are summarized in Table 3.2.

For this study, the actual lens element is fabricated with FIB milling in a combined SEM/FIB system (*NVision 40*, Carl Zeiss Microscopy GmbH, Oberkochen, Germany). The approach is similar to the so-called *H-bar preparation* of TEM lamellae [GS99]. The focused Ga⁺ beam is used for precise micromachining by etching material with a high spatial resolution. This preparation has two intentions: First, all damaged regions at the sidewall of the multilayer resulting from the mechanical preparation are removed. This relates especially to microcracks and layer delaminations. Second, the thickness of the MLL along the optical axis has to be adjusted to the photon energy (see Fig. 2.3) for the entire width and height of the lens element. The definition of all dimensions is shown in Fig. 3.4b. The resulting sidewalls are smooth, even if high ion currents of

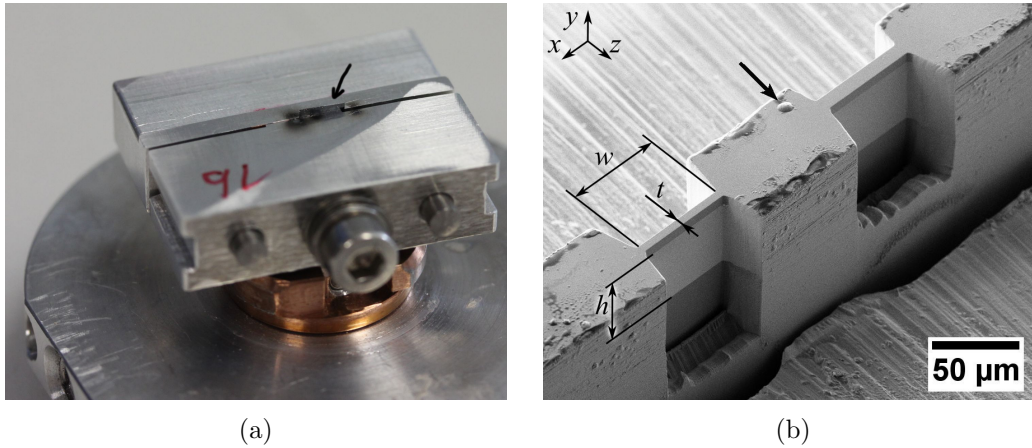


Figure 3.4.: FIB milling of a single MLL: (a) The customized specimen holder for FIB preparation of MLLs. The arrow points to the wafer stripe. (b) SEM micrograph of two MLLs on a single stripe after FIB preparation. The arrow points to a hump caused by a droplet. Width w , thickness t , and height h of the MLL are indicated. A protective layer of few microns of Si is deposited on top of the multilayer coating.

27 nA are used. In particular, no curtaining artifact² occurs as all materials are either amorphous or single-crystalline.

A customized object holder, which elastically clamps the stripe, was designed and built to improve specimen handling, i.e. the glue bonding to and subsequent debonding from a temporary holder is avoided (Fig. 3.4a). Two standard trapezoidal milling boxes are defined in the FIB system to coarsely thin the entire multilayer stack starting from both sides along the thickness of the stripe (Table 3.2). It should be ensured that no hump on the surface exists at this position (cf. Fig. 3.4b). The MLL might otherwise suffer from enclosed droplets. Then, both sidewalls are milled successively until the desired thickness of the MLL element is reached. To ensure positioning accuracy and coplanar sidewalls, milling is now performed from the same direction, i.e. the SEM stage has to be rotated by 180° to process the second side. The stage is additionally tilted by approximately 3.0° to increase the angle of incidence of the Ga^+ ions to mill the final sidewalls without taper. The FIB processing takes about 5 h for each MLL and the number of individual milling steps was reduced to three steps using this optimized strategy. Fig. 3.4b shows a result.

The resulting stripe is then mounted onto a holder for XRM investigations. A $\varnothing 3$ mm copper ring – well known from TEM specimen preparation – serves as standard frame for laboratory experiments. Another custom holder was provided by *Fraunhofer IWS Dresden* for synchrotron radiation experiments. This holder has a window of $3 \times 3 \text{ mm}^2$

²Curtaining, i.e. a special roughness of the milled sidewall, is a well known artifact in FIB processing. It is especially observed on heterogeneous and polycrystalline materials being caused by different etching rates of other materials and along different crystal orientations adjacent grains, respectively. A too low overlap of adjacent raster spots of the ion beam represent another source for curtaining.

3. Multilayer Laue lenses

where the lens element can be placed. It is compatible to the *AttoCube* nanomanipulator system at the beamlines *P06*, *PETRA III*, Hamburg and *ID13*, *ESRF*, Grenoble (see section 3.7). A single holder can be equipped with several stripes that contain individual MLLs, if they are stacked vertically. If lenses from coatings with different focal lengths are used, they might be assembled onto a single holder that offers multiple positions along the optical axis. Hence, only a minor change in focus position will happen, if lenses are switched. This approach allows a fast change of the lenses during experiments at synchrotron radiation facilities. All bonding is performed with solvable adhesives such as commercially available superglue or nail polish. This way, each stripe can be released and cleaned with acetone for repositioning or for other further purposes.

Few individual one-dimensionally operating MLLs can be fabricated side by side on a single stripe. This is especially reasonable if MLLs with different thicknesses in beam direction should be compared during experiments at synchrotron radiation facilities (compare Fig. 3.4b). Switching between those adjacent lenses requires only a small translation of the stripe, what significantly simplifies experiments.

The above described approach yielded decent results for PS 5741 and PS 6056, but few additional measures have to be taken for PS 6359. This is necessary, because this multilayer coating has smaller zone widths down to 5 nm, which make the lens more sensitive to geometrical imperfections. The residual compressive stress after annealing was apparently greater than the stress of both other coatings. This stress may cause a buckling of the lens element. Gallium implantation into the silicon substrate at the bottom of the MLL may lead to additional compressive stress, and therefore, to an elastic deformation of the lens element. These effects can be reduced if the MLL is detached from the remaining multilayer stack after initial milling. The analysis of those defects, examples of fabricated lenses, and feedback to preparation will be described in section 3.3.

Fabrication of crossed partial MLLs

As a major difference to published approaches, crossed MLLs are obtained from a single wafer [KB14] and they are assembled to a compact device in this study. Two single partial MLLs will be directly bonded in series perpendicular to each other to obtain a two-dimensionally operating lens. Though the distance along the optical axis is only in the order of 30 μm , this value exceeds the depth of focus and astigmatism will occur. Therefore, both lenses have to have matched focal lengths that differ by Δf . The thickness gradient along the radius r of the coating $\eta = \frac{dh}{dr}$ will be employed to realize the matching (cf. eq. 3.4). Based on eq. 2.11, the height of the multilayer stack can be described as

$$h = (\sqrt{1 + n_{\Omega}} - \sqrt{n_A}) \sqrt{\lambda f} \quad , \quad (3.2)$$

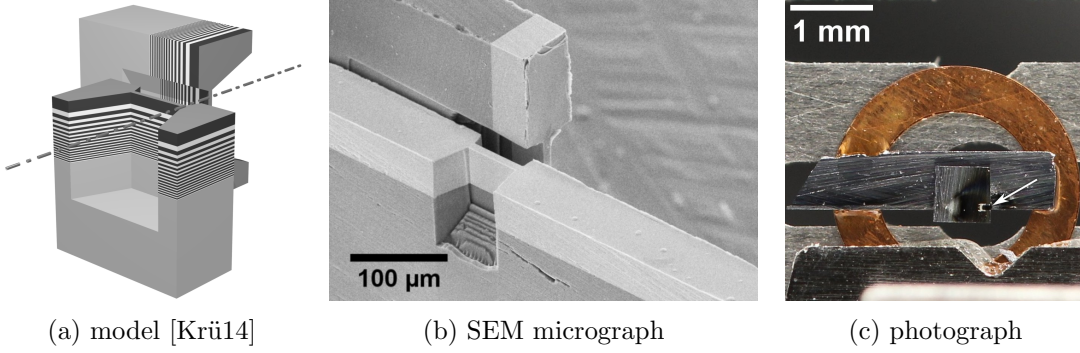


Figure 3.5.: Crossed MLLs: (a) The simplified model shows the orientation of individual layers of the multilayer stack with respect to the wafer stripe and the optical axis. (b) The multilayer stack appears bright in the SEM micrograph. (c) Crossed MLLs are assembled from a longer and a shorter stripe, being mounted on a $\varnothing 3$ mm Cu ring. The arrow points to the actual lens.

with n_A and n_Ω being the numbers of the first and last zone. The slope of the focal length at a given radius is

$$\frac{df}{dr} = \frac{2\eta h(r)}{(\sqrt{1+n_\Omega} - \sqrt{n_A})^2 \lambda} . \quad (3.3)$$

Finally, $\Delta r = \Delta f / \frac{df}{dr}$ is obtained with linear approximation.

Two stripes – each containing an MLL – have to be fabricated as described above with matching focal lengths. The width of each lens element should be two times of the aperture size to reduce demands on tolerances during assembly. Each MLL might be placed off-center of the stripe to reduce the distance along the optical axis between both lens elements (Fig. 3.5a). It proved to be beneficial to fabricate one MLL on a short stripe with a length of 1 mm. The longer, second stripe has a length of at least 3 mm in order to mount the lens assembly to a holder (compare Fig. 3.5c). Both stripes are assembled on top of each other and the cutouts are aligned in series using a stereo microscope. Once both stripes are oriented perpendicularly to each other, a solvable adhesive is used to carefully bond the crossed MLLs. Fig. 3.5 shows the scheme and images of real crossed MLLs.

Fabrication of a complete MLL

Initial experiments were done with complete MLLs [Liu+07; LRK10; Yan+10; YC12] based on PS6056. Basically, two MLLs have to be placed vis-à-vis in parallel (cf. Fig. 3.6b). To match the focus of both partial lenses, the positioning accuracy has to be better than half the resolution. Because of the 49 missing innermost zones (cf. Table 3.1), a certain space between both lenses has to be set. This distance equals $15.59 \mu\text{m}$ for PS 6056. $6.50 \mu\text{m}$ of additional amorphous silicon had been deposited onto

3. Multilayer Laue lenses

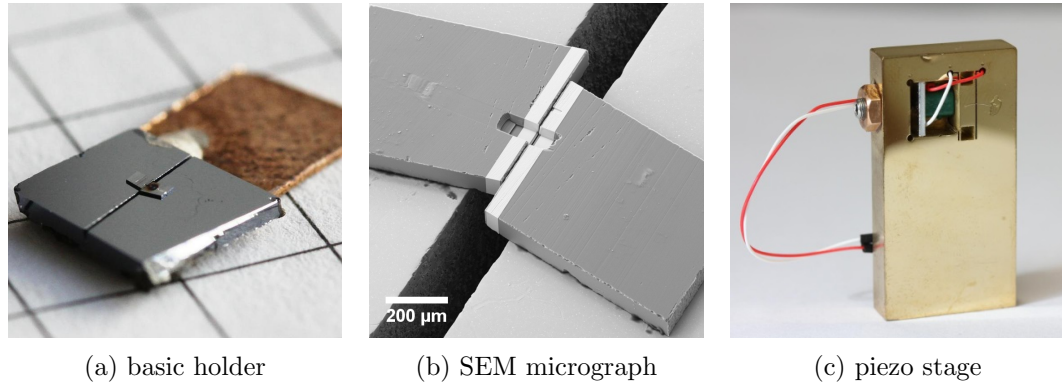


Figure 3.6.: Evaluation of a complete MLL.

the wafer piece in order to reduce the absolute distance to $2.59 \mu\text{m}$ and to allow a better absolute accuracy of length measurement in the SEM.

Two short stripes from adjacent positions of the wafer were fabricated, each containing an MLL. Both stripes are attached onto a silicon plate containing a $130 \times 130 \mu\text{m}^2$ aperture (Fig. 3.6a) with an adhesive that can be cured by electron beam irradiation (*SemGlu*, *Kleindiek Nanotechnik GmbH*, Reutlingen, Germany). The plate is transferred into the SEM and a micromanipulator system (*MM3A*, *Kleindiek Nanotechnik GmbH*) is used to align both stripes under normal SEM operation (5 kV acceleration voltage, $30 \mu\text{m}$ aperture). Subsequently, the adhesive is cured using a selective illumination along the outline of the stripe at different settings (25 kV acceleration voltage, $120 \mu\text{m}$ aperture, high current mode). Fig. 3.6b shows an assembled complete MLL.

The main drawback of this approach is the fixed distance after preparation. An iterative refinement of the interspace is necessary to find correct values, which slightly differ from design parameters. Hence, a piezo stage was designed and built to allow experiments with varying interspace of both MLLs inside the X-ray microscope, see Fig. 3.6c. One stripe is mounted onto a slide that can be moved via a flexure by the piezoelectric actuator (*AE0203D04F*, *Thorlabs Inc*, Newton, NJ, USA). The actuator offers a displacement of $3.0 \mu\text{m}$. It can be driven in open-loop operation with the *E-709* controller (*Physik Instrumente GmbH & Co. KG*, Karlsruhe, Germany) that belongs to the MicroDCB device (see chapter 4.3 and appendix B, p. 119).

Table A.1 summarizes all fabricated MLLs.

3.3. Geometrical characterization of the multilayer stack and individual MLLs

It is obvious to characterize the real optical properties of the X-ray lenses in suitable focusing and imaging experiments. In addition, several methods were developed to perform initial characterization of the entire stack and of individual MLLs to control the fabrication process.

Radial gradient of layer thickness

The radial gradient of layer thickness can be measured with X-ray reflectometry (XRR) at test wafers that are used to calibrate the magnetron sputter system before each multilayer deposition³. This distribution is then normalized to the height of the multilayer stack. Alternatively, the thickness of the entire multilayer stack can be measured with SEM at a cleaved cross section along the wafer's radius. Fig. 3.7 shows the results for PS 6056 and PS 6359. The thickness gradient is well described with a 3rd-degree polynomial $h(r)$:

$$h(r) = a_3r^3 + a_2r^2 + a_0 \quad (3.4)$$

Its linear coefficient equals zero, because the derivate at $r = 0$ is zero due to symmetry. Scattering of the experimental data is mainly attributed to delaminated areas at the cleaved edge, if SEM measurement is used. These relations are necessary to size the focus matching (cf. eq. 3.3).

Precision of layer thicknesses

The process stability of the magnetron sputtering characterized by the drift of the deposition rate is crucial for the final quality of the MLL [KB14]. There is no direct method available to monitor the deposition rate in-line during the thin film deposition with sufficient accuracy. It is possible to perform XRR measurements at test wafers that are run before and after the multilayer coating. However, the final deposition might fail due to changed conditions of the chamber, e.g. caused by flitter particles yielding arching at the end of the rather long deposition process. Assuming a linear drift of the deposition rate, this drift affects size and position of side lobes of the X-ray focus. This will be shown in section 3.4. Ptychographic investigations at synchrotron radiation facilities are able to

³This measurement is done at *Fraunhofer IWS Dresden*.

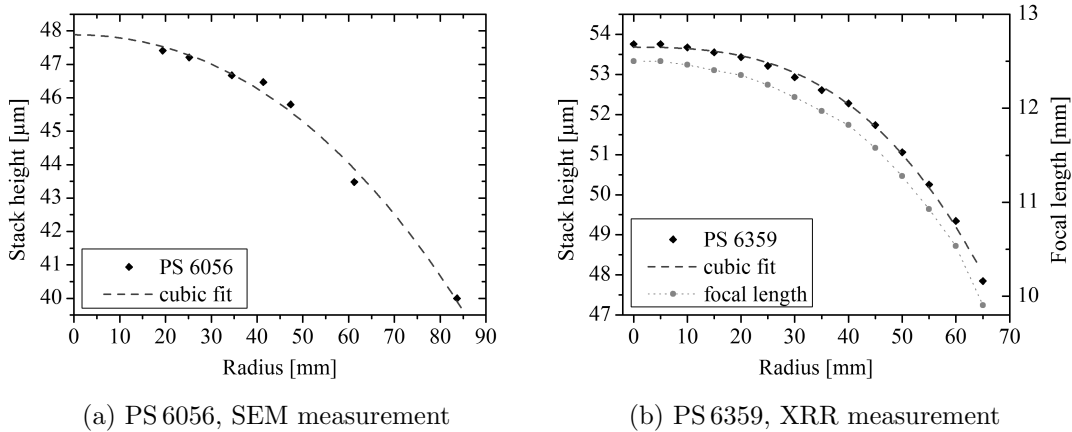


Figure 3.7.: Measured thicknesses of the multilayer stack for PS 6056 and PS 6359.

3. Multilayer Laue lenses

reconstruct the complex wave field at the focus position (section 3.7). This data can be fit to an average linear drift. To be independent from investigations using synchrotron radiation, an alternative access is desired.

Huang et al. use SEM investigations to measure these values [Hua+13]. However, since the resolution of a modern SEM is in the order of 1 nm, it is not possible to directly measure the expected deviations from the design values in micrographs of cross section of an MLL. Considering the translation invariance of the multilayer in one dimension and the sharp transition of both materials, a more sophisticated evaluation is possible. A line intensity profile is taken perpendicularly to the layers and averaged over a certain width to reduce noise. Then, an edge detection algorithm is applied and the half maximum position of each edge is determined with sub-pixel resolution by fitting a polynomial function to the measured values. The distance of two neighboring positions equals the layer thickness. Calculating floating average values of adjacent distances circumvents effects of slightly different shapes of falling and rising edges.

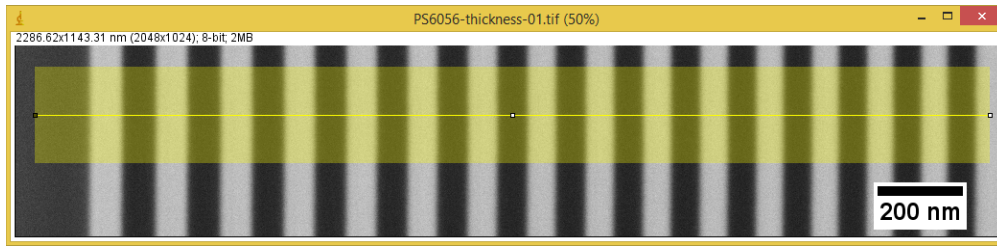
This algorithm is implemented in the *ImageJ* plugin *Measure Layer Thickness*, see Fig. 3.8 and appendix B, p. 108. It was used to characterize PS6056 at a FIB cross section. The used SEM parameters are listed in Table 3.3. At first, the thin layers are analyzed, which are directly deposited onto the silicon substrate. The measured values typically own a systematic deviation from the design values due to the limited SEM calibration, a slightly slanted incidence of the electron beam with respect to the layer orientation, and the incorporated thickness gradient, if the measurement is not performed at the center of the wafer. Therefore, an empirical correction factor is determined and subsequently applied to all measurements, i.e. the thin layers provide the reference for calibration. Fig. 3.9a shows a typical experimental result for the thin layers where even the small increase of thickness of 0.4 nm over the first 180 layers is clearly visible.

The measured thickness can now be compared to design values at arbitrary positions. However, since this semi-automated approach requires a correct assignment of layer indices, it is challenging to avoid mistakes at central positions. H. Yan et. al suggests to use marker layers [Hua+13], e.g. to replace a single Si layer by a WSi₂ layer every few microns. In this study, we focus on the outermost layers, as no markers are yet incorporated. Fig. 3.9b contains a comparison of the measured values to the design

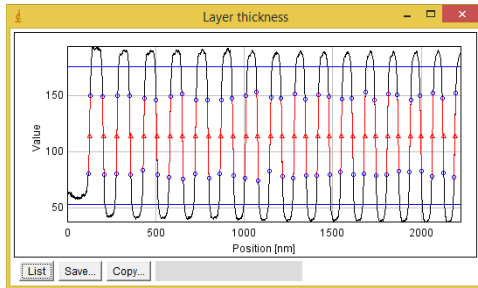
Table 3.3.: SEM parameters to measure layer thicknesses.

Parameter	Value (Zeiss NVision 40)
Acceleration voltage	5 kV
Working distance	5 mm
Magnification	50000 ×
Detector	InLens
Scan size	2048 × 1536 or 3072 × 2304
Scan speed	9

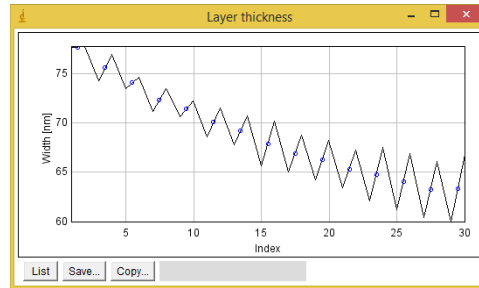
3.3. Geometrical characterization of the multilayer stack and individual MLLs



(a) SEM image with line

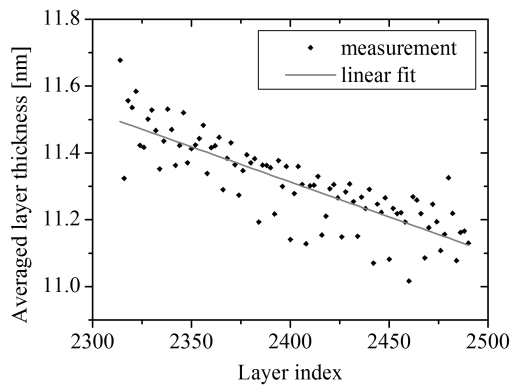


(b) line profile with fit edges

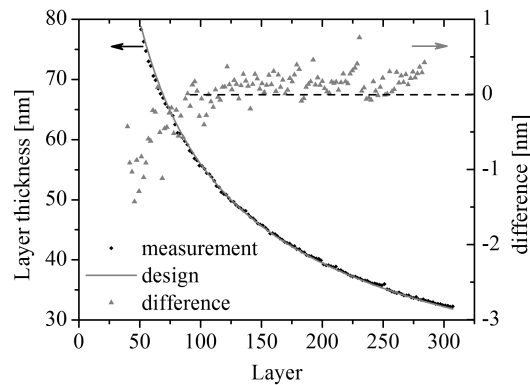


(c) thickness graph

Figure 3.8.: *ImageJ* plugin *Measure Layer Thickness*: demonstration at thick layers of PS 6056. The circle in (c) is the floating average value of two adjacent layers.



(a) thin layers



(b) thick layers

Figure 3.9.: Results of the advanced SEM analysis to measure layer thicknesses.

values for the top-most 250 layers. A large discrepancy is obvious for layers 50 – 100. This relates to inherent deviations of the magnetron sputtering system. It is only able to master a certain limited variation of the layer thicknesses within one recipe, which is why larger tolerances have to be accepted for the few top-most layers having exceeding increments in layer thickness. The drift value is determined at layers 150 – 300, which are in average 0.4 % thicker than expected.

XRM inspection

The quality of the lens elements, influences of residual stresses, and geometrical imperfections can be studied with laboratory X-ray microscopy, if the MLL is imaged with

3. Multilayer Laue lenses

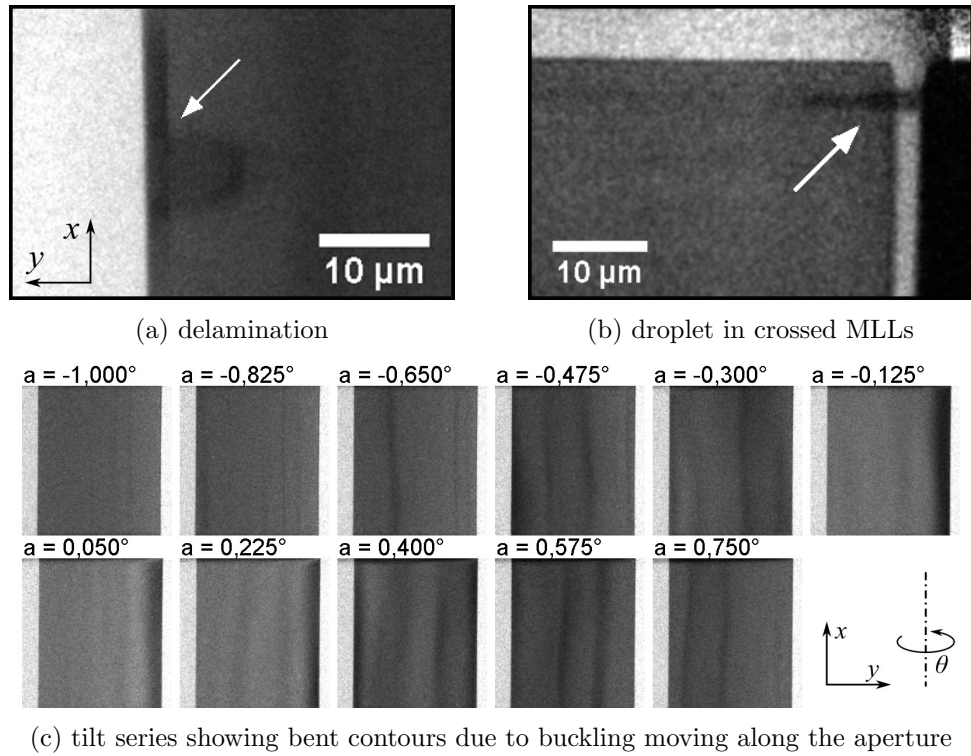


Figure 3.10.: Characterization of an MLL with laboratory XRM.

the $10\times$ magnifying FZP. Initially, such imaging was used to easily align the MLL inside the X-ray microscope *NanoXCT-100*. Once the lens is rotated almost in parallel to the optical axis, extinction patterns are observed. They have a certain dependence on the orientation of the multilayer with respect to the optical axis and tilt series are acquired for further evaluation. Typically, the MLL is rotated by $\pm 1^\circ$ while a series of radiographs is acquired.

A qualitative analysis of geometrical imperfections is possible by analyzing the shape of the extinction patterns. There are several less transparent regions along the layers visible, which traverse the lens if the tilt angle changes. They are expected to appear as straight contours in ideal case. Any difference like bending or buckling of the contour is a clear indication for critical residual stresses causing elastic deformation of the lens. In addition, local defects like included droplets and layer delaminations, which are related to flaws of the magnetron sputter deposition or mechanical preparation of the lens, can be seen as artifacts in the radiographs. Fig. 3.10 provides an overview of typical observations.

Measurement of layer tilts

Tilt series can be evaluated quantitatively to reveal local changes of the orientation of the multilayer within the aperture of an MLL. Such changes might be caused by remaining residual stress as described above. On the other hand, a specific elastic deformation of

3.3. Geometrical characterization of the multilayer stack and individual MLLs

the lens element can be exploited to realize a wedged shape of the MLL, see section 3.8. In all cases, a quantitative characterization of this effect that does not rely on synchrotron radiation is preferred to get a prompt feedback of the preparation of MLLs. The subsequently presented method analyzes the extinction patterns, which are observed with laboratory X-ray microscopy, if the MLL is tilted. It determines the relative layer tilt $\Delta\theta$ at arbitrary positions of the lens with respect to a reference state. The reference state may be a flawless area within the aperture of a single MLL, or the entire area of the lens to reveal effects of an additional process step, which affects the lens globally. The latter approach is of particular interest to characterize wedged MLLs. The result is typically shown as a map over the entire aperture of the MLL.

It can be assumed, that the recorded intensity $I(\theta)$ at a certain position (x, y) within the aperture of the MLL is defined by the illumination, the thickness of the MLL along the optical axis, the local layer thickness, and the tilt of the zone with respect to the optical axis⁴. The first two parameters are fixed. The layer thickness depends on the y -position. Considering a condition A where all layers are parallel to the optical axis at $\theta = 0$, and a condition B where the MLL is tilted by $\Delta\theta$, it will be $I_A(\theta) = I_B(\theta - \Delta\theta)$ for all corresponding positions. Thus, $\Delta\theta$ is determined by cross correlation at equal positions (x, y) , e.g. by calculating the center of gravity of $I_A(\theta) \star I_B(\theta)$.

This method can be applied to compare any position of an MLL with a corresponding reference. In case of a single MLL, the central part at position x_M with respect to its width is usually considered as non-deformed, unless buckling is observed. The local relative layer tilt $\Delta\theta$ is calculated by

$$\Delta\theta(x, y) = D_\theta [I(\theta, x, y) \star I(\theta, x_M, y)] \quad . \quad (3.5)$$

The operator D has to be defined with any suitable method to determine the center of the cross correlation function. Currently, a center of gravity determination is implemented, thus

$$D_\theta [f(\theta)] = \frac{\sum_i \theta_i (f(\theta_i) - o)}{\sum_i (f(\theta_i) - o)} \quad \text{with } o = \min \{f(\theta)\} \quad . \quad (3.6)$$

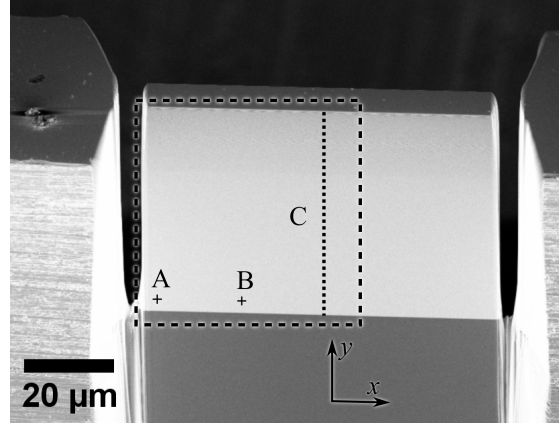
The offset o of $f(\theta)$ is subtracted to improve the determination. As an alternative, the function can be fitted to a Gaussian curve

$$g(\theta) = A \exp\left(-\frac{(\theta - \Delta\theta)^2}{w^2}\right) + o \quad . \quad (3.7)$$

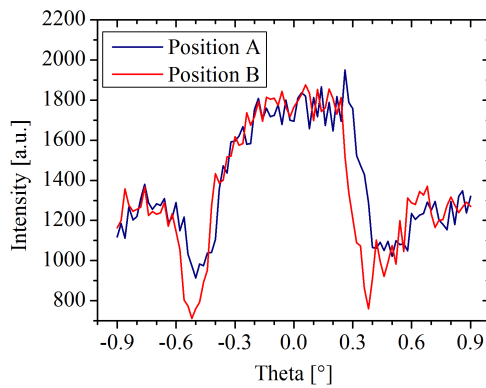
This evaluation is performed to measure the quality of a fabricated MLL and to study the influence of process parameters. Fig. 3.11 shows $\Delta\theta$ maps for the same MLL. The lens element was detached from the remaining multilayer during initial preparation

⁴Regarding the definition of the axes: x and y are along the width and height of the MLL, respectively (cf. Fig. 3.4b). Hence, both axes span the image plane of a typical radiograph of an MLL (cf. Fig. 3.10c). z is along the optical axis and θ defines a rotation around x .

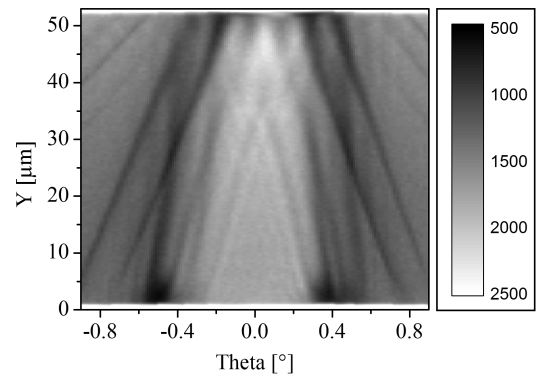
3. Multilayer Laue lenses



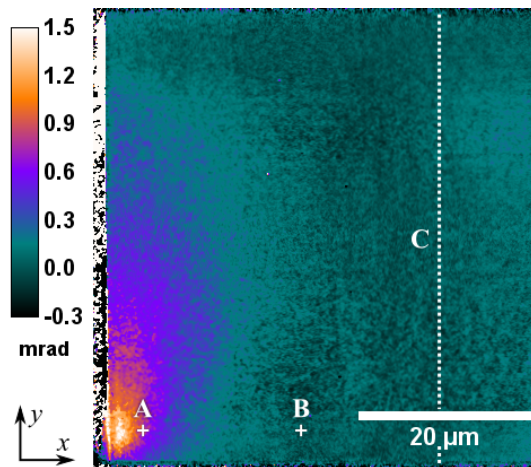
(a) SEM image: positions A & B and line C are indicated, the dashed area marks the evaluated region



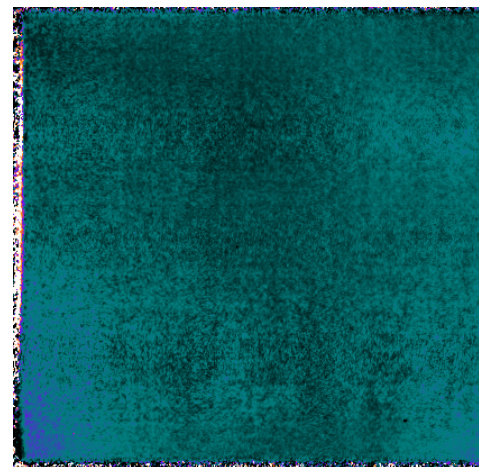
(b) $I(\theta)$ at positions A and B



(c) $I(y, \theta)$ along line C



(d) $\Delta\theta$ map, 1st FIB preparation



(e) $\Delta\theta$ map, 2nd FIB preparation

Figure 3.11.: $\Delta\theta$ evaluation of an MLL comparing two FIB strategies: (a) SEM image of the lens. The evaluated region and positions A, B, and C are indicated. (b) Plots of $I(\theta)$ at positions A and B – the shift in θ is clearly visible. (c) The shape of $I(\theta)$ depends on the y position due to the changing layer thickness. (d) & (e) Maps of the relative layer tilt show the influence of two FIB strategies. A substantial deformation in the lower left corner of the MLL being visible in (d) was reduced by a modified FIB preparation (e).

3.4. Simulation of the optical properties

(Fig. 3.11a). The gallium implant volume at the bottom of the MLL and the redeposition layer at the sidewall of the MLL were removed at both sides in advance of the second measurement with a different FIB procedure. It is evident that the relative layer tilt at the bottom-edge of the MLL was significantly reduced and it is estimated that this FIB procedure yields an enhanced optical performance.

To test the robustness of the presented method for obtaining the $\Delta\theta$ distribution over the aperture of the MLL, typical misalignments had been enforced and the acquired datasets were evaluated against the initial state. First, the entire MLL specimen was rotated by 5° inside the object plane. The resulting radiographs were aligned with the initial dataset by translation and rotation. Second, the object was placed out of focus by $200\ \mu\text{m}$, which is larger than the depth of focus. In both cases, the $\Delta\theta$ evaluation showed no significant difference to zero. This indicates, that the method is not sensitive to regular misalignments.

A similar evaluation can be done to characterize global effects of an additional process step, e.g. to study wedged MLLs. Here, tilt series of the lens after a geometrical modification $I_{\text{mod}}(\theta)$ are evaluated against tilt series of the initial lens after FIB preparation $I_{\text{origin}}(\theta)$. The $\Delta\theta$ map is calculated with

$$\Delta\theta(x, y) = D_\theta [I_{\text{mod}}(\theta, x, y) \star I_{\text{origin}}(\theta, x, y)] \quad . \quad (3.8)$$

This analysis is implemented in an *ImageJ* plugin called *MLL Tilt Evaluation* (see appendix B, p. 114). Further results of this method will be shown and discussed in section 3.8.

3.4. Simulation of the optical properties

Though there are few theoretical papers published about optical properties of multilayer Laue lenses, two rather simple models were developed to gain a better understanding of the behavior of these lenses. In particular, recent work was concentrated on the focusing properties of MLLs and no experience is available for full-field imaging properties. At first, the entire optical path of the laboratory X-ray microscope can be simulated with the program *RayT*, which was kindly provided by Dr. P. Krüger [Krü13]. It is based on geometrical optics. Another simulation library called *MLL.i*, which considers physical optics, was developed in this thesis.

Geometrical optics simulation – RayT

RayT [Krü13] implements a ray tracing algorithm to simulate the effects of all optical components along the beam path of the microscope. All dimensions, distances, and positions can be modified. Here, they are set to real values based on the known or estimated design of the beam path of the X-ray microscope *NanoXCT-100* (Fig. 2.5).

3. Multilayer Laue lenses

The program is written in *Java*. It offers a graphical user interface to define all optical elements and to run the simulation, see Fig. 3.12.

The X-ray source is implemented as a circular area. Individual rays are emitted from random positions at the source area to random directions within a specified divergence along the optical axis. Refraction, reflection, and extinction are considered for each optical element until the ray might hit the detector at the calculated position. Beamstop and pinhole are modeled as simple elements with a certain area where all incoming rays are stopped. The condenser is modeled as a section of a spheroid. Its inner surface reflects incident rays, if the condition for total reflection is fulfilled. Diffractive lenses are replaced with models of their refractive equivalents. The FZP and a single MLL are substituted by a spherical lens and a cylindrical lens, respectively. Geometry and index of refraction are adjusted to match the focal lengths of the real lenses. Each lens can be parameterized with a probability η that an incident ray interacts with it. Thereby, the effect of limited diffraction efficiency can be simulated, and beams in zero-order and first-order occur. Finally, an object that features a spatial distribution of transmissivity can be placed anywhere. The simulated image shows the distribution of the X-ray intensity at the detector.

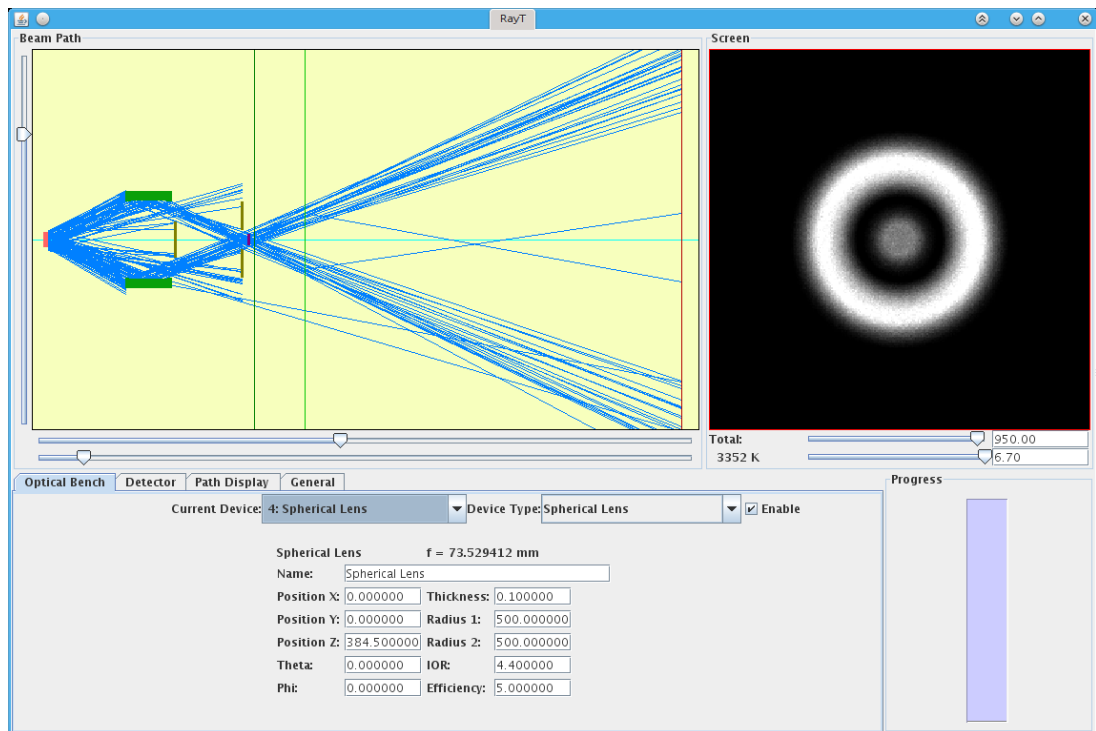


Figure 3.12.: Screenshot of *RayT* [Krü14] showing the simulation of the beam path of the X-ray microscope *NanoXCT-100* with the $10\times$ FZP.

Physical optics simulation – MLL.i

A complementary simulation software was developed to account for physical optics being the actual mechanism of the optical properties of those lenses. In literature, few theoretical approaches exist to calculate focusing properties of linear and circular zone plates. Dynamic diffraction inside the lens is described with coupled wave theory [MS92; Sch97], with the parabolic wave equation in paraxial approximation [Sch06], or based on the Takagi-Taupin approach [Yan+07]. Different geometries of the MLL like flat, tilted, wedged, and curved layers were analyzed. The point spread function of the focus, in particular its spot size and the extent of side lobes, as well as local and global diffraction efficiency are of special interest.

In this thesis, a different approach is used. It is based on point source synthesis, which is well known to calculate acoustic sound fields [Spi94]. It is a straightforward implementation of the Huygens-Fresnel principle. The X-rays are emitted from a source and they propagate to the optical element on arbitrary paths. The interaction with the MLL is simplified with a ray tracing approach to reduce computational time. At its back side, another point source is generated and the X-rays propagate to the detector. The source can either be a laterally coherent parallel beam illumination or a point source. This approach allows focusing properties or imaging properties to be simulated, respectively.

Fig. 3.13 shows a scheme of the model that is used. The simulation can be run in two or three dimensions. The latter one is evidently necessary if crossed MLLs are simulated, because one dimension is required for the extent of the optical axis. The front side of the MLL is discretized to a rectangular grid with a given spacing. The position of each point is displaced by a random amount within its cell to avoid aliasing. During a simulation, beams are propagated from the source to each grid position. The beam is subsequently propagated through the MLL having a thickness t in its former direction until it reaches the back side. External reflection is considered at interfaces from optically less dense to optically more dense materials. The positions of the phase boundaries are given by the layer positions of the MLL. In case of crossed MLLs, the beam is propagated through the gap d_g between both lenses and through the second MLL in the same way. The detector is split into discrete elements as well, and each beam is then propagated individually to each of these elements.

Each beam path is split at phase boundaries. Within each of the sections, the complex amplitude A of the wave field will be propagated according to the scalar form of eq. 2.2:

$$A_i^{(\text{ray})} = A_{i-1}^{(\text{ray})} \exp(k_i \Delta x_i) \quad \text{with} \quad k_i = \frac{2\pi n_i(\lambda)}{\lambda}, \quad i = 1 \dots N \quad . \quad (3.9)$$

The initial amplitude at the source is set to $A_0 = 1 + 0i$. Δx_i equals the length of the section. The complex refractive index n_i of the corresponding material has to be known for the selected wavelength λ . While this procedure is looped over all beams that are

3. Multilayer Laue lenses

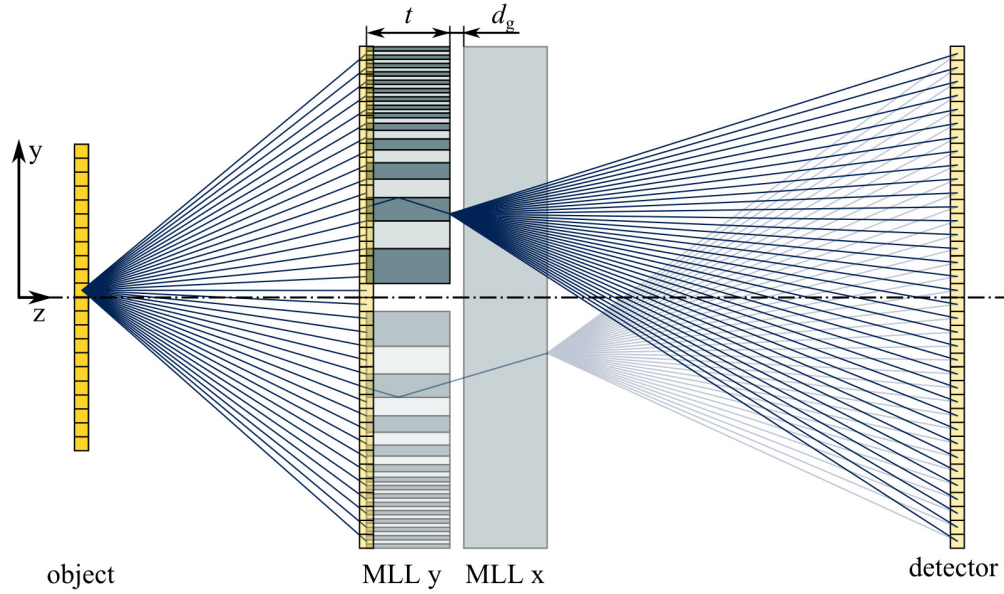


Figure 3.13.: The model for the physical optics simulation in case of a point source. Both one-dimensional grids at the front side of the MLL and at the detector position are illustrated. A second point source is generated at the exit of the MLL. Complete and crossed MLLs are indicated.

emitted from the source, the complex amplitudes $A_N^{(\text{ray})}$ are added up at each position m of the detector. Finally, the intensity can be calculated by

$$I_m = \left(\sum_{\text{rays}} A_N^{(\text{ray}, m)} \right)^2 . \quad (3.10)$$

Point source synthesis requires mesh sizes that are smaller than the wavelength to minimize artifacts. In this case, the lateral extent of the MLL is in the order of $50 \mu\text{m}$ and the wavelength is typically smaller than 0.16 nm , yielding more than $3 \cdot 10^5$ elements in each dimension of the grid. Facing memory requirements and in particular computational time, it is obvious that this condition cannot be satisfied in particular for three-dimensional simulations when a two-dimensional grid is required at the front side of the lens. It is nevertheless assumed that regions with significant intensity such as the main peak and its side lobes are well represented and this model is suitable to get a basic insight into focusing and imaging properties of MLLs. In particular, the results appear to be physically reasonable. Though the simulation allows arbitrary thicknesses t and interspaces d_g of both MLLs, large values exceeding few microns yield increasing artifacts. They are caused by the used ray tracing approximation for the propagation through the lens.

The following configurations of individual MLLs can be simulated:

- a single partial MLL, consisting of a range of zones;

3.4. Simulation of the optical properties

Table 3.4.: Major parameters for the physical optics simulation.

		Imaging	Focusing
MLL design		PS 6056 (see Table 3.1)	
Photon energy	[keV]	8.05	20.0
Focal length	[mm]	8.05	20.0
X-ray source		point source	coherent parallel beam
Object position	[mm]	-8.140	—
MLL position	[mm]	0	0
Detector position	[mm]	750.0	20.000
Detector size	[μm]	40	0.65

- two facing partial MLLs (*complete MLL*) with variable distance and missing inner zones;
- crossed partial or complete MLLs with variable distance of both lenses along the optical axis (requires three-dimensional calculation).

Each MLL is defined with layer thicknesses according to the zone plate law, a thickness along the optical axis, and complex index of refraction for both materials. A linear drift of the deposition rate can be applied to the layer thicknesses. This algorithm is implemented in the library *MLL.i* for the interpreted mathematical programming environment *Yorick* [Mun10]. It was used to simulate several MLL configurations to get a better knowledge of their expected optical behavior.

Some important results will be briefly summarized and discussed. Design parameters of PS 6056 were used to simulate the MLL. Photon energies and distances to the detector are set according to real values of the X-ray microscope *NanoXCT-100* (imaging) or of *PETRA III* beamline *P06* (focusing), respectively, see Table 3.4.

It has not been shown so far that MLLs can be used for full-field imaging. Therefore, the image of a point source was calculated to obtain the point spread function inside the image plane. This calculation can be performed for a single MLL and crossed MLLs expecting a line focus and a point focus, respectively. Fig. 3.14a shows peak profiles on the detector of a single MLL. The calculation was performed in two dimensions for five different y -positions of the point source with respect to the optical axis. It was already discussed, that such a *partial* MLL only contains a part of the complete aperture in contrast to a Fresnel zone plate. Therefore, all zones are placed at one side of the optical axis – in positive y -direction in this case. If the point source is placed directly on the optical axis ($y = 0 \mu\text{m}$) or moved to positive y -direction ($y = 10 \mu\text{m}, y = 20 \mu\text{m}$), the point spread function (PSF) is dominated by a main peak. If the point source is moved to negative y -direction ($y = -10 \mu\text{m}, y = -20 \mu\text{m}$), the PSF broadens and collapses to few single peaks. Consequently, proper imaging cannot be expected. Fig. 3.14b shows the 2D PSF of crossed MLLs if the point source is located on the optical axis ($x = y = 0$). Hence, proper imaging for a partial MLL can be expected, if the object is placed at the

3. Multilayer Laue lenses

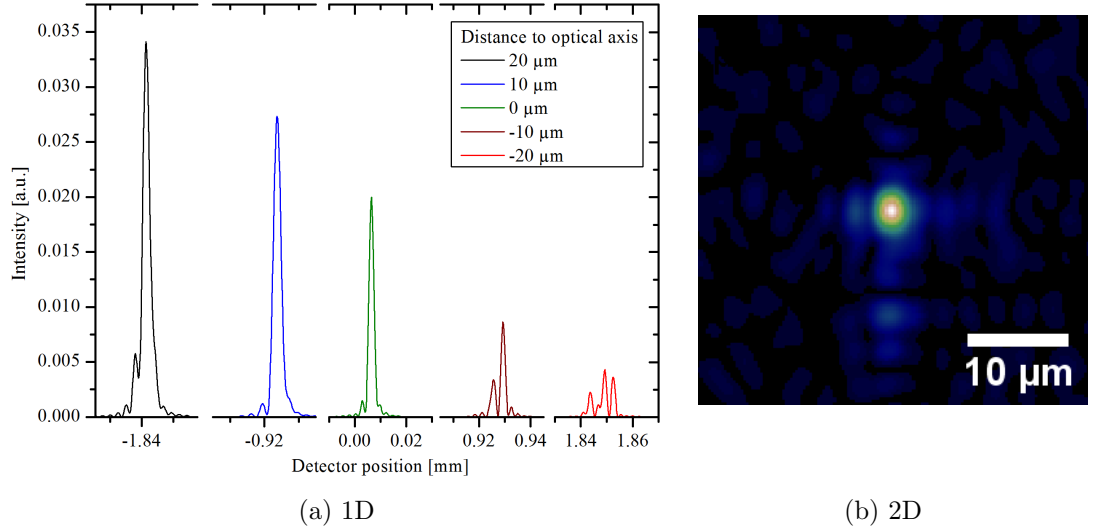


Figure 3.14.: (a) Simulated PSF on the detector of a partial MLL for several distances of the point source from the optical axis. (b) 2D PSF of crossed MLLs.

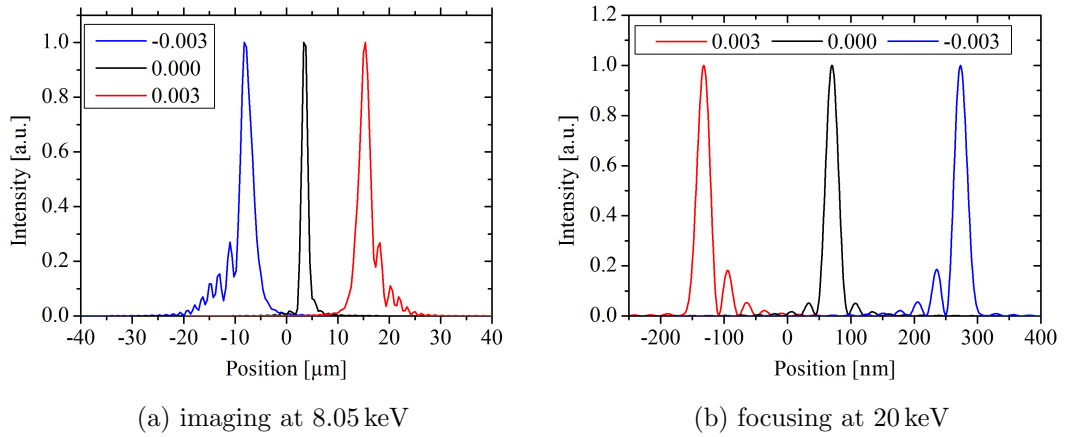


Figure 3.15.: Simulation of the effect of a drift during layer deposition on the shape of (a) the image of a point source imaged by an MLL to a scintillating screen and (b) the focus of an incident parallel beam.

side of the MLL or close to the optical axis. The focus broadens and side lobes occur if a drift of $\pm 0.3\%$ during layer deposition is assumed, see Fig. 3.15a.

Two cases were studied for X-ray focusing. At first, a focal series was simulated for crossed MLLs at a photon energy of 20.0 keV, see Fig. 3.16. That means, the position of the detector was changed within a range of $\pm 140\ \mu\text{m}$ around the focal length. The best focus is obtained at a position of 20.000 mm as expected and minor side lobes exist in vertical and horizontal direction according to the orientation of both MLLs. The focus broadens during defocusing and several peaks appear in a rectangular pattern.

A second 2D simulation was performed for a single MLL to investigate the effect of a drift of the deposition rate. Fig. 3.15b shows PSFs for three different cases of positive, negative, and zero drift. Only minor side lobes that are symmetric to the main peak are

3.5. One-dimensional imaging with a single partial MLL

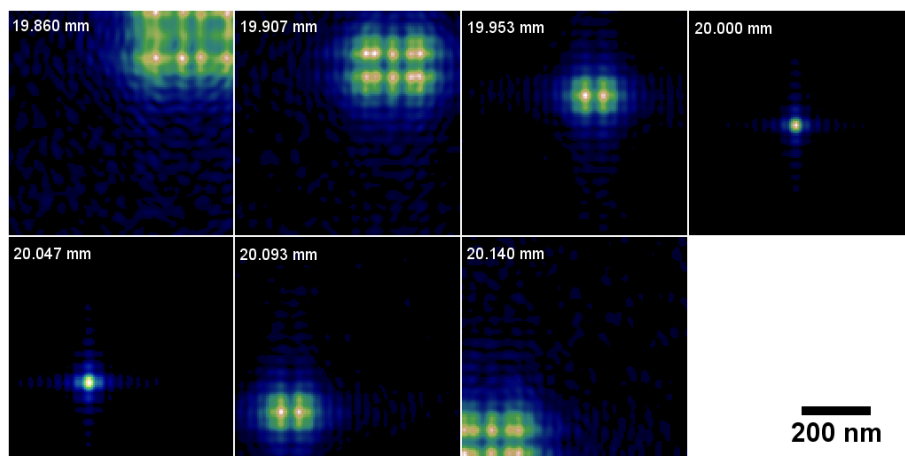


Figure 3.16.: Simulation of a focal series for an MLL of PS 6056 at 20 keV with incident parallel beam.

observed for 0% drift. Increased side lobes are observed on a particular side of the main peak in case of $\pm 0.3\%$ drift. If the drift rate is positive, they are located at in positive direction of the main peak. Such simulations can be used to fit PSF that are obtained by ptychographic reconstruction from experiments at synchrotron radiation facilities.

3.5. One-dimensional imaging with a single partial MLL

Single MLLs showing one-dimensional imaging were studied in the laboratory X-ray microscope *NanoXCT-100*. Therefore, the new lenses have to be integrated into its optical path to study their imaging capabilities with basic experiments. The experimental results shown in this section have been achieved with the MLL *5741-0* and one single lens of *6056-C2* (Table A.1).

Integration into the X-ray microscope

All existing optical elements such as condenser, pinhole, Fresnel zone plate, phase ring, and the specimen are mounted on separate 3-axis translation stages (*M-562-XYZ*, Newport corporation, Irvine, CA, USA). This allows a flexible adjustment of all components. The specimen can be rotated around its vertical axis in addition. This rotation is necessary for tomography and it allows special features of the object to be aligned in a certain orientation with respect to the beam.

It proved to be appropriate to mount the MLL onto the very stable sample stage using the specimen holder belonging to the microscope that is designed for flat samples. Thereby, the FZP can be used to place the MLL at defined positions with respect to the illumination. On the other hand, any other specimen that is going to be imaged with the MLL can be placed rather quickly in the required distance to the MLL: First, the MLL placed in the focus of the FZP and it is then temporarily moved out of beam.

3. Multilayer Laue lenses

Second, the FZP is moved upstream by the focal length of the MLL and the object is aligned to be in this focus. The FZP is moved out of beam and the MLL is moved to its former position after alignment.

Two additional motorized stages – *Newfocus 8081-M* and *Newfocus 9065-XYZ-NPP-M* (*Newport corporation*) – are available to insert additional elements inside the optical path. They offer five (X, Y, Z, θ, φ) and three (X, Y, Z) degrees of freedom, respectively, and an additional optical breadboard was mounted in vicinity of the existing stages to place both stages at arbitrary positions. However, the stage has to be positioned beside the optical path due to geometrical restrictions of the microscope. A 15 cm long extension is necessary to bridge the remaining distance. After the actual specimen had been mounted on one of both additional stages, a critical vibration caused by the length of the extension and the compliance of the stage was observed. Hence, all specimens were later on mounted onto the pinhole stage. The pinhole was moved to one of the additional stages because it has lower requirements regarding stability. This set-up is shown in Fig. 3.17.

The microscope is equipped with two different condensers. The condenser that is typically used for absorption contrast imaging has a greater angular range where light is collected. Thus, it is more efficient than the phase contrast condenser, but suffers from significantly larger background at the position where the image is generated, i.e. within the condenser ring. This value reaches almost critical magnitudes if radiographs are acquired with the $40\times$ FZP. Therefore, the phase contrast condenser was chosen for all following experiments with MLLs to explicitly study their imaging properties.

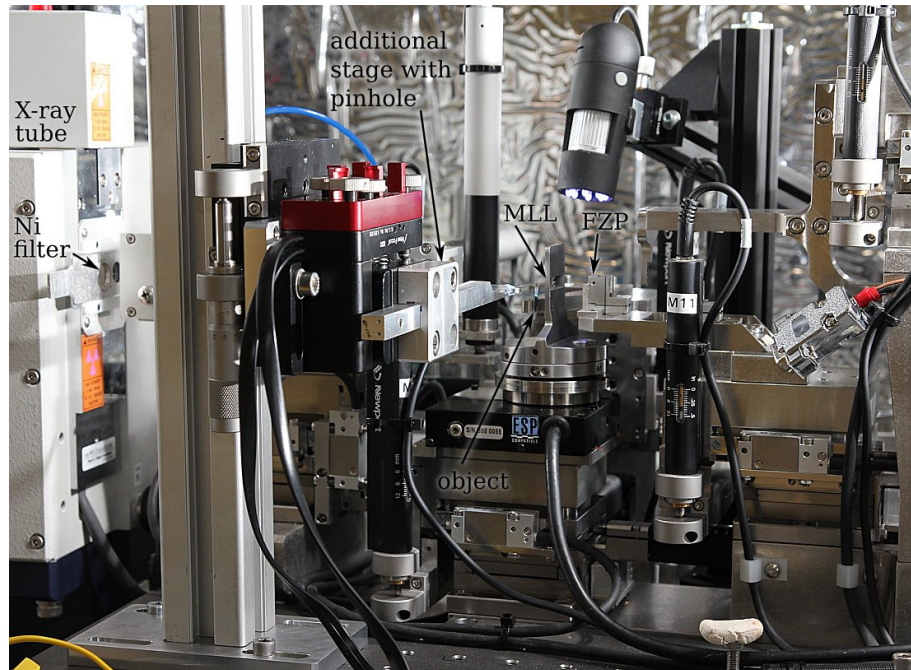


Figure 3.17.: Photograph of the X-ray microscope *NanoXCT-100* being equipped with an additional stage to integrate the MLL into its optical path.

Alignment and tilt series

Due to the alignment with the FZP, the MLL had been placed at a suitable position in terms of translation. For a single MLL, there is one essential degree of freedom left in rotation to match the optical axes of the microscope and the MLL. Tilt series of the entire lens were performed to study its optical behavior. Fig. 3.18a shows the measured image on the larger scintillating screen. If the zones of the MLL are misaligned ($\alpha = -1.12^\circ$), solely the condenser ring is observed. Once the MLL is tilted towards its optimal position ($\alpha = -0.40^\circ, \alpha = -0.08^\circ$), a bright stripe appears across the entire width of the screen and its intensity increases. It then disappears gradually with increasing angle ($\alpha = 0.36^\circ$).

This observation is in agreement with the results of the refractive simulation using *RayT* (section 3.4), see Fig. 3.18b. The stripe equals the bright-field image of the $\varnothing 70\ \mu\text{m}$ illumination at the object plane. Due to the greater magnification of the MLL compared to the FZP ($200\times$ vs. $10\times$), a larger image of the illuminated area is generated, which exceeds the size of the condenser ring. As already discussed, a single MLL acts as an one-dimensionally operating lens. The light is only distributed correctly in one direction onto the screen yielding the measured and simulated distribution of intensity.

Evidence of imaging capabilities of partial MLLs

This set-up with a single partial MLL allows first imaging experiments, if suitable specimens like gratings are used. In any case, the transmissivity should only vary in one principal direction, which has to be aligned to the orientation of the MLL. The first successful demonstration was performed at a cross section of a microprocessor chip. Fig. 3.19 shows an image that was acquired with the MLL *5741-0* and the larger scintillating screen and its corresponding radiographs taken with the $10\times$ FZP. In vertical direction starting at the top, there are transitions from air to several layers of copper interconnects being separated by a dielectric material until the silicon substrate is reached at the bottom. These materials have different transmission, which is visualized in the FZP radiograph. Regarding the MLL image, a very similar vertical distribution of intensity is recorded. The copper layers are clearly imaged as dark regions within the bright-field of the MLL.

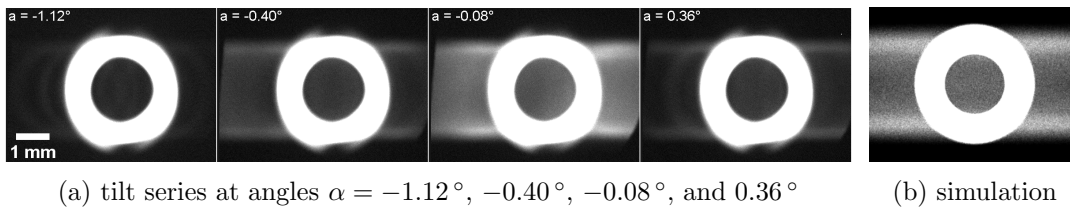


Figure 3.18.: Tilt series of the MLL *5741-0* acquired with the larger scintillating screen and a simulated image using *RayT*.

3. Multilayer Laue lenses

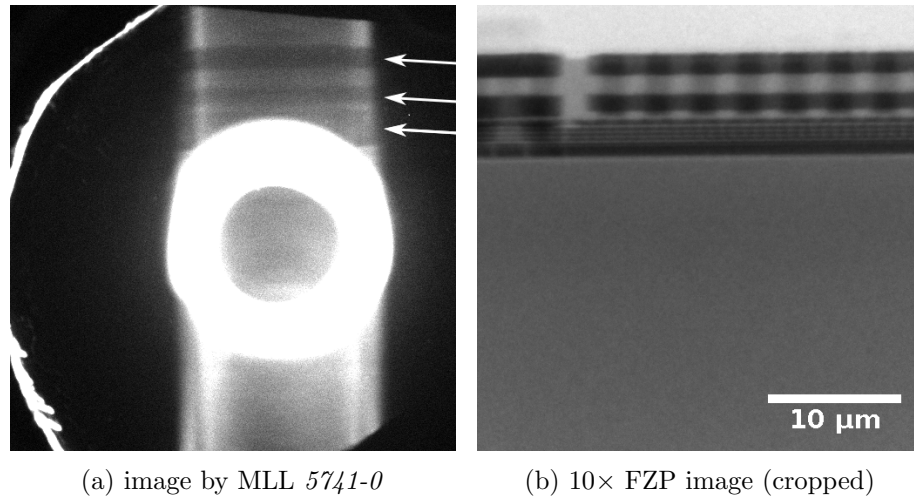


Figure 3.19.: First observation of the one-dimensional imaging capability of an MLL using lens 5741-0 and the larger scintillating screen. A radiograph of the 10× FZP is inserted for comparison. Arrows in (a) point at the positions of the dark Cu layers in the MLL image.

For the following experiments, a more suitable specimen was chosen to be imaged with an MLL. A former MLL of PS 5741 was chosen to act as a test pattern. The top-most layers have a thickness of few 100 nm. Two additional 2 μm thick layers of Al and Ni were deposited on top of them, see Figs. 3.20a and 3.20b. Therefore, they can easily be resolved with an MLL. The resolution may be estimated at thinner layers.

An MLL was prepared from deposition PS 6056 for experiments⁵. Its thickness in beam direction equals 4 μm, see Fig. 3.20c. Fig. 3.20d contains an image of the test pattern on the larger scintillating screen using this MLL for imaging. Test pattern and MLL are rotated clockwise by 90° in contrast to the previously described experiment. The pattern of the imaged multilayer appears on the right-hand side of the scintillating screen. Finally, the specimen was moved horizontally and the top-most layers of the test pattern appeared in the center of the condenser ring. The smaller scintillating screen was then used to acquire a real radiograph at this position (see Fig. 3.20e). For the sake of completeness, five images of a focal series with a range of 800 μm using the larger scintillating screen are shown in Figs. 3.20f – 3.20j.

This set-up – i.e. the image generated by the lens appears in the center of the condenser ring – complies with the conditions that are used for FZP imaging. The results yield a first evidence that MLLs can be used for imaging as well. An exact determination of the resolution was not possible since the existing stage configuration of the *NanoXCT-100* did not offer enough degrees of freedom in rotation to align the specimen precisely with respect to the optical axis and parallel to the MLL. In particular, the latter inaccuracy has a significant impact on the apparent resolution. In view of experiments with crossed

⁵This lens was assembled to the crossed lens 6056-C2 after all one-dimensional imaging experiments had been performed.

3.5. One-dimensional imaging with a single partial MLL

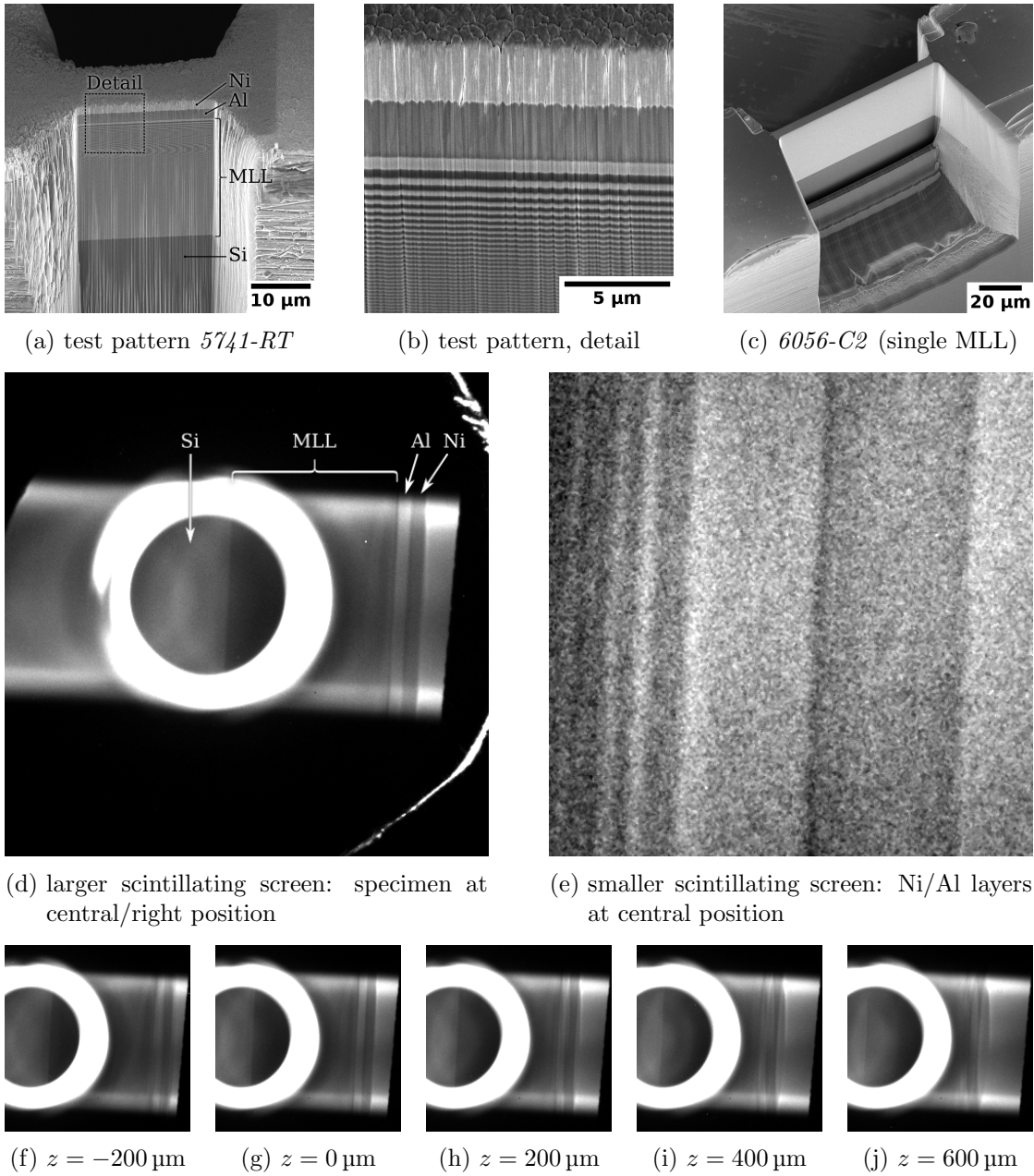


Figure 3.20.: One-dimensional imaging of a grating with one MLL of 6056-C2. (a) and (b) SEM images of the grating, being a former MLL of PS5741 that is coated with 2 μm Al and Ni. (c) SEM image of a single MLL of 6056-C2, which was used as the lens for imaging experiments. (d) and (e) One-dimensional image of the grating on both scintillating screens. (f) – (j) Cropped images of a focal series: the MLL was moved along the optical axis in z -direction.

3. Multilayer Laue lenses

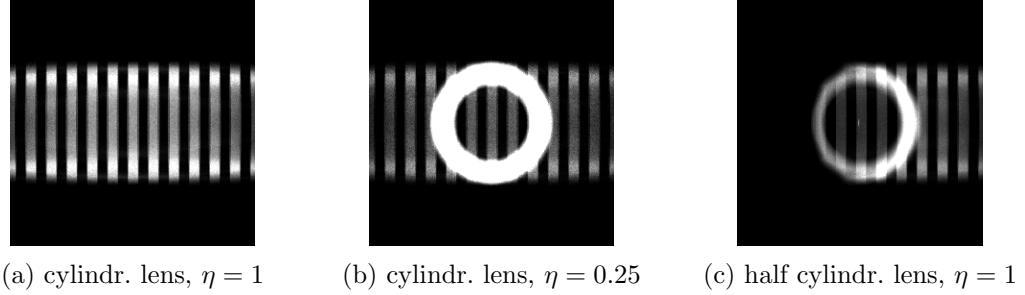


Figure 3.21.: Simulated image on the detector of a grating that is imaged with a complete or half cylindrical lens. The contrast in (b) is enhanced to emphasize the 1st order image in case of the reduced efficiency η of the lens.

MLLs, which are not affected by this inaccuracy, no further effort was made to improve the set-up for one-dimensional imaging.

Another important finding was made while the specimen was moved inside the object plane, e.g. in order to locate it or to place it in the center of the field of view. A correct one-dimensional image of the object is obtained on the right-hand side of the entire field of view and at a central position as shown in Fig. 3.20d. Once the object is moved to the other side of the field of view, its image disappears. The reason for this asymmetry of the imaging capability is the use of partial MLLs. As shown with the physical optics simulation in Fig. 3.14a, a proper PSF can only be expected on one side of the optical axis in this case. Hence, simulation and experimental results are in accordance.

This fact cannot be simulated with the refractive simulation. Three simulations were computed and a periodic linear grating of transparent and opaque regions was used as object that is imaged with a cylindrical lens to the detector. If the MLL is modeled as a complete cylindrical lens, the image of the object appears on the entire field of view as expected (Fig. 3.21a). The condenser ring appears if the efficiency of the lens is reduced to $\eta = 0.25$, see Fig. 3.21b. The cylindrical lens is cut at the optical axis to approximate a partial MLL, which was used in the experiments. The simulated image on the detector differs significantly from real experiments, because the bright stripe is only observed on one side of the optical axis in the simulated image and no intensity is seen on the other side (Fig. 3.21c vs. Fig. 3.20d).

Hence, both simulations are able to contribute to a better understanding of the experimental results. The general appearance of the bright-field of a single MLL can be well described with the refractive simulation because all optical elements from source to detector are considered. The physical optics simulation provides complementary results about the expected PSF and real imaging capabilities.

Investigation of complete MLLs

So far, only partial MLLs were tested. It was not intended to fabricate a multilayer coating that contains all zones on both sides of the optical axis. The major reasons

3.5. One-dimensional imaging with a single partial MLL

for this decision are concerns regarding the precision of the multilayer deposition if all thicker zones are incorporated, the impossibility to realize a tilted MLL since both halves have to be tilted contrarily, and issues of accumulated roughness [KB14].

Thus, complete MLLs can be fabricated as an assembly of two partial MLLs. First approaches to realize them experimentally are described in section 3.2. The obtained lens is mounted onto the holder for flat specimens and coarsely aligned inside the X-ray microscope using the built-in FZP. To study both partial lenses individually, a $\varnothing 200\ \mu\text{m}$ tungsten wire was inserted into the optical path as close as possible downstream the lens assembly. It was mounted on one of the additional stages. The tungsten wire is utilized to cover one partial lens, e.g. to acquire tilt series or to perform imaging experiments with one of both partial MLLs.

The relative tilt of both partial MLLs can be determined, if tilt series are analyzed. In a first attempt, an offset of 0.8° was measured. This value is expected to be too large, because diffraction behavior changes significantly within this angular range (cf. Fig. 3.18a). Both MLLs were released from the holder and cleaned carefully. Thereby, the offset was reduced to 0.1° . The stage was rotated to the central position.

A former MLL of PS 5741 was used as a test pattern as described for the previous experiments. Focal series and final alignment of the specimen were done using one of both partial MLLs, while the second MLL is covered with the tungsten wire. Its image appears in the center of the condenser ring and the smaller scintillating screen can be used to acquire the radiograph. A corresponding radiograph of the second MLL is obtained by covering the first MLL with the wire.

If both radiographs are overlaid, a horizontal offset of 31 px is observed, see Fig. 3.22. This offset is influenced by two major reasons. First, the remaining error of the adjusted interspace between both partial lenses yields a shift of the image that is equal to the value of this error multiplied with the magnification. Therefore, it can directly be measured if

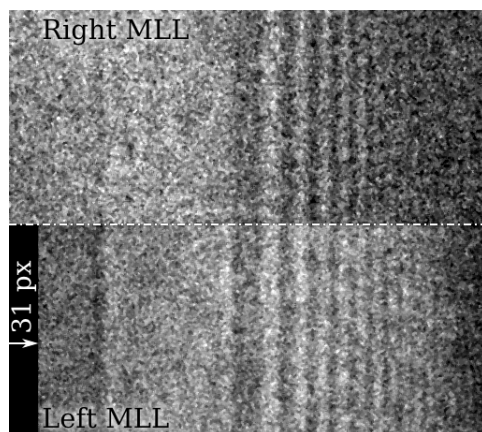


Figure 3.22.: Vertical composition of individual images of both partial MLLs of a complete MLL. The image of the left MLL was shifted by 31 px to the right to overlay both partial images correctly.

3. Multilayer Laue lenses

the pixel size of the image is calibrated to real values, resulting to approximately 410 nm in this case. Second, any offset from the focus position shifts both images relative to each other. This is caused by the asymmetric shape of the PSF of a partial MLL along the optical axis. It turned out that both effects cannot be separated by any straight-forward approach. Therefore, the initial plan to iteratively refine the interspace inside the SEM was stopped. Further experiments with complete MLLs are supposed to be done with the designed piezo stage in future (see section 3.2).

If no partial lens is covered, a common image is recorded. It almost equals the sum of the intensities of both individual images and no visible improvement or other effect due to the combination of two diffractive lenses is observed. This behavior is expected because the alignment error is significantly greater than the resolution, what will unlikely result in interference effects.

However, several concerns emerged if complete MLLs are suited in general for X-ray focusing and imaging, though the global diffraction efficiency might be doubled easily and a better resolution might be gained. This will be discussed in section 5. In any case, one-dimensional experiments are important to obtain basic experience in terms of MLL alignment and of interpretation of several findings. The developed methods typically rely on tilt series. They provide the basic experimental methods for advanced characterization of new multilayer coatings in general and in particular for individual lenses, such as the measurement of relative layer tilts for wedged MLLs or the general evaluation of MLL fabrication.

3.6. Full-field imaging with crossed partial MLLs

The one-dimensional imaging experiments proved the general capability of MLLs to act as imaging optics. A two-dimensional imaging behavior is mandatory for real application. It was shown in section 3.4 that crossed MLLs show a suitable PSF and proper imaging can be expected. On the other hand, it should be reminded that each of both crossed MLLs is a diffractive lens with a limited efficiency and both lenses are assembled in series. Thereby, mixed orders might appear and this typically results in serious background intensity. A major drawback of the physical optics simulation is the insufficient calculation of such minor intensities that are spread over a large area. Hence, these effects might not be recognized at all.

Simulation of mixed-order imaging with serial diffractive lenses

Refractive simulations using *RayT* were executed to get a better understanding of the expected imaging properties. The existing model for 1D imaging was extended by a second cylindrical lens that is placed in close distance downstream and perpendicular to the existing lens. Its focal length is slightly greater than the focal length of the first lens to achieve matching of both focal planes. Hence, the magnification in horizontal

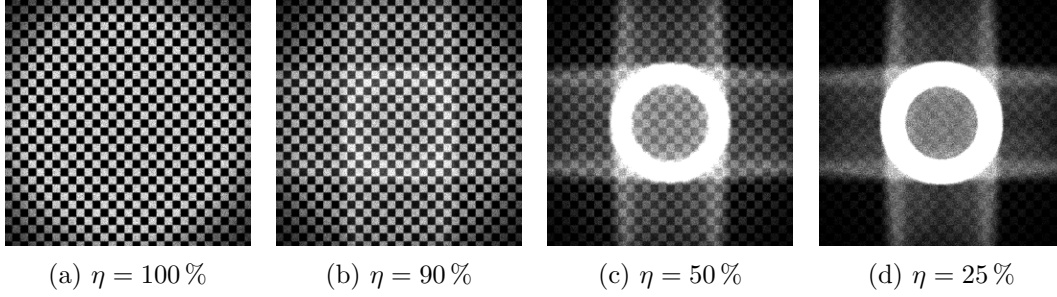


Figure 3.23.: Simulated distribution of the intensity on the detector if a chessboard-like pattern is imaged with crossed cylindrical lenses having different efficiencies η .

and vertical direction differs by less than 1%, what will have negligible effect on the actual image. The linear grating is replaced by a chessboard-like grid of opaque and transparent areas. The probability η that incoming rays are refracted by each lens was varied to account for the limited efficiency of both diffractive lenses. Fig. 3.23 shows a collection of simulated images at the detector for different values of η .

If all rays are refracted ($\eta = 1.00$), the lens assembly operates like a spherical lens and a large bright-field is obtained. The observed pattern changes significantly with decreasing η . Basically, the well known stripes that represent a bright-field image of a single MLL as well as the condenser ring appear again, and they get more pronounced. The image weakens simultaneously. This behavior can be explained if the result is understood as an overlay of different orders of both lenses. For each lens, a certain amount of intensity passes the lens in zero-order without interaction. The remaining part is refracted, and therefore, it is imaged correctly in the corresponding direction. All rays can be classified in four categories, if higher orders are neglected:

- 0-0: rays passing both MLLs in 0th order, fraction = $(1 - \eta)^2$;
- 0-1: rays passing the horizontal MLL in 0th order and the vertical MLL in 1st order, fraction = $\eta(1 - \eta)$;
- 1-0: rays passing the horizontal MLL in 1st order and the vertical MLL in 0th order, fraction = $\eta(1 - \eta)$;
- 1-1: rays passing both MLLs in 1st order, fraction = η^2 .

The detector can be virtually equipped with a filter to separate the images that are generated by each order for a better understanding, see Fig. 3.24. Direct beams (0-0) generate the condenser ring, while beams that are refracted by exactly one lens (0-1, 1-0) yield the already known stripes in vertical and horizontal direction, respectively. The object is only partially imaged in these orders due to their one-dimensional operation. In particular, the chessboard-like pattern is not visible. This is caused by the fact, that in contrast to a linear grating, the average transmission in horizontal and vertical direction

3. Multilayer Laue lenses

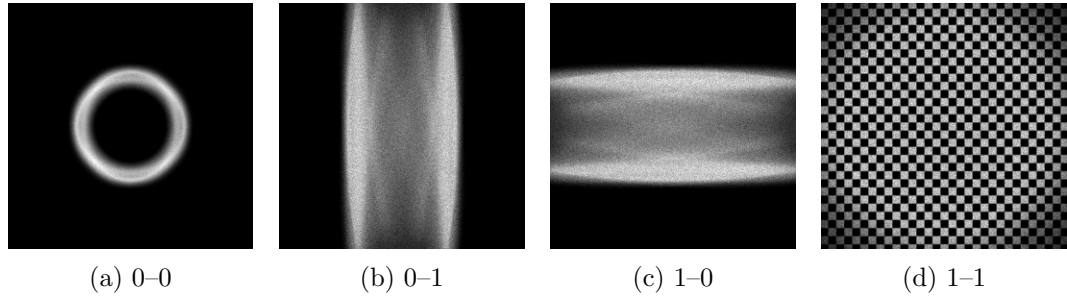


Figure 3.24.: *RayT* simulations for imaging with crossed cylindrical lenses. Each image contains the image that is generated by a specific order.

is independent of the position. All remaining beams (1-1) will be imaged correctly in both dimensions and the image of the object is measured. The eventual image on the detector can be generated if the images of each category are add up and weighted accordingly.

It is obvious that most regions of the detector contain a mixture of images of different orders. All orders appear in the region of the condenser ring, while all orders except 0-0 are present inside the condenser ring. Thus, the actual 1-1 image is overlaid by a significant background (0-1, 1-0). The background itself depends on the object due to the one-dimensional imaging. It is therefore not possible to remove the background with a subtraction of some known, static distribution of intensity.

The regions in all four corners apart the areas of the condenser ring and both 0-1/1-0 stripes are only illuminated by 1-1 beams and a correct image can be expected at these positions. It was shown in sections 3.4 and 3.5, that each MLL only shows proper imaging on one side of the optical axis. Hence, the four corners can be classified to one corner, where both MLLs show a bad PSF; two corners along a diagonal, where exactly one of both MLLs has a suitable PSF; and a single corner, where both MLLs show proper imaging. Finally, combining both results, there is a single corner where a real image might be found without background.

Evidence of full-field imaging

The following imaging experiments were carried out using the lens *6056-C2* (Table A.1). Its alignment is equivalent to the alignment of an one-dimensionally operating lens. In addition, the vertically imaging lens has to be tilted to the correct position. A manual tilt axis was realized with a fine-thread screw inside the bottom of the specimen holder without further ado. Thereby, the entire holder can be tilted in a sufficient range and the correct alignment is found with few iterations.

The resulting bright-field of crossed MLLs is shown in Fig. 3.25. This image agrees well with the *RayT* simulation. Hence, two crossed stripes are observed and – in difference to the one-dimensional case – some intensity is noticed in all corners.

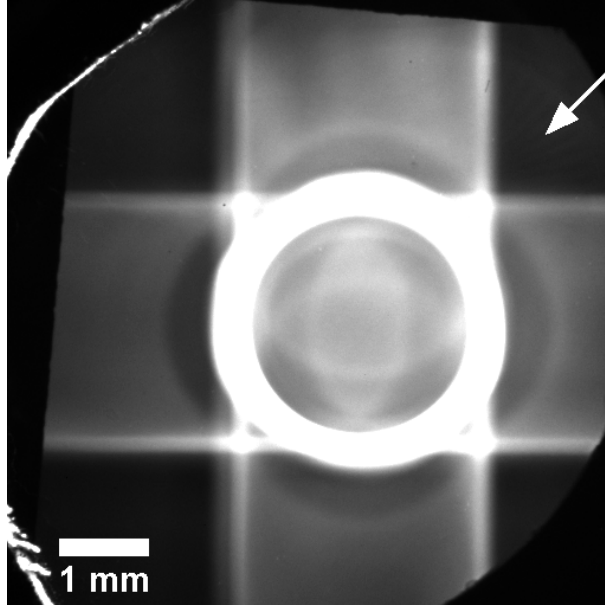


Figure 3.25.: Bright-field image of crossed MLLs acquired with the larger scintillating screen. The arrow points the corner where the image was found.

The imaging properties are demonstrated at X-ray test patterns according to custom. Such specimens exhibit a Siemens star test pattern, which is used to determine the resolution and aberrations of an optical system. At first, the standard test pattern *X50-30-0* (*Xradia Inc.*, Pleasanton, CA, USA) belonging to the X-ray microscope *NanoXCT-100* was used. For some reason, the pattern was degraded, and therefore, its application was restricted. A flawless *ATN/XRESO-50HC* (*NTT-AT*, Tokyo, Japan) was used for final experiments [ATN50].

After the test pattern had been inserted into the microscope and coarsely aligned with the built-in FZP, its image appeared in one distinct corner (cf. arrow in Fig. 3.25). The $\varnothing 60\ \mu\text{m}$ pinhole was replaced by a custom-built $12 \times 33\ \mu\text{m}^2$ pinhole to further truncate the illumination. The smaller scintillating screen was centered to the position in the corner⁶ in preparation of the real imaging experiments. Supplementary radiographs were acquired with the $40\times$ FZP and the $\varnothing 60\ \mu\text{m}$ pinhole for the purpose of comparison.

Two radiographs of the center of *X50-30-0* are shown in Fig. 3.26. For each image, 16 radiographs each with an acquisition time of 450 s were recorded at binning 2 ($512 \times 512\ \text{px}$) and binning 1 ($1024 \times 1024\ \text{px}$) for MLL and FZP, respectively. Different binning is related to the unequal fields of view of both lenses – $(6.86\ \mu\text{m})^2$ vs. $(16.5\ \mu\text{m})^2$ – yielding more similar pixel sizes of both radiographs. For comparison, the radiograph of the FZP was cropped and scaled to virtually match both magnifications. A slight drift occurred during the rather long total exposure time of 120 min. Therefore, a drift correction according to appendix B (p. 107) was applied to the reference corrected series

⁶The entire detector unit is mounted on a cross table and can be moved perpendicular to the optical axis.

3. Multilayer Laue lenses

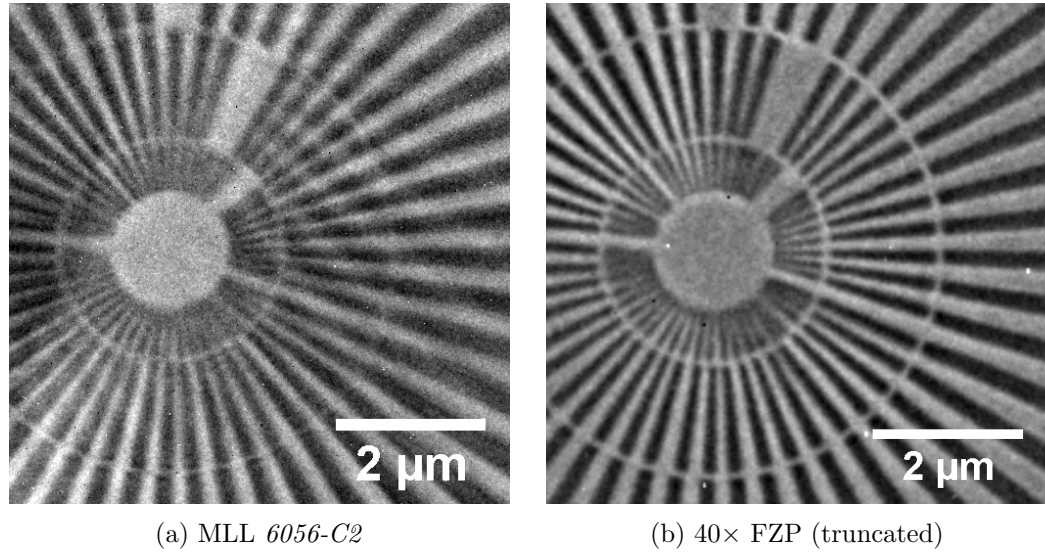


Figure 3.26.: Radiographs of the center of the Siemens star test pattern *X50-30-0*.

of radiographs prior to averaging. All image processing was done in *ImageJ* [Ras13].

It is obvious that both crossed MLLs act as an imaging lens: The center of the Siemens star pattern is visible in the radiograph (Fig. 3.26a). In comparison to the image of the FZP, similar features of the test pattern are resolved, such as some collapsed and some free-standing bars in the inner ring. The evaluation of the focal series indicated that the adjustment of both focal lengths was not entirely successful. Astigmatism is observed because vertical and horizontal features show their best image in different focal planes, which have a distance of approximately 20 μm . This distance exceeds the depth of focus of $\pm 9 \mu\text{m}$ (eq. 2.14) and the radiograph was acquired at an intermediate position. The offset originates from known imperfections of the preparation of the lens.

It is remarkable that the radiographs seems to be overlaid by another pattern that is visible on closer inspection. Some streaks appear in particular in the dark regions. These features look like a part from another position of the Siemens star pattern. Therefore, it seems that a kind of *ghost image* of the specimen overlays the real image with a certain displacement.

Detailed analysis

Fig. 3.27 shows three cropped radiographs of an outermost region of the second Siemens star pattern (*ATN/XRESO-50HC*). In contrast to the previous experiment, an additional image was acquired using crossed MLLs and the 10 μm nickel filter. This optional filter is installed downstream the X-ray shutter to suppress Cu-K β radiation. Similar artifacts are observed without filter, if the MLL is used (Fig. 3.27a). Hence, there is evidence to suggest that this behavior is inherent for this configuration. The FZP image (Fig. 3.27c) is not affected by such an artifact and it was never observed in previous experiments.

3.6. Full-field imaging with crossed partial MLLs

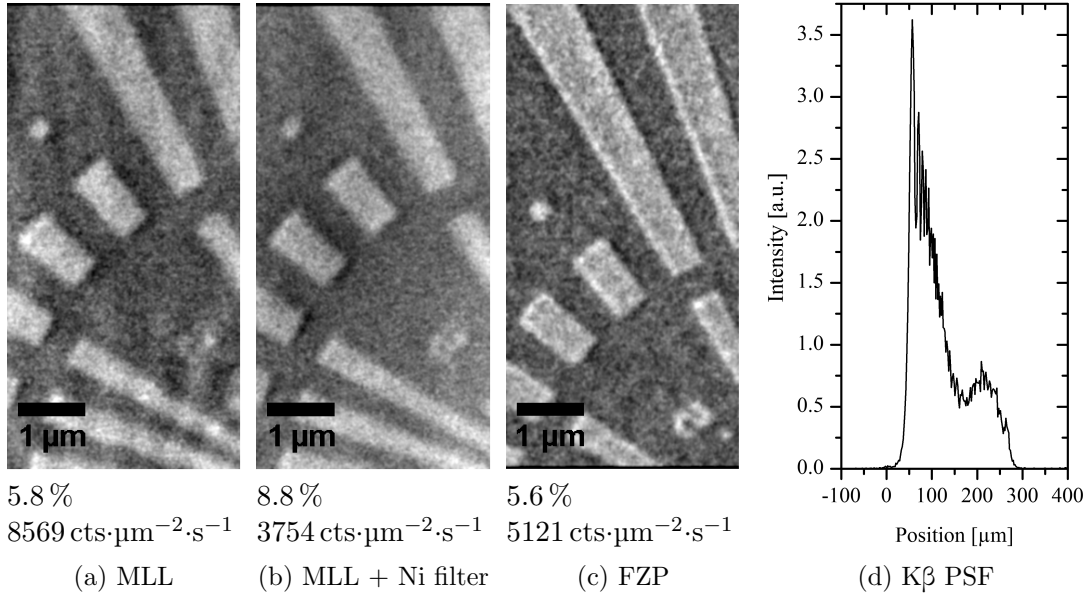


Figure 3.27.: Radiographs of *ATN/XRESO-50HC* [Nie+14b]. The values stated below are the measured absorption of the tantalum layer and the flux in the bright-field. (d) shows the image of a point source ($y = 0$) in the image plane in case of $K\beta$ imaging.

However, the *ghost image* is efficiently suppressed if the nickel filter is used (Fig. 3.27b). It was already described in section 2.3 that only a moderate filtering of rather high and low energies is carried out in the illumination unit. On the other hand, diffractive lenses are highly achromatic and only characteristic radiation offers a suitable brilliance for decent imaging. $K\beta$ radiation has a lower intensity than $K\alpha$ radiation. This explains the weak appearance of the *ghost image*, which is assumed to be caused by $Cu-K\beta$ radiation ($E = 8.90$ keV). Using the nickel filter, the $K\alpha/K\beta$ ratio is increased⁷ by a factor of 8.0. With regard to the immediate suppression of the *ghost image* due to the use of the filter, an image caused by $Cu-K\beta$ radiation seems to be a valid explanation for this effect. Fig. 3.27d shows the simulated image of a point source located at the object plane being imaged with $Cu-K\beta$ radiation to the scintillating screen. The simulation was performed with *MLL.i* (section 3.4). Though the image plane is not in focus, the main peak has a real FWHM of $67 \mu\text{m}$. This equals $0.72 \mu\text{m}$ within the radiograph, if it is scaled with the magnification of the $K\alpha$ image. Thus, sub-micron features such as broader lines of the Siemens star pattern can be resolved – what is in agreement with the experimental data.

Further analysis of the acquired micrographs and the reference images is done to determine some basic imaging properties of the crossed MLLs. The pixel size of the radiograph at binning 2 was determined to be 13.4 nm. Thus, the optical magnification equals $M = 93$. The measured intensity on the detector in absence of any specimen allows a qualitative evaluation of the global diffraction efficiency of the lens. The flux

⁷Transmission through $10 \mu\text{m}$ of Ni for $Cu-K\alpha$ and $K\beta$ radiation is 0.660 and 0.082, respectively [Gul10a].

3. Multilayer Laue lenses

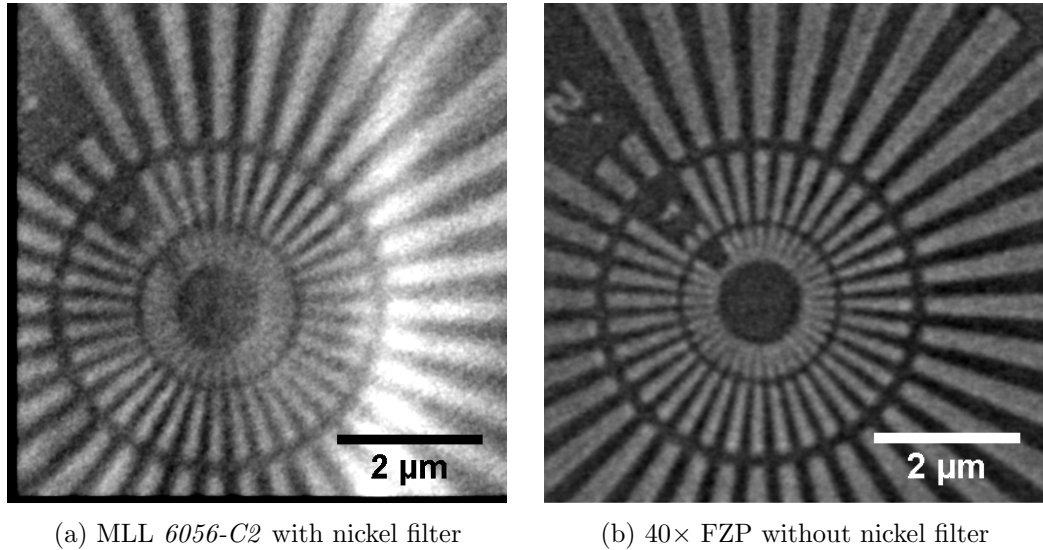


Figure 3.28.: Radiographs of the center of the Siemens star pattern *ATN/XRESO-50HC* [Nie+14b].

is normalized to a certain area inside the object plane and to time to compare both lenses. Without nickel filter, the MLL collects two thirds more photons than the $40\times$ FZP ($8570\text{ cts}\cdot\mu\text{m}^{-2}\cdot\text{s}^{-1}$ vs. $5120\text{ cts}\cdot\mu\text{m}^{-2}\cdot\text{s}^{-1}$). This is remarkable because the FZP has a diameter of $80\mu\text{m}$ what leads to a 2.3 times larger aperture where light can be collected. The flux is decreased to $3750\text{ cts}\cdot\mu\text{m}^{-2}\cdot\text{s}^{-1}$, if the nickel filter is used.

The measured absorption of coarse features of the Siemens star inside the radiograph provides complementary information. Any background radiation that is not imaged correctly onto the detector reduces this value. The test pattern is etched into a 500 nm tantalum layer that is deposited onto a membrane. Hence, the theoretical absorption using $\text{Cu-K}\alpha$ radiation is 12.3% [Gul10a]. To account for the membrane, the absorption is calculated as the decrease of intensity from etched regions to the remaining tantalum pattern. Without nickel filter, MLL and FZP show a similar value of 5.8% and 5.6% , respectively. Thereby, the images of both lenses are assumed to have a comparable amount of background. The measured absorption using the MLL is enhanced to 8.8% using the nickel filter, and background was obviously reduced. This finding is in agreement with the suppression of the *ghost image*.

Fig. 3.28 shows two radiographs of the center of the Siemens star to finally compare both lenses. The MLL radiograph was acquired using the nickel filter because it proved to be mandatory. The noticeable bright stripe on the right-hand side of this image is caused by an accidental drift of the pinhole while the reference images had been measured. Hence, this artifact is neglected in the further discussion.

In contrast to Fig. 3.26a, aberrations of the MLL are better observed in this radiograph, because the *ghost image* is suppressed and the test pattern is assumed to be flawless. The FZP has a slightly better resolution from visual impression, as more details are visible especially in the innermost ring ($50 - 100\text{ nm}$ lines and spaces). In addition,

3.7. Characterization of MLLs using synchrotron radiation

small dots appear less clearly in the MLL image. It is assumed that these aberrations are mostly related to the astigmatism due to insufficient matching of focal lengths of both crossed MLLs and a remaining error in the perpendicular alignment of both lenses. In addition, a stronger drift correction of the acquired series of radiographs was necessary in case of the MLL. This is mainly related to the uncommon usage of the stages and the provisional mounting of the MLL itself. It is also known that the multilayer coating exhibits some deviations from the zone plate law, which result in side lobes of the PSF (cf. sections 3.2 and 3.3, and Fig. 3.15a).

To summarize the results, it was shown that full-field X-ray microscopy can be done with crossed partial multilayer Laue lenses. The tight assembly of both partial MLLs to a single lens element yields a practical solution for lens adjustment inside the microscope and provides a virtually undistorted image due to a focal length variation of less than 0.5%. Background due to mixed order imaging of both serial diffractive lenses is a significant issue, but there are several positions where the actual image is separated from other orders. Regarding the directional imaging of the partial MLL, a single corner inside the image plane emerges, where a suitable image is found. To suppress a *ghost image* of the object, which is apparently caused by Cu-K β radiation, it is mandatory to use a nickel filter. The imaging quality is close to the quality being achieved with commercially available FZPs. There are several known flaws of these first experiments such as an astigmatism of the crossed MLLs, imperfections of the multilayer stack and lens assembly, and stability issues of the experimental set-up. These issues limit the achievable performance and they have to be avoided in future.

3.7. Characterization of MLLs using synchrotron radiation

It is obvious to study the optical properties of multilayer Laue lenses at synchrotron radiation facilities. X-ray focusing will be a main application of this kind of X-ray lenses and it is to date limited to synchrotron radiation anyway. Furthermore, special methods such as ptychography [Sch+10b] are available. Thereby, it is possible to reconstruct the complex wave field at the position at the specimen. Subsequently, the PSF of an arbitrary lens can be calculated and imperfections such as side lobes are directly observed. These experiments yield practical experience to what extent the present MLLs can be used for general studies. In addition, the results provide useful information to advance the fabrication of MLLs.

The experiments were conducted at *PETRA III* in Hamburg, Germany, at the hard X-ray micro/nano-probe beamline *P06* [Sch+10a] and at *ESRF* in Grenoble, France, at the microfocus beamline *ID13* [RBD10; DBR09; DBR06]. A comprehensive list of all beamtimes is given in the appendix in Table A.2. This section collects a set of tools that were developed in this thesis to optimize the experiments. In addition, those findings are discussed that give a feedback to the preparation of the multilayer coating to actual lens elements as described in section 3.2.

3. Multilayer Laue lenses

Experimental set-up

The experimental set-up of an X-ray nanoprobe beamline will be briefly described on the basis of beamline *P06*, which is typically equipped with refractive nanofocusing lenses (NFLs, cf. section 2.2). More detailed information is provided in [Sch+10a] and [Kub+14]. An one-dimensional scheme of the optical components in the experimental hutch is given in Fig. 3.2. The X-ray beam is emitted by an undulator. A prefocusing optics may be used to focus the coherent fraction of the beam into the aperture of the lens. A set of slits finally truncates the beam to the size of the aperture of the MLL. Two five axis nanopositioning stages are available to align two individual vertically and horizontally focusing X-ray lenses with respect to each other and to the beam. Only one set of these stages is necessary in case of pre-assembled crossed MLLs. A pinhole acts as an OSA to separate the first focusing order from other radiation. The specimen is placed at the focus position onto three axis translation nanopositioning stages, which enable raster scans.

The detector stage is equipped with several detectors. An optical microscope is used to coarsely align specimens. An X-ray live camera (*pc0.4000*, *PCO AG*, Kelheim, Germany⁸) is used to acquire X-ray transmission images, e.g. during lens alignment. The resulting X-ray flux can be measured with a PIN diode, while the incident flux downstream the slits is monitored with a transmission diode. An X-ray fluorescence detector is placed beside the specimen to acquire fluorescence spectra and a counting pixel detector (e.g. *Pilatus 300K*, *DECTRIS Ltd.*, Baden, CH) is placed approximately 2 m downstream the specimen to acquire far-field diffraction patterns during scanning X-ray microscopy experiments. At first, one of both NFLs was replaced with an MLL for initial experiments to gain experience with alignment and analysis. Finally, both individual lenses had been removed and crossed MLLs were installed.

Knife-edge scans

Knife-edge scans are performed to locate the focus in all three dimensions. If two individual lenses are used, vertical and horizontal scans at several positions along the optical axis are necessary to determine the focus position of each lens and to subsequently align both to the same spot. A custom-built cross of two $\varnothing 50\ \mu\text{m}$ gold wires is available at the beamline for this purpose. Though this is a suitable approach to align NFLs, which exhibit rather long focal lengths and depths of field, they showed limited ability for the alignment of MLLs.

A precisely shaped corner of an 80 nm thin gold layer was identified as appropriate test pattern for knife-edge scans. This solution is in agreement with other studies, where similar specimens were used (e.g. [Sch+05b]). The coated wafer was cleaved to an approximately $4 \times 8\ \text{mm}^2$ large piece. One corner had been covered by a protective

⁸combined with a visible light microscope from *Optique Peter*, Lentilly, France, which is equipped with a scintillating screen

3.7. Characterization of MLLs using synchrotron radiation

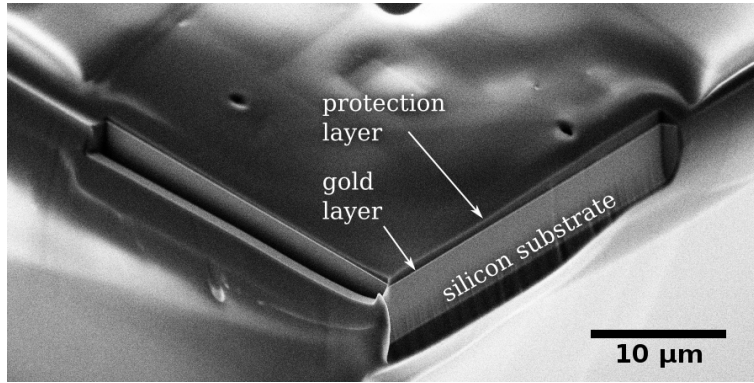


Figure 3.29.: SEM micrograph of the new test pattern for knife-edge scans.

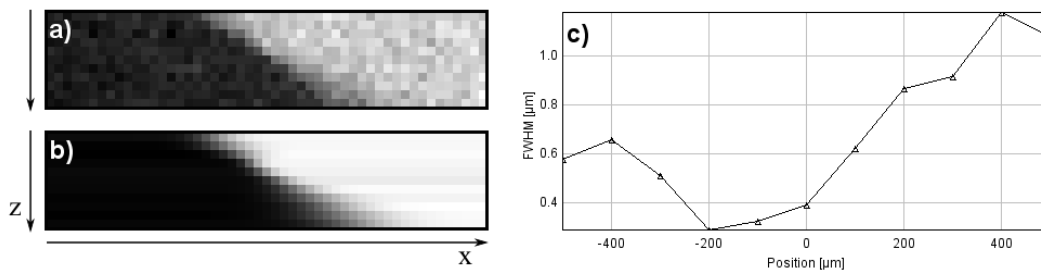


Figure 3.30.: Advanced evaluation of a series of knife-edge scans across a gold edge in x direction along the optical axis in z direction: (a) experimental data, (b) fit, (c) fit value of FWHM of the transition vs. position along optical axis.

layer and both edges were shaped by FIB. The obtained 30 μm long sections offer well defined edges for vertical and horizontal knife-edge scans, see Fig. 3.29. In contrast to the wire cross, both edges are in the same focal plane what is in particular beneficial regarding the shorter depth of focus of the MLLs.

As a consequence of the small thickness of the gold layer, it is now mandatory to use the fluorescence detector instead of the PIN diode. In general, this data has a worse signal to noise ratio. For this reason and to reduce the subjective influence of the person who evaluates the data, an automated analysis of the acquired knife-edge scans was developed and implemented in an *ImageJ* plugin called *Eval Knife Edge*, which will be briefly described (for source code, see appendix B, p. 112).

All knife-edge scans are stored as maps in *EDF* bitmap files. Each pixel represents a single data point and the measured intensity is typically saved as a 16 bit integer value. Pixel sizes and origin of each *EDF* image are automatically assigned once the file is loaded. Fig. 3.30a shows an example of a scan. To find the focus, several line scans are performed at different positions along the optical axis. Each row of the image corresponds to an individual knife-edge scan across the edge. The algorithm evaluates each line scan individually. The intensity profile is fit to an error function

3. Multilayer Laue lenses

$$I = A \operatorname{erf} \left(\frac{x - x_c}{w} \right) + I_0 \quad , \quad (3.11)$$

where A scales to the amplitude of the transition, x_c equals the center position, w is a measure of the width of the transition, and I_0 determines the offset. The FWHM of the transition equals $1.665 w$. The fit of the image is shown in a new window. It can be visually compared to the original data to exclude erroneous results (Fig. 3.30a vs. 3.30b). A plot of the determined FWHM vs. the position of the specimen along the optical axis is shown as a final result (Fig. 3.30c). The focus is located at the position of the minimum and a refined series of knife-edge scans can be repeated there. The application of this plugin showed good results during experiments at the beamline in comparison to the previously used approach. The analysis itself is now user-independent and the time to evaluate knife-edge scans is significantly reduced.

Experimental results and their feedback to the fabrication of MLLs

Radiographs being acquired with the X-ray live camera are used to perform an initial alignment of the lens at a photon energy of 20 keV. The camera is positioned few centimeters downstream the lens. Parallel beam illumination can be assumed and in general a transmission image is obtained. The radiographs reveal the same imperfections of the lens elements like laboratory X-ray microscopy (see section 3.3). Each MLL has to be tilted accordingly with respect to the optical axis. Once the lens is tilted, extinction patterns are observed inside the aperture of the MLL. The diffracted intensity is observed at estimated positions inside the image. It is evident that the apparent extinction is related to the light that is diffracted for instance in a first-order focus. Finally, the lens is aligned until a suitable first-order focus is observed on the detector. Fig. 3.31 shows radiographs of two lenses from different coatings having the same thickness in beam direction of $10.5 \mu\text{m}$. An even extinction along the height of the multilayer stack is observed in case of *6056-4* (Table A.1). The lens *6359-FC* has a different behavior as only a rather narrow extinction band is observed. The band moves towards thicker or thinner zones if the lens is tilted. This is a clear indication, that volume diffraction occurs. Thus, only a part of the multilayer is able to properly contribute to the X-ray focus, which is related to the thinner layers of this coating compared to PS6056 (cf. Table 3.1). In addition, the band is slightly curved. This observation is in agreement with the observations in laboratory XRM (Fig. 3.31d; cf. section 3.3).

Fig. 3.32 shows results for three lenses [Kub+14]. The PSF for the MLL *6056-C2* is of special interest with regard to the full-field imaging experiments shown in section 3.6, where this lens was used, too. The FWHM of the main peak in both principal directions equals $42 \times 47 \text{ nm}^2$. It can be assumed that the astigmatism is reduced at these conditions due to the higher photon energy of 20 keV, where a larger offset in beam direction is needed, and the depth of focus is increased to $\pm 22 \mu\text{m}$ (eq. 2.14). In any case, the determined focus size provides a good estimation of the expected resolution of the

3.7. Characterization of MLLs using synchrotron radiation

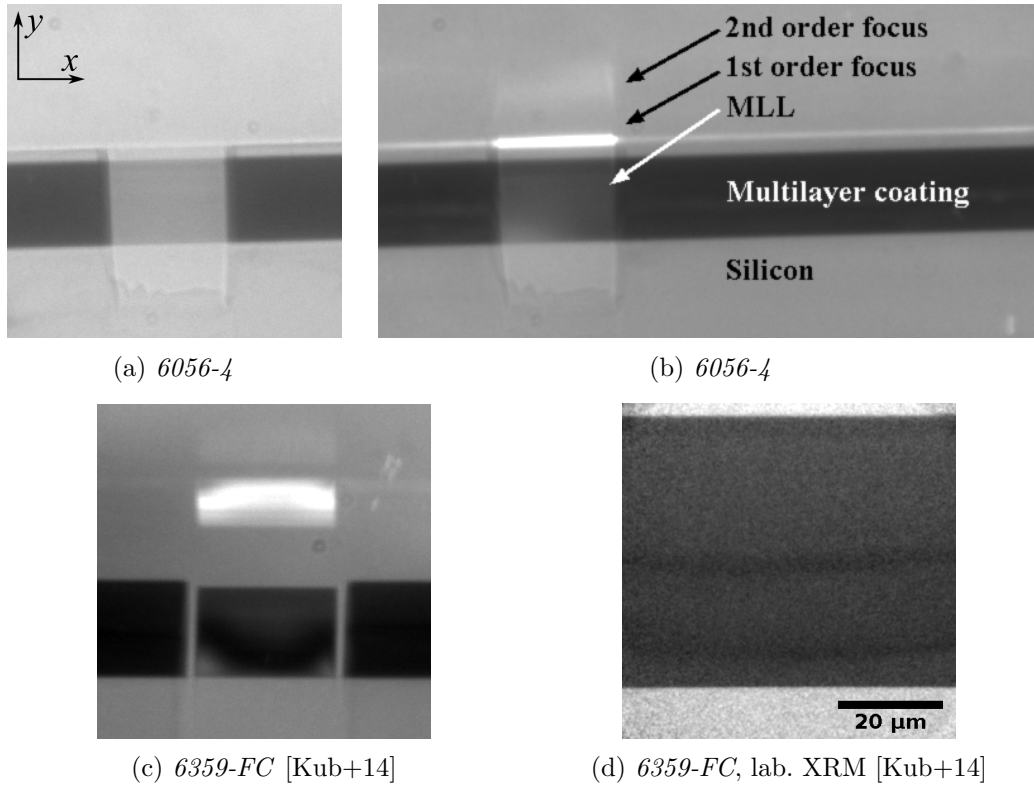


Figure 3.31.: X-ray live camera images of MLLs: (a) Reference without diffraction effects. MLLs are tilted to maximum intensity of 1st order focus in (b) and (c). A radiograph of the central area of *6359-FC* acquired with laboratory XRM is shown in (d): similar bent contours are seen like in (c).

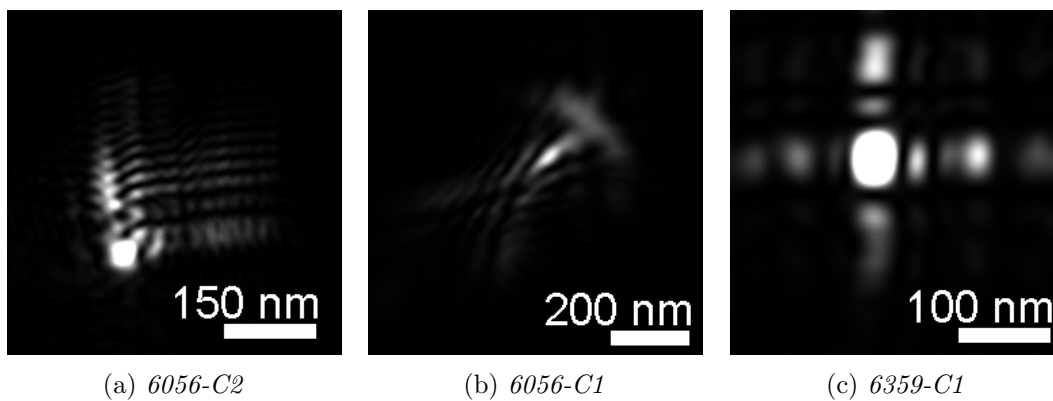


Figure 3.32.: Reconstructed PSF by ptychography of different crossed MLLs [Kub+14].

3. Multilayer Laue lenses

lens. Furthermore, side lobes are visible on one side of the main peak in both focusing directions. According to the physical optics simulation shown in Fig. 3.15b, these side lobes are a clear indication that the coating is affected by the estimated drift of the deposition rate. The PSF for the lens *6056-C1* appears differently and less clearly than the latter one. More side lobes are observed diagonal to the main peak. It is assumed that the perpendicular alignment of both single MLLs is insufficient. The PSF for lens *6359-C1* has almost symmetric side lobes. Thus, it is concluded that the drift correction approach for the magnetron sputtering process improved the focusing characteristics.

3.8. Wedged MLLs

It was already described, that volume diffraction effects have to be employed to reach ultimate resolution of diffractive lenses. Each zone has to follow an elliptical path to comply with a local Bragg condition at each position (cf. section 2.2, [Sch06]). Otherwise, the accepted thickness of the lens tends to zero and efficiency will become negligible [Yan+10]. Since the focal length of real optics is long against their thickness, the elliptical path can be linearized leading to a wedged geometry of the multilayer stack [Con+08]. The necessary tilt of a zone that has a distance h' from the optical axis results from the Bragg equation and can be approximated by

$$\theta(h') = \frac{h'}{2f} \quad . \quad (3.12)$$

The slope equals

$$s_\theta = \frac{d\theta}{dh'} = \frac{1}{2f} \quad . \quad (3.13)$$

It is typically expressed in $\text{mrad} \cdot \mu\text{m}^{-1}$. Such a linear incline can be realized if a strong thickness gradient is incorporated during layer deposition [Con+08; Con+11]. However, such a deposition is fixed to be operated at a certain photon energy. In addition, requirements regarding precise thickness control are expected to be in conflict with measures to achieve the gradient.

Table 3.5.: Materials parameters used as input for FEA.

Material	Young's modulus [GPa]	Poisson ratio	CTE [K^{-1}]
Silicon	170	0.28	0
Multilayer compound	190	0.26	0
SiO_2	72	0.17	$5.5 \cdot 10^{-7}$

Geometrical modification using a stress layer

This approach [Nie+14a] is based on a generic MLL deposition without a strong radial gradient in layer thickness. The actual MLL is prepared in a way, that it stands freely on the substrate without any connection to the remaining multilayer stack. Subsequently, a stress layer is deposited onto the front side, leading to an elastic deformation of the lens, see Fig. 3.33. This yields a relative tilting of the zones along the height of the MLL according to the requirements of a wedged MLL. The final shape is controlled with the thickness and the type of the additional layer, which will be silicon dioxide in this study. An energy of 1 keV for sputtering Ar^+ ions is used that results in a relatively high compressive residual stress within the deposited SiO_2 layer of about -1.0 GPa. The resulting relative layer tilt is subsequently analyzed with the method that was presented in section 3.3 using the *ImageJ* plugin *MLL Tilt Evaluation*. It provides the necessary input to iteratively refine the fabrication.

A finite element analysis (FEA) using CalculiX [DW14] is conducted to find a suitable thickness of the stress layer and to understand unwanted elastic deformations. A simple model is used that consists of a block of silicon substrate, the multilayer compound, and a SiO_2 stress layer at the front side [Nie+14a]. For simplification, all materials are modeled with isotropic elastic properties, although single crystalline silicon has cubic anisotropy and the multilayer has transverse isotropy. The parameters are given in Table 3.5. The dimensions are set to values of actual lenses for an application at a photon energy of 20 keV having a width of $100\ \mu\text{m}$, a height of $54\ \mu\text{m}$, and a thickness of $16.8\ \mu\text{m}$. As boundary conditions, the displacement of all bottom nodes is fixed and a symmetry boundary condition is applied to the center plane of the lens. The effect of residual stress is simulated by a mismatch of thermal expansion during temperature change between the stress layer with a certain CTE, and both other materials whose CTE is set to zero. Subsequently, the temperature change is modified iteratively until the compressive stress inside the stress layer equals -1 GPa. Beside the desired curvature of the MLL along its height, there is also some bending along its width noticeable that can

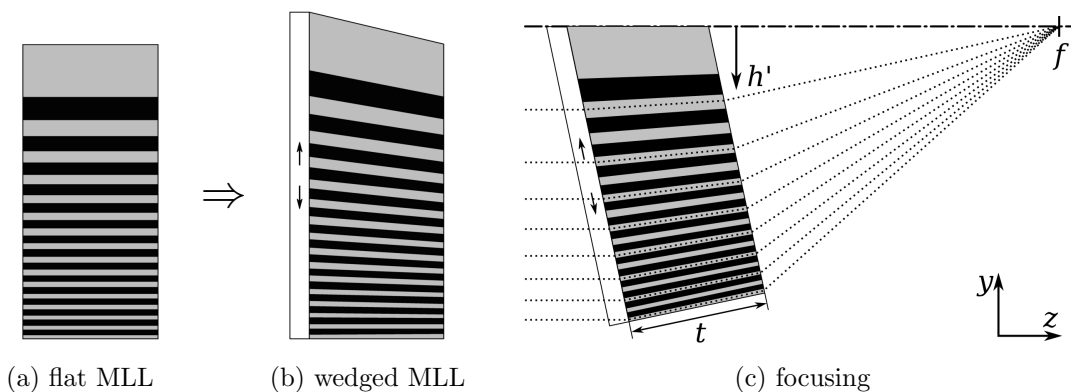


Figure 3.33.: Modification of a flat MLL to a wedged MLL by deposition of a compressively stressed layer on one side. X-rays run from left to right.

3. Multilayer Laue lenses

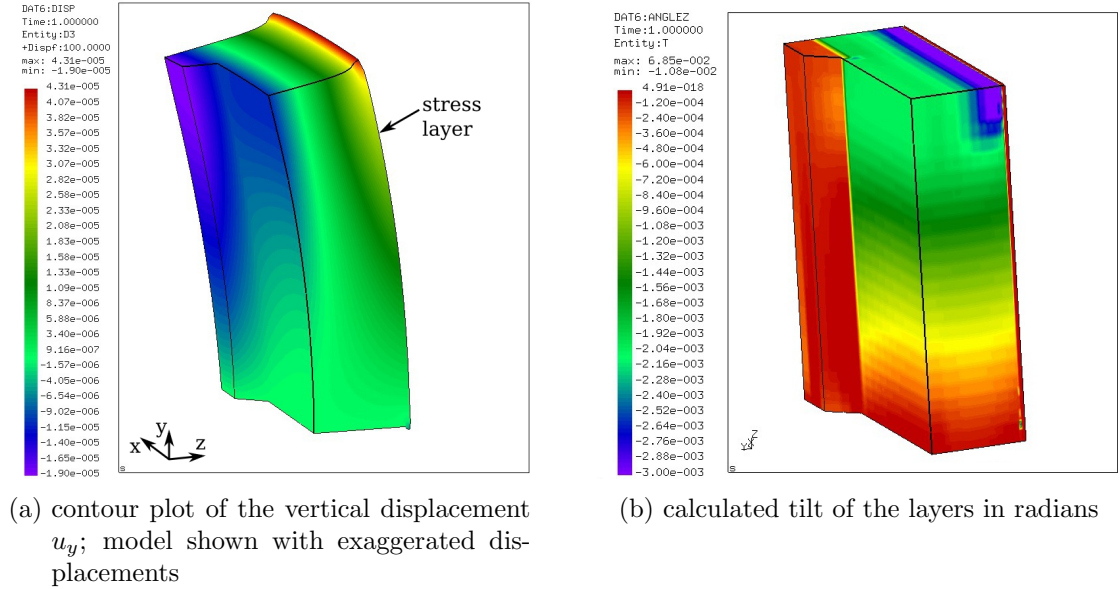


Figure 3.34.: Results of the FEA.

be expected due to the biaxial stress of the SiO_2 layer. Stiffening elements were added to the sides of the lens to reduce this effect. An example of such a FEA calculation is shown in Fig. 3.34a.

For X-ray application, two properties are of interest. First, the difference in vertical displacement Δu along the width of the aperture has to be small compared to the corresponding zone width. This information can be directly extracted from the FEA. Second, relative layer tilts are calculated from the output of the FEA according to the following algorithm that is implemented in a program. For each element, the corresponding nodes are ordered, and their positions and displacements are determined. Subsequently, two nodes with minimum and maximum position along the optical axis are identified. The tilt angle can be calculated from their vertical displacements and projected distance in beam direction. The calculated tilt angle is assigned to all nodes of the element and the result is added as an additional dataset to the output file of the FEA. Fig. 3.34b shows those results, indicating that a linear behavior can be expected. Finally, an initial set of properties for fabrication is found with few iterations.

Initial experiments

For basic demonstration purposes, two MLLs of deposition PS6056 (Table 3.1) with thicknesses t of $4.5\ \mu\text{m}$ and $10.5\ \mu\text{m}$ were selected. Both MLLs are placed in close adjacency on the same stripe and they have no stiffening elements. A nominally $200\ \text{nm}$ thick SiO_2 layer was deposited on their sidewalls to compare the effect of their different compliance (Fig. 3.35a). The XRM measurements to analyze the shape of the MLL are performed in the X-ray microscope *NanoXCT-100* using the $10\times$ FZP. Typically, tilt series are recorded with 0.02° step size at 101 positions. The radiographs are aligned

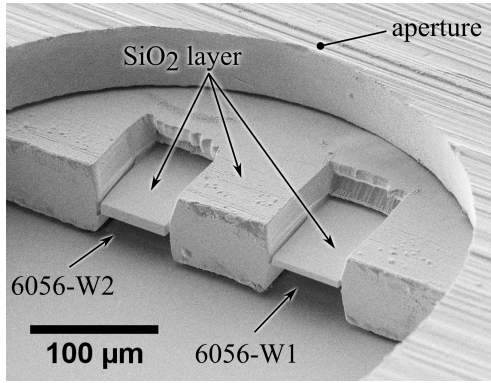
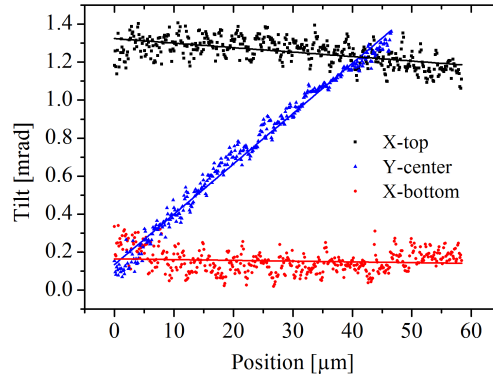
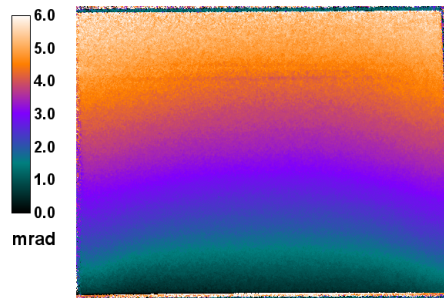
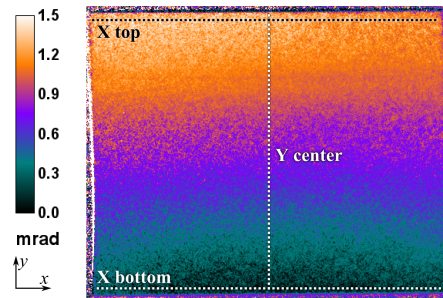
(a) SEM image after SiO_2 deposition(b) plots of $\Delta\theta$ along different lines(c) $\Delta\theta$ map of 6056-W1(d) $\Delta\theta$ map of 6056-W2

Figure 3.35.: Fabrication and characterization of 6056-W1 and 6056-W2. An aperture limits the region of the SiO_2 deposition on the sidewall of the wafer stripe.

using *ImageJ* and the *TurboReg* plugin [TRU98; The11].

Figs. 3.35c and 3.35d show the resulting maps of the 4.5 μm and 10.5 μm thick MLL. As expected, an increasing relative layer tilt along the height of the MLL is observed and some relaxation effects are visible as bent contours along the width of the MLL. The thinner lens shows a stronger tilt due to its larger compliance. Line plots of $\Delta\theta$ can be analyzed along the width and height of the MLL for a detailed evaluation. This analysis is shown for 6056-W2, see Fig. 3.35b. The positions of the line plots are indicated in Fig. 3.35d. An almost linear increase of the tilting angle along the height of the lens is observed. The slope is fitted by linear regression to $0.026 \text{ mrad}\cdot\mu\text{m}^{-1}$. An almost constant plateau in x-direction is recognized at the center of the lens.

Experiments at ID13, ESRF

The multilayer coating PS 6359 was chosen for first experiments using wedged MLLs at a synchrotron radiation facility. This decision has two major reasons: First, the a better optical performance is expected in comparison to PS 6056 due to the smaller theoretical size of the focus by design and the application of the empirical drift correction for the layer deposition. Second, the enhanced efficiency is related to dynamical diffraction and this effect is only observed at thin zones. Yan et al. calculated the local diffraction efficiency for an MLL with layer thicknesses down to 1 nm (Fig. 6a in [Yan+10]). The

3. Multilayer Laue lenses

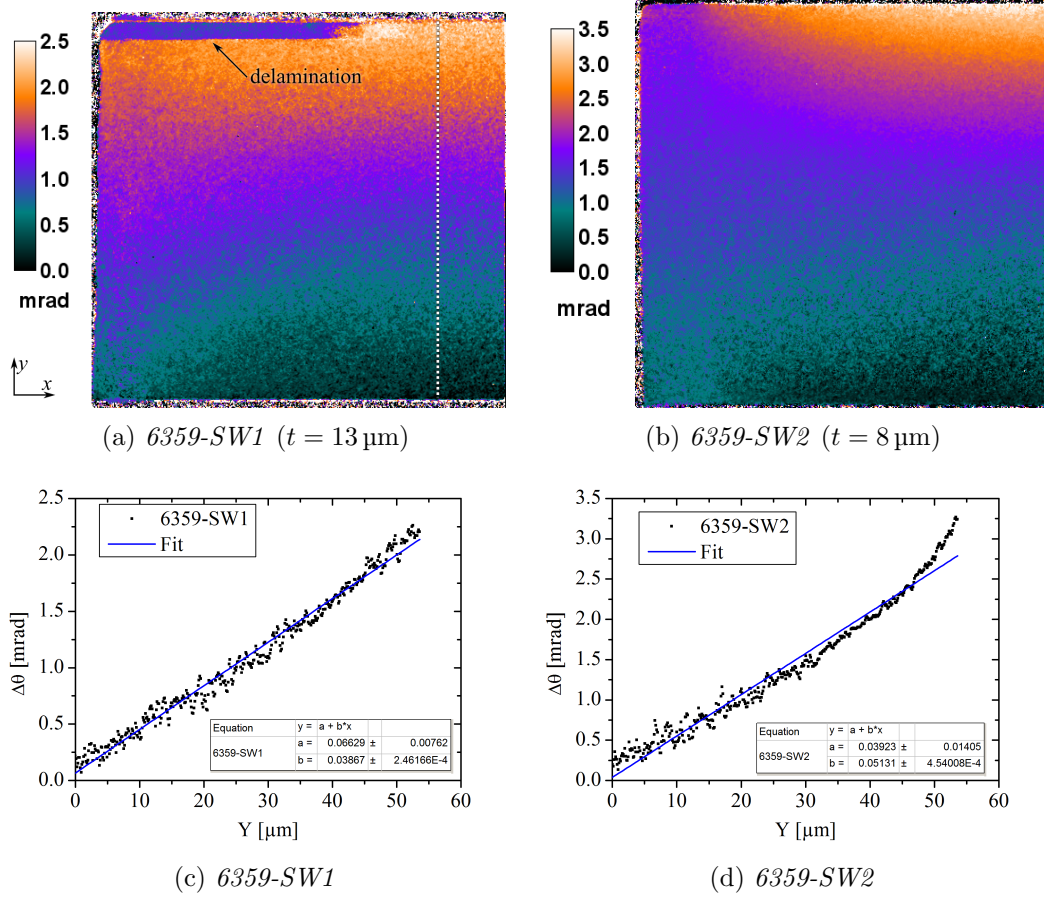


Figure 3.36.: $\Delta\theta$ maps and line plots along y at the center of the lens of two wedged MLLs *6359-SW1* and *6359-SW2*

thickness t of this MLL equals $16 \mu\text{m}$ according to eq. 2.15 for $E = 19.5 \text{ keV}$. The innermost, thick zones show the same efficiency of 13 % like a flat MLL exploiting relative phase shifts. Zones with thicknesses less than 20 nm show an increased efficiency of 70 %, because Bragg diffraction occurs. Thus, it is expected that PS 6359 having zone thicknesses of $19.5 \text{ nm} - 5.3 \text{ nm}$ is more suitable for this kind of experiments.

Experiments were done at *ID13, ESRF* at a photon energy of $E = 15.25 \text{ keV}$, which corresponds to a focal length of $f = 9.5 \text{ mm}$. Two wedged MLLs – *6359-SW1* and *6359-SW2* – with thicknesses of $t_1 = 13.0 \mu\text{m}$ and $t_2 = 8.0 \mu\text{m}$ for best dynamic diffraction and optimal phase shift, respectively, had been prepared (cf. Fig. 2.3). The corresponding nominal thicknesses of the SiO_2 layers are 400 nm and 160 nm to achieve a slope of the layer tilt of $s_\theta = 0.052 \text{ mrad} \cdot \mu\text{m}^{-1}$. The width of the MLL is $85 \mu\text{m}$ plus the width of both stiffening elements. Thus, some relaxation effects at the side will not affect the central region, i.e. the $54 \mu\text{m}$ wide part that will be finally used as aperture in case of a crossed lens. For the purpose of comparison, the $8.0 \mu\text{m}$ thick MLL *6359-SF3* without stress layer was prepared, i.e. it acts as a reference for the wedged MLL *6359-SW2*.

Fig. 3.36 summarizes the results of the evaluation of the relative layer tilt for both wedged lenses. *6359-SW1* owns a minor layer delamination at one side for the top-most

layers, which is not assumed to be critical. The line plots show a different behavior of both lenses: an almost linear slope of $\Delta\theta$ is observed in case of *6359-SW1*, whereas a progressive slope is observed for *6359-SW2*. The average slope determined by linear regression equals $s_{\theta,1} = 0.039 \text{ mrad}\cdot\mu\text{m}^{-1}$ and $s_{\theta,2} = 0.051 \text{ mrad}\cdot\mu\text{m}^{-1}$, respectively. Deviations along the width are assumed to be negligible within the central region of both lenses.

At first, experimental results of *6359-SW2* and *6359-SF3* will be discussed ($t = 8 \mu\text{m}$). Transmission images were acquired using the X-ray live camera. A scheme of the set-up at *ID13* is shown in Fig. 3.37a. Vertical slits truncate the illumination to about $80 \mu\text{m}$ and tilt series of the MLL were done, with α being the tilt angle. Diffraction to different orders is more or less efficient for each value of α . The corresponding defocus of the $\pm 1^{\text{st}}$ order is seen on the detector beside the 0^{th} order transmission image of the MLL. Each diffraction to any non-zero-order corresponds to a dark band, which is seen in the transmission image of the MLL. Hence, the width of this band gives a first indication, which parts of the MLL contribute to the present diffraction order.

In case of the flat MLL *6359-SF3*, almost no diffraction occurs at $\alpha = -0.240^\circ$ (Fig. 3.37b). The first-order defocus is pronounced at $\alpha = -0.176^\circ$ and $\alpha = -0.128^\circ$. The dark band moves towards thicker zones, which corresponds to a shift of the peak intensity in the defocus towards the optical axis. Almost no diffraction effects are seen at $\alpha = 0^\circ$. The first defocusing order is clearly visible at $\alpha = 0.160^\circ$. The width of the observed dark band is similar to the band, which was observed in case of the first-order. Less diffraction effects are seen at $\alpha = 0.288^\circ$.

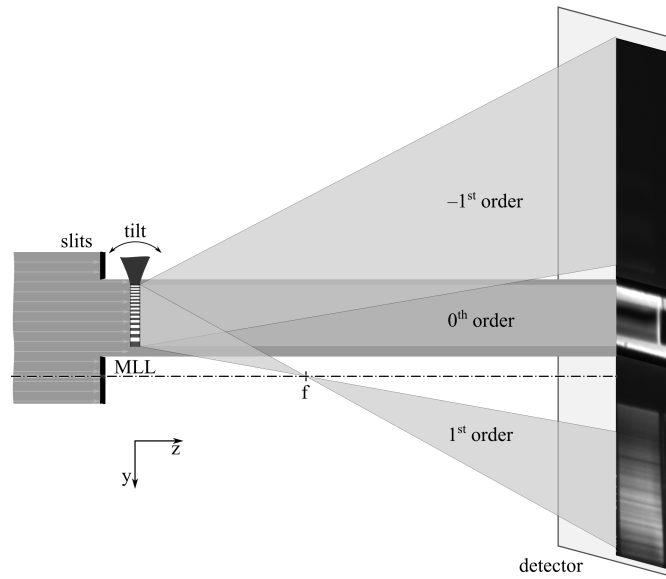
Two major differences are noticed, if the wedged MLL *6359-SW2* is used instead of the flat MLL. First, the defocus of the first-order focus is more intense and broader. This fact is in accordance with the broader dark band, which is observed in the transmission image. Hence, the diffraction efficiency of the thinnest and thickest zones is increased and almost all parts of the MLL contribute to the first-order focus. Line plots of the intensity are provided in Fig. 3.38 for both lenses. Second, the amount of layers that contribute to the first defocusing order is reduced. A narrower dark band is seen and the defocus is less pronounced. This behavior is expected, because the geometrical modification was realized to enhance the first focusing order.

The enhancement of the efficiency is estimated from the images of the X-ray live camera. Background subtraction of 400 cts was done to eliminate the offset caused by dark current of the CCD. Integral mean intensities of the first order focus of 2131 cts and 3346 cts are measured for the flat and wedged MLL, respectively⁹. This corresponds to a mean increase of the diffraction efficiency of 57%.

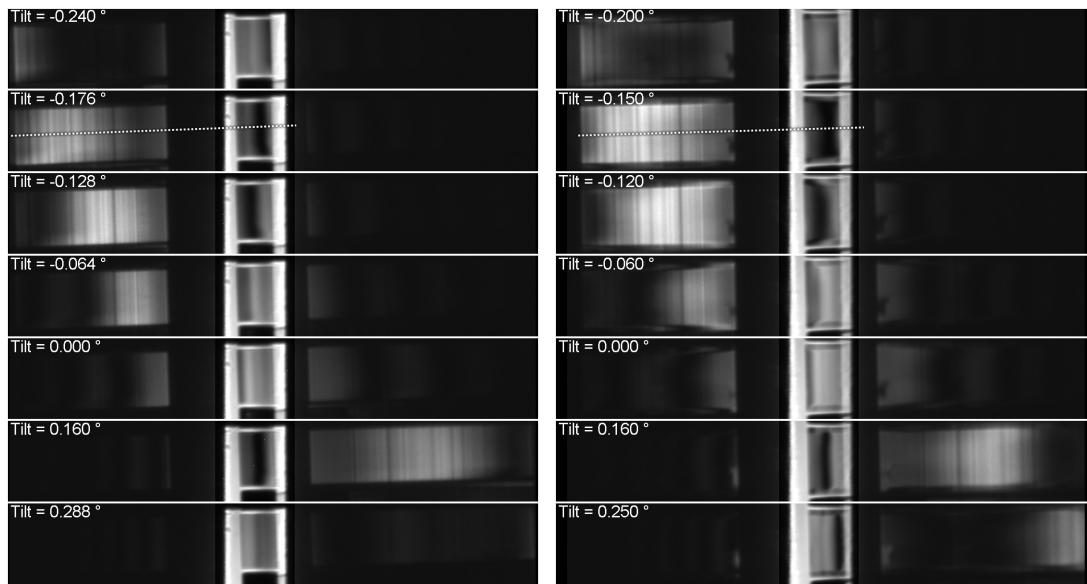
The results for *6359-SW2* – being optimized for phase shift – are promising due to the noticed enhancement of first-order diffraction. Though, the investigation of *6359-SW1* – being optimized for dynamic diffraction – shows less clear results. Fig. 3.37d

⁹Intensity values differ from Fig. 3.38 due to a scaling of the data to 8-bit prior to the preparation of the graph.

3. Multilayer Laue lenses

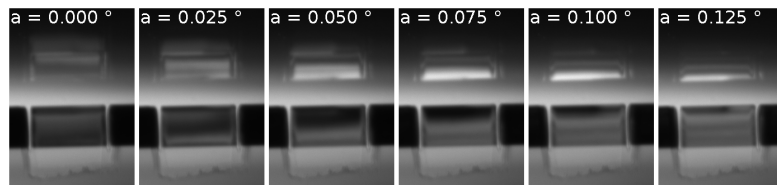


(a) Drawing of the beam path used for (b) and (c). No slits were used in case of (d). Detector positions are $z \simeq 5f$ and $z \simeq 1.5f$, respectively.



(b) *6359-SF3* (flat, $t = 8 \mu\text{m}$)

(c) *6359-SW2* (wedged, $t = 8 \mu\text{m}$)



(d) *6359-SW1* (wedged, $t = 13 \mu\text{m}$)

Figure 3.37.: Collections of images acquired with the X-ray live camera for three MLLs. The tilt angle is printed in each image. The intensity of the central region containing the zero-order image of the MLL in (b) and (c) is reduced to 17% to equalize gray levels.

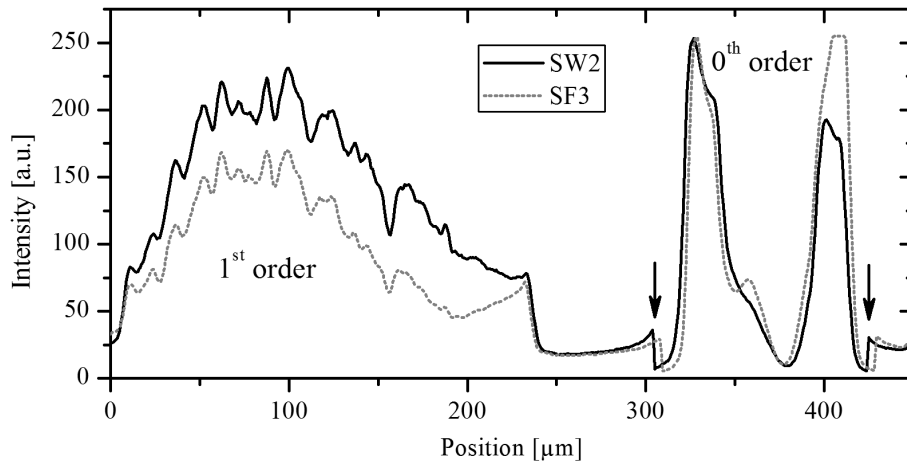


Figure 3.38.: Intensity plots of X-ray camera images of two MLLs *6359-SW2* and *6359-SF3*. Both MLLs are tilted to maximum 1st order diffraction. Positions are indicated in Figs. 3.37b and 3.37c as dashed lines. Averaging was done using a width of the profile of 30 px. Arrows mark the region where the intensity scaled to equalize gray levels.

contains images of the X-ray camera of a tilt series of this lens. Here, the detector was positioned more closely to the MLL and no slits had been used in contrast to the previous experiment. Thus, the defocus appears smaller and more close to the optical axis. The dark band broadens if the lens is tilted ($\alpha = 0.125^\circ \rightarrow 0.050^\circ$). However, no further extension of the dark band – i.e. diffractive region – towards thinner zones is observed at $\alpha = 0.025^\circ$. The intensity of the first-order diffraction decreases simultaneously. The reason for this behavior it is not yet evident. It is assumed to be caused by flaws of the multilayer and the subsequent fabrication of the wedged MLL.

Conclusions

According to these initial results, this approach seems to be feasible to manufacture wedged multilayer Laue lenses. Experiments using synchrotron radiation confirmed the increased efficiency of such a lens in comparison to a tilted MLL. The presented analysis to measure the relative layer tilt, which is based on the evaluation of tilt series of the MLL acquired with laboratory X-ray microscopy, is expected to be a robust approach to analyze the desired elastic deformation of the lens. An almost linear increase of the relative layer tilt is observed along the height of the MLL, which can be matched to a requested value if the thickness of the stress layer is changed. Some bending of the MLL is noticeable along its width, which is assumed to have negative impact on X-ray focusing properties. To reduce this effect below critical levels, optimal parameters for stiffening elements at the sides of the MLL may be found with FEA in future. In addition, the width of the MLL was enlarged to keep those boundary effects away from the finally used aperture of the lens element. Since the additional SiO₂ stress layer has a thickness

3. Multilayer Laue lenses

in the order of 300 nm, its absorption of 1 % at 5 keV and less than 0.02 % at 20 keV can be neglected.

Further work is necessary to study the elastical deformation of the MLL in detail with FEA. In particular, MLLs with a larger thickness might suffer from relaxation effects along the optical axis, i.e. different tilting of a zone might be observed at the front side and back side of the lens. The deposition of the SiO₂ layer needs to be optimized as well. A common recipe, which is typically used for the deposition on planar wafers, was applied for these initial experiments. Hence, some shadowing effects are expected to occur due to topography.

4. In-situ 3D investigations of crack propagation

In this chapter, a miniaturized set-up of the double cantilever beam test (DCB) is presented. A potential application of this method is estimated in the field of microelectronics to provide complementary information to conventional macroscopic tests. Thus, a brief introduction to this topic is provided in the following section. The *MicroDCB tester* and the preparation of specimens is described in sections 4.2 and 4.4. Finally, applications in microelectronics and other fields will be shown.

4.1. Challenges of the mechanical stability of recent microelectronics products

A cross section of a typical microprocessor chip is shown in Fig. 4.1. Billions of individual devices – transistors – are fabricated onto a single crystalline silicon wafer in a batch process. Thin films deposition and etching steps are used to add or remove material, respectively. The transistors are directly fabricated into the surface of the wafer. Wiring is subsequently realized with about a dozen of metallization layers (on-chip interconnects). The layers are numbered consecutively from bottom to top as “metal 1”, “metal 2”, . . .

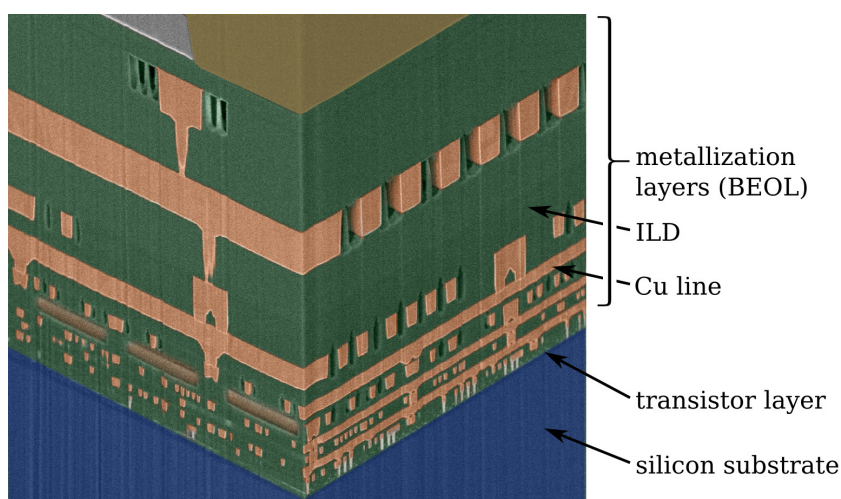


Figure 4.1.: SEM micrograph of a FIB-prepared cross section of a typical microprocessor chip. The colorized micrograph is taken from an IBM press room announcement on May 3, 2007: IBM Airgap Microprocessor [IBM07].

4. In-situ 3D investigations of crack propagation

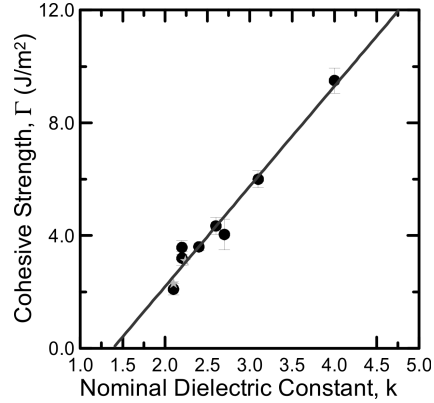


Figure 4.2.: A decrease of the relative permittivity of ILDs coincides with a steady decrease of mechanical properties such as cohesive strength. This graph is taken from M. Lane et al. [LLS04], Fig. 6.

or “M1”, “M2”, . . . , respectively. Currently, copper is used as conducting material for high performance products. Metal on-chip interconnects are separated by an insulator, the so-called interlayer dielectrics (ILD). Silicon dioxide was used for a long time for this purpose. Further shrinkage reduced the distance of adjacent copper lines to 100 nm and less. The thereby increased capacitance leads to increased signal delay times and to critical cross-talk of such lines.

One option to reduce the capacitance is the substitution of SiO_2 ($\kappa = 3.9$) with another dielectric material that is characterized by a lower relative permittivity κ . Those materials are referred¹ as *low-k* dielectrics ($\kappa \lesssim 3.9$) or *ultra low-k* dielectrics (ULK, $\kappa \lesssim 2.5$) [Gri+14]. The decrease can be achieved, if Si–O bonds are partially replaced by less polar bonds such as Si–C, C–C or C–H [Sha+04]. Organosilicate glasses fulfill these condition and they are currently used for interconnect insulation in leading-edge integrated circuits (IC). In addition, the generation of nanoscale pores within the material decreases its mean density to reduce κ even further.

A major drawback of this approach is the substantial decrease of mechanical properties such as Young’s modulus and fracture toughness of these dielectrics compared to SiO_2 , see Fig. 4.2 and [LLS04]. The weak mechanical properties challenge existing processes during fabrication – particularly CMP – as well as the reliability of final products. The latter fact is mainly caused by their cyclic operation due to switch-on/switch-off procedures or alternating loads during operation. In particular, temperature changes occur and thermal stress is generated due to a mismatch of the coefficients of thermal expansion of all used materials. This provides a driving force to initiate or to propagate layer delaminations, and it may yield a catastrophic failure of the device.

On the other hand, some counteractions are done to limit crack propagation. Massive copper structures at the border of each chip are a simple design option to stop micro-cracks that are generated during wafer dicing, when chips are separated by a sawing

¹The relative permittivity of SiO_2 marks the reference value; ‘ κ ’ is replaced with a ‘k’ for convenience.

process [San10]. The same concept can be applied to other regions of a chip. In particular, it is evident that the local layout of copper lines directly influences the chance of delaminations and appropriate *design rules* are applied to avoid critical spots. These assumptions can hardly be studied with macroscopic tests. Thus, the MicroDCB experiment was designed to provide valuable knowledge about crack evolution in on-chip interconnect stacks of integrated circuits.

4.2. Micro double cantilever beam test – MicroDCB

The DCB test was first presented by J. J. Benbow and F. C. Roesler in [BR57] in 1957. The title of this article was carefully chosen by the authors, being “Experiments on *Controlled Fractures*”. Unlike other methods like tensile or shear testing, this experimental set-up allows a crack to be introduced and to be propagated in a controlled way, i.e. stable crack propagation is realized and no instantaneous failure happens. A dedicated set-up of a four-point bending test yields similar results with a mixture of normal and shear loading at the crack tip [Cha+89]. Both methods are especially dedicated to measure adhesion properties of individual layers that are usually deposited onto a planar substrate. Hence, each specimen is prepared as a sandwich having the layers with weak interfaces in its center, where the crack will propagate. The substrate is bonded to a dummy with similar dimensions to obtain the sandwich [Dau+98].

The DCB test was chosen for this study for three major reasons. At first, the specimen can be placed on top of the testing device and no part of the fixture will shadow the region of interest during rotation. This is especially important if tomographies are acquired. Second, the specimen can be aligned in a way that the crack front is parallel to the optical axis. This will be the preferred set-up to obtain radiographs. Third, the method will initially be applied to test structures that are used in microprocessors. Although the four-point bending test is in general preferred due to time constraints, DCB is well introduced in semiconductor industry to measure basic adhesion properties of thin films [San14]. Recent studies investigated the effect of patterned films like the so-called BEOL stack, which realizes the internal wiring of a chip [San10]. The aim of this study is to develop a complementary method to visualize local crack propagation in these structures.

Double cantilever beam test

Fig. 4.3a shows the experimental set-up of a typical DCB test. The specimen consists of the previously described sandwich-type structure. Once a crack is initiated at its center, the system can be described with two individual beams, where the sample holder acts as a hinged support on one side with a given opening o . The other ends of both beams are fixed at the position of the crack tip. This system is well described with the Euler-Bernoulli beam theory [BR57; CH12], if all dimensions – the width t of the specimen, its height h , the deflection y at the end of each beam, and the length a of the crack – as

4. In-situ 3D investigations of crack propagation

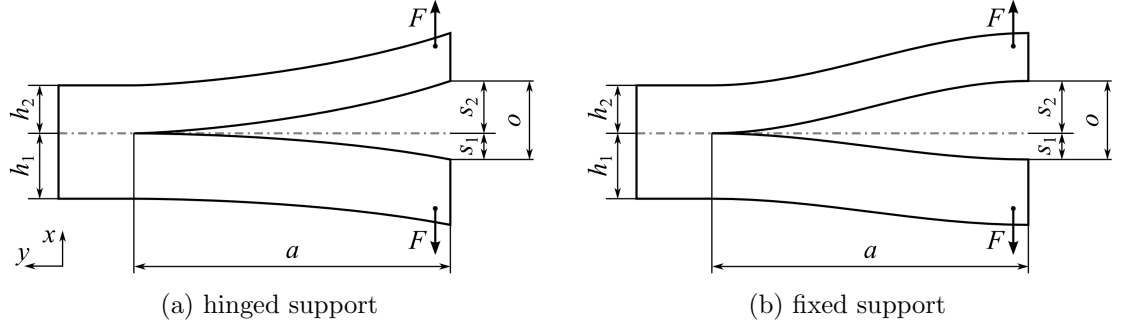


Figure 4.3.: Drawing to illustrate a DCB test with asymmetric beams.

well as Young's modulus E of the substrate are known, and $a \gg h$ is fulfilled. The force F equals

$$F(y) = 3EI \frac{y}{a^3} \quad , \quad (4.1)$$

and the second moment of area I of the rectangular cross section is

$$I = \frac{th^3}{12} \quad . \quad (4.2)$$

The energy release rate G is the normalized amount of elastic energy U_{el} stored in the system that would be released if the crack propagates. If only one beam is considered, it is

$$G^* = -\frac{1}{t} \frac{dU_{el}}{da} \quad , \quad U_{el} = \int_0^s F(y) dy \quad . \quad (4.3)$$

$$G^* = \frac{3Eh^3s^2}{8a^4} \quad (4.4)$$

Timoshenko's beam theory can be included in this concept to consider the fraction of energy caused by shear stress [WBH82]. This is of particular relevance for short crack lengths.

In the following, all necessary equations will be derived for the asymmetric case, i.e. both beams have different heights h_1 and h_2 with the known ratio ξ . This results in different deflections of each beam s_1 and s_2 , which sum up to the total opening o :

$$o = s_1 + s_2 \quad , \quad \xi = \frac{h_1}{h_2} \quad . \quad (4.5)$$

The deflections can be calculated for equilibrium of forces, thus

$$s_1 = \frac{o}{\xi^3 + 1} \quad , \quad s_2 = \frac{\xi^3 o}{\xi^3 + 1} \quad . \quad (4.6)$$

Finally, G can be calculated:

$$G = G_1^* + G_2^* = \frac{3Eh_1^3o^2}{8(\xi^3 + 1)a^4} \quad . \quad (4.7)$$

If stable crack growth occurs and plastic deformation at the crack tip can be neglected, the released energy is used to create new surface area at both sides of the crack, i.e. this *critical* value G_c can be related to the specific surface energy γ_0 :

$$G_c = 2\gamma_0 \quad . \quad (4.8)$$

The system is more stiff in case of a fixed support at the sample mount (Fig. 4.3b). This behavior was observed in some experiments. Both beams can be virtually divided at their middle position $a/2$. The reaction force at this point is still $F(y)$, but both dimensions in eq. 4.1 change ($a \rightarrow a/2$ and $y \rightarrow y/2$), thus

$$F_{\text{fixed}}(y) = 3 \cdot 4EI \frac{y}{a^3} \quad . \quad (4.9)$$

Hence, forces are four times larger compared to the other case. G is affected by the same factor due to the linearity of all subsequent equations:

$$G_{\text{fixed}} = \frac{3Eh_1^3o^2}{2(\xi^3 + 1)a^4} \quad . \quad (4.10)$$

As shown in eq. 4.7, the energy release rate decreases with a^{-4} , if a crack propagates and the opening o is kept constant. This is the major reason why this kind of experiment is suitable to perform controlled fracture in displacement controlled testing systems.

Differentiation from macroscopic tests

Macroscopic test systems – such as the *DTS Delaminator* [Dau05] – consist of a stiff frame, an actuator, and appropriate sensors to measure the applied force and the displacement. A procedure to prepare a specimen out of a semiconductor device will now be briefly described [San10]. A processed silicon wafer with some layers of interest on its surface and a corresponding dummy wafer are cleaved to pieces of approximately $50 \times 50 \text{ mm}^2$. A release layer is deposited on that side of the piece, which will be directly underneath the sample mount later on. A thin foil of polytetrafluoroethylene $(\text{C}_2\text{F}_4)_n$, or a thin film of either carbon or gold being deposited by sputter deposition can be used for this purpose. Both pieces are subsequently bonded with epoxy and cut to 3.5 mm broad bars using a dicing saw. Sample mounts are fixed with commercial super glue at the upper and lower side on one end of each bar. Finally, the sample mounts are placed into the testing station and the DCB test can be started.

A typical size of a specimen is $1.6 \times 3.5 \times 50 \text{ mm}^3$ and the overall dimensions of the testing station are $75 \times 170 \times 435 \text{ mm}^3$ (Fig. 4.4). It is evident that this kind of set-up is not applicable to microscopic in-situ studies. The testing station is too large to be integrated into an X-ray microscope. Also, this specimen cannot be penetrated by X-

4. In-situ 3D investigations of crack propagation

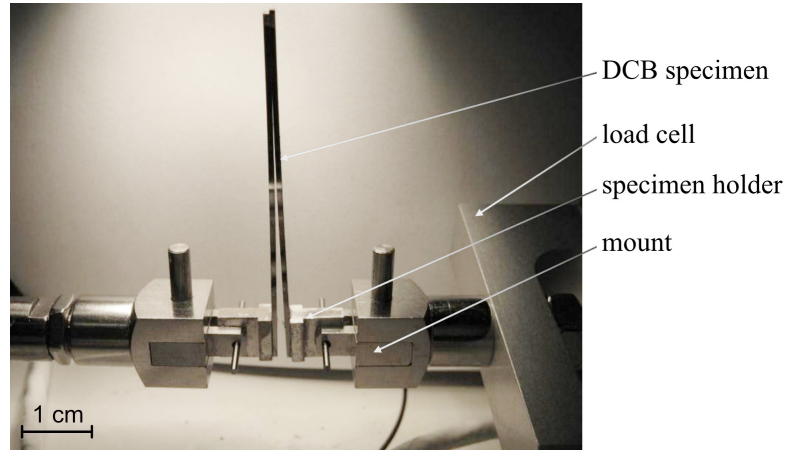


Figure 4.4.: *DTS Delaminator* with DCB specimen (based on Fig. 2.9 in [San10]).

rays at a photon energy of 8.0 keV, and it is anyway too large for tomographic studies at such high resolution, because the volume of the specimen would be much larger than the investigated volume.

Therefore, the size of the specimen was adapted to the field of view of the X-ray microscope *NanoXCT-100* (*Xradia Inc.*, Pleasanton, CA, USA). The cross section of each bar is approximately $50 \times 50 \mu\text{m}^2$ and its length is less than 2 mm – yielding a decent X-ray transmission and suitable handling during preparation.

Hence, the ratio of the thicknesses of both silicon beams – substrate and dummy – to both other layers – BEOL stack and epoxy with a total thickness of few microns – is significantly reduced compared to the macroscopic test. This is not expected to be an issue unless the experiment might be evaluated quantitatively to precisely determine particularly G_c , because the elastic properties of the films cannot be easily neglected like in macroscopic tests. This is in accordance with the aim of the miniaturized set-up to visualize crack propagation under load with X-ray microscopy. No force sensor has been integrated into this experiment, since loads can be estimated based on the geometry of the specimen and the measured deformations.

4.3. Experimental integration of the MicroDCB tester into an X-ray microscope

At first, major requirements and boundary conditions of the experimental set-up will be listed:

- The fixture must fit onto a base plate with a *kinematic mount* as used for sample holders in case of the X-ray microscope *NanoXCT-100*.
- No collision with existing parts of the X-ray microscope.

4.3. Experimental integration of the *MicroDCB* tester into an X-ray microscope

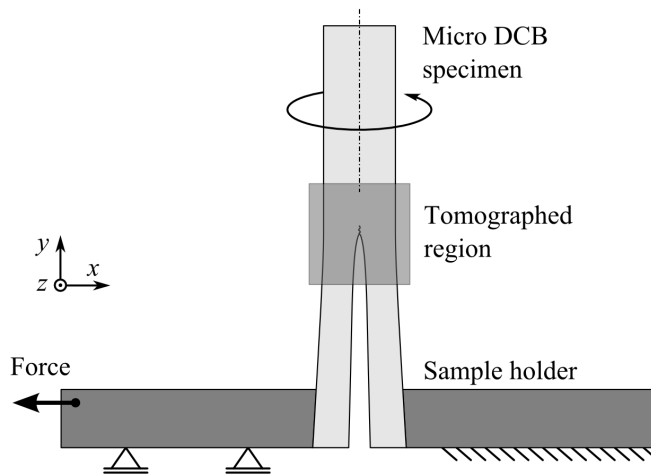


Figure 4.5.: Drawing of the *MicroDCB* test.

- The ability to acquire radiographs during full rotation of the specimen without restrictions; in particular no shadowing.
- A rigid design of the fixture to minimize elastically stored energy.
- Acceptable efforts to replace the specimen.
- A stable actuation for experiments that last several hours or days with a total displacement of at least $30\ \mu\text{m}$.
- No additional demands regarding radiation safety.

A dedicated device, which will be called *MicroDCB tester*, was developed and built in this thesis based on these considerations. Fig. 4.5 shows a scheme of the vicinity of the specimen, which is located on top of the entire fixture. Hence, the entire specimen can be imaged at arbitrary rotation without shadowing, except for its bottom part that will be bonded to the sample holder. The *MicroDCB tester* is displacement controlled, i.e. one side of the sample holder is fixed and the other side can move horizontally to an arbitrary position within the travel of approximately $35\ \mu\text{m}$.

The fixture itself is designed as a monolithic device with a flexure that will be employed to realize the translation. Fig. 4.6 shows images of the corresponding 3D CAD model. A technical drawing is given in appendix C, p. 122. The fixture has a horizontal drill hole housing a piezo actuator. The drill hole is then closed with a small piston and a nut with a fine adjustment screw. The piston reduces the torque that will be transferred onto the actuator if the screw is rotated. It acts as a well defined contact surface for the piezo actuator, which is clamped in between both parts of the flexure. This combination allows a coarse and a fine adjustment of the distance of both sample holders with the screw and the piezo actuator, respectively. Due to the leverage, the translation of the actuator yields a 2.57 times larger displacement at the position of the specimen; see Table 4.1 for a basic calibration.

4. In-situ 3D investigations of crack propagation

Table 4.1.: Measured displacement of the sample holder in dependence of the position of the piezo actuator.

Piezo position [μm]	2.0	4.0	6.0	8.0	10.0	12.0	14.0
Sample displacement [μm]	0.0	5.2	10.3	15.5	20.5	25.6	30.8

The *MicroDCB tester* can be used in different versions of Xradia's X-ray microscopes. The configuration of the motorized sample stages of the *NanoXCT-100* is not designed to center a specimen onto the rotational axis. Therefore, a small cross table *MS-125-XY* (*Newport Corporation*, Irvine, CA, USA) is mounted underneath the fixture onto a bare sample holder of the X-ray microscope. This set-up allows a manual centering of the specimen once it is mounted to the *MicroDCB tester*. The succeeding model *UltraXRM-L200* has a modified stage arrangement, which already supports this feature. A socket is used in this case to mount the fixture onto the sample holder. The final assembly is shown in Fig. 4.7.

The specimen has eventually to be mounted to the *MicroDCB tester*. The actual sample holder is realized with two small steel plates that are bonded on top of the fixture with super glue (Fig. 4.6b). Hence, they can be easily replaced, for instance if they are damaged or worn. The plates have a trapezoidal shape and a thickness of $100\ \mu\text{m}$. They are cut from sheet steel with a dicing saw. A technical drawing of an individual holder and a pattern to efficiently fabricate multiple holders is given in appendix C, pp. 123 and 124.

A *P-882.51* (*Physik Instrumente GmbH & Co. KG*, Karlsruhe, Germany) was chosen as piezo actuator. Its nominal displacement is $15\ \mu\text{m}$. It is equipped with ball tips and strain gauges that are calibrated for displacement measurements with the controller *E-709* of the same supplier. The actuator can be operated in open-loop and closed-loop mode, i.e. either a constant voltage or displacement is set. Closed-loop operation is needed to compensate for creep, which will otherwise have negative impact on experi-

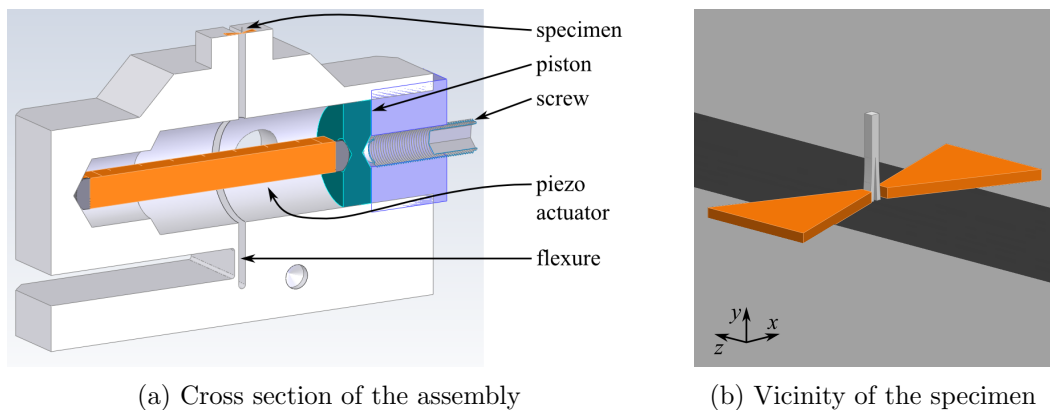


Figure 4.6.: CAD drawings.

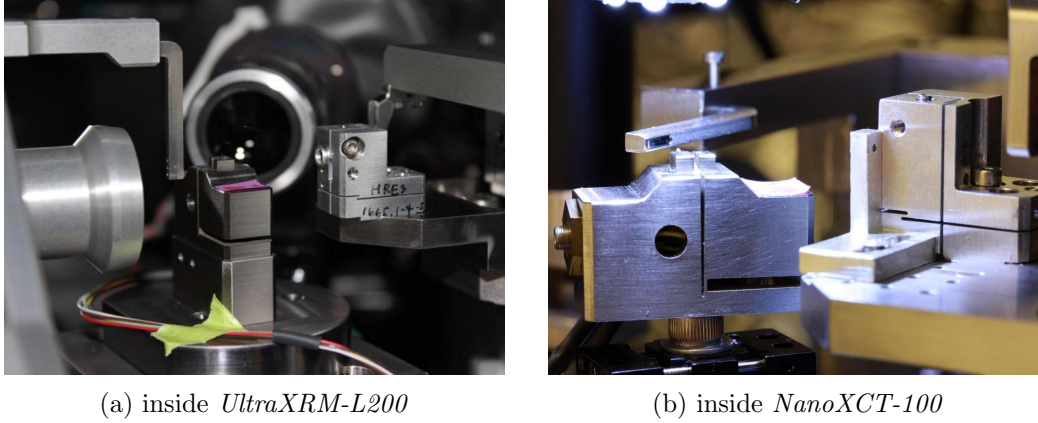


Figure 4.7.: Photographs of the *MicroDCB* tester inside two X-ray microscopes.

ments. An extension cable with a length of 3 m is used to connect the controller and the actuator. It can be routed through the existing cable feedthrough of the X-ray microscope. The controller is located outside the X-ray shielding. It is connected via USB to a computer; a virtual serial port is automatically created for communication. A basic introduction to the communications protocol is provided in appendix B, p. 119.

4.4. Specimen selection and preparation

Some basic remarks about the dimensions of the specimen have already been discussed at the end of section 4.2. The cross section of each specimen will be approximately $50 \times 50 \mu\text{m}^2$. This is a reasonable size to image the entire object with the $10\times$ FZP. A region of interest CT using the $40\times$ FZP is possible as well. In this section, some further aspects about suitable samples will be given. The preparation of MicroDCB specimens is described for the example of a microprocessor chip.

A general pre-condition of the imaging experiment is given by the fact, that the specimen has to be sufficiently transparent to X-rays at 8.05 keV. Table 4.2 lists attenuation

Table 4.2.: Attenuation lengths l_{att} and index of refraction $n = 1 - \delta - i\beta$ at 8.05 keV of several materials [Gul10c; Gul10b].

Material	ρ [$g \cdot \text{cm}^{-3}$]	l_{att} [μm]	$\tilde{\mu}$ [cm^{-1}]	δ	β
Air	$1.18 \cdot 10^{-3}$	$1.06 \cdot 10^6$	$9.43 \cdot 10^{-3}$	$3.81 \cdot 10^{-9}$	$1.15 \cdot 10^{-11}$
Epoxy	1.5	1287	7.77	$5.16 \cdot 10^{-6}$	$9.52 \cdot 10^{-9}$
Low-k ILD	1.14	309	32	$3.68 \cdot 10^{-6}$	$3.96 \cdot 10^{-8}$
Silicon	2.33	70.8	141	$7.58 \cdot 10^{-6}$	$1.73 \cdot 10^{-7}$
Copper	8.96	22.3	448	$2.44 \cdot 10^{-5}$	$5.50 \cdot 10^{-7}$
Gold	19.3	2.53	3950	$4.72 \cdot 10^{-5}$	$4.86 \cdot 10^{-6}$

4. In-situ 3D investigations of crack propagation

lengths for some materials² [Gul10c; Gul10b; HGD93]. The attenuation length for silicon (71 μm) is in the order of the size of the specimen. Due to the fact that silicon will be the major phase in each sample, an average attenuation of approximately $1/e$ can be expected. Copper has a significantly smaller value (22 μm), but even few tens of microns of Cu will not block the radiation – i.e. transmissivity is less than 15 %. Hence, a decent imaging with a good contrast of Cu and Si can be expected. Materials with light elements such as polymers are hardly imaged in absorption contrast due to their low attenuation. However, δ values are in a more reasonable range, yielding an increased visibility in Zernike phase contrast.

Mechanical preparation

The preparation of appropriate specimens for MicroDCB experiments is based on the procedure to get samples for a conventional DCB test [San10]. This mechanical preparation uses conventional techniques such as grinding and sawing to obtain dozens of individual samples. The procedure to finally mount a single specimen to the *MicroDCB tester* is described in the next subsection. There are three major differences to obtain such miniaturized specimens compared to the preparation of the macroscopic test: First, it is not sufficient to cut the wafer to desired dimensions. In addition, its thickness has to be reduced as well. Second, the cross section of each specimen is now quadratic instead of rectangular. This geometry is beneficial to acquire a tomography. Third, no release layer is used in this study. This decision is based on the consideration, that it will be demanding to reference and locate its position during all steps of the preparation. In addition, initial experiments revealed proper crack initiation making it obsolete to use any release layer.

The test wafer and a corresponding dummy wafer³ are cleaved to pieces of about $6 \times 6 \text{ mm}^2$, respectively. They are subsequently cleaned to remove all particles that originate from the cleaving step. The top surfaces of both pieces are bonded with epoxy and clamped with a suitable clip. Here, *EpoTek 375* (*Epoxy Technology Inc.*, Billerica, MA, USA) is used as adhesive. Curing is done on a heating plate at approximately 120 °C for several hours. Excessive adhesive is removed with a razor blade. The overall thickness of this assembly equals two times the thickness of a raw wafer (780 μm) plus the thickness of the epoxy layer and the thickness of the BEOL stack (few microns). It is temporarily fixed with a mounting adhesive⁴ onto a fixture that allows coplanar grinding. Grinding is done manually and it is controlled with a dial indicator until approximately 755 μm of the silicon are removed. Final grinding is performed with *P4000* silicon carbide paper to ensure a smooth surface.

²Epoxy is approximated with $\text{C}_{18}\text{H}_{20}\text{O}_3$, being the major component of a bisphenol A epoxy resin.

Air is approximated as $\text{N}_{79}\text{O}_{21}$. Low-k ILD is exemplary taken from [Lee+08], SiCOH in Table 1 ($\text{Si}_{24}\text{C}_{57}\text{O}_{19}$, $\rho = 1.14 \text{ g} \cdot \text{cm}^{-3}$).

³E.g. a raw silicon wafer.

⁴E.g. *CrystalBond 590* (*Ted Pella Inc.*, Redding, CA, USA).

4.4. Specimen selection and preparation

Table 4.3.: Used parameters of the precision saw to prepare MicroDCB specimens and of the low pressure plasma system to clean their surfaces.

Disco DAD 321		Diener Femto version C	
Parameter	Typical value	Parameter	Typical value
Blade type	Z09-SD2000-Y1-60	Type of gas	100 % O ₂
Spindle rev.	30000 min ⁻¹	Pressure	0.5 mbar
Mode	semi-automated	Generator power	80 %
Cut mode	A	Plasma process time	5.0 min
Cut shape	square	Matching C-Load	36 %
Cut depth	80 μm	Matching C-Tune	36 %
Y Index CH1	1.05 mm		
Y Index CH2	0.10 mm		
Feed rate	0.6 mm·s ⁻¹		
Water flow	0.5 l·min ⁻¹		

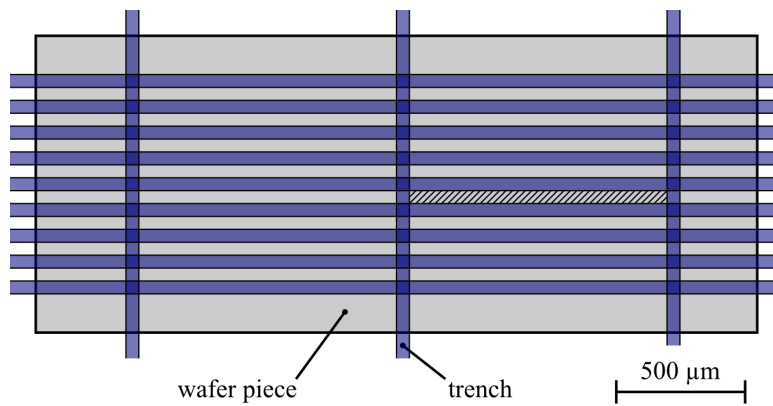


Figure 4.8.: Dicing pattern to prepare numerous specimens at once. A single MicroDCB specimen is indicated by the hatched area.

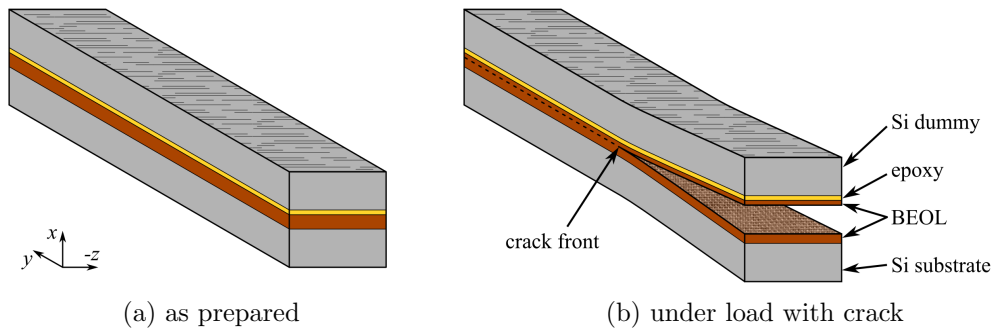


Figure 4.9.: Drawing of a sandwich-like MicroDCB specimen. Outer dimensions are $50 \times 50 \times 1000 \mu\text{m}^3$.

4. In-situ 3D investigations of crack propagation

The assembly is released after the first grinding step and temporarily mounted onto a suitable flat holder – e.g. a larger wafer piece – that can be inserted into the dicing saw. Here, a *DAD 321* (*DISCO corporation*, Tokyo, Japan) is used. The parameters are listed in Table 4.3. The blade height is set in such a way, that the depth of the cut is approximately 80 μm , i.e. a shallow trench is generated. Semi-automated sawing can be used to accelerate the preparation. At first, few trenches with a distance of 1.05 mm are cut in one direction. The stage is afterwards rotated by 90° and trenches are cut with a distance of 0.10 mm. Hence, rectangular areas with a dimension of $0.05 \times 1.0 \text{ mm}^2$ are separated, considering the width of the cut of approximately 0.05 mm. The resulting pattern is drawn in Fig. 4.8. The piece is subsequently transferred upside down onto the grinding fixture. It has to be ensured that all trenches are well filled with mounting adhesive. Its backside is ground, until the thickness is reduced to approximately 50 μm and all trenches are visible. Individual specimens are eventually separated by dissolving the adhesive with acetone. The result of the mechanical preparation can be inspected with visible light microscopy. An apparently flawless specimen is selected for the *MicroDCB* experiment.

An illustration of such a specimen is given in Fig. 4.9. The sandwich-type structure of the specimen after preparation is clearly visible in Fig. 4.9a. It consists of the original test wafer (Si substrate, BEOL), a thin layer of epoxy, and the silicon dummy. The crack is expected to propagate within the BEOL stack during the experiment, where the weakest interfaces and layers are located (Fig. 4.9b).

Preparation of a *MicroDCB* experiment

The specimen has to be carefully cleaned before it is bonded to the *MicroDCB tester*. Initial experiments indicated, that the crack may form spontaneously under load. However, this behavior was not observed in consecutive experiments with an improved type of samples (cf. section 4.5). Thus, few methods were evaluated to prepare an initial crack.

At first, residuals of the mounting adhesive are dissolved with boiling acetone. It is known that adsorbed acetone molecules on the surface of the specimen have a negative impact onto bonding with most adhesives such as super glue [Bur13]. It is also evident that further cleaning will not be productive, if the specimen is placed onto another – potentially dirty – surface in the meantime. Hence, one end of the specimen is now fixed into reverse-action tweezers to prevent such a step during further handling of the sample. It is subsequently cleaned with isopropyl alcohol and oxygen plasma (see Table 4.3).

The specimen is eventually mounted to the *MicroDCB tester* using the pre-alignment

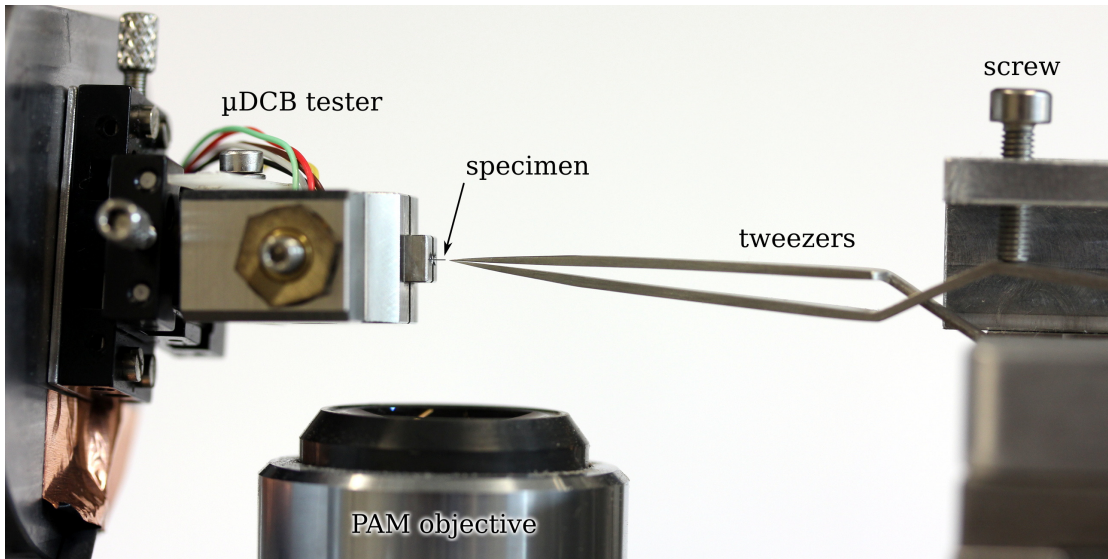


Figure 4.10.: Photograph showing the PAM with the *MicroDCB tester* and reverse-action tweezers, both being attached to a separate XYZ stage, to mount a specimen. The tweezers can be opened with a screw in order to release the specimen.

microscope (PAM)⁵. The PAM is equipped with an additional fixture that is able to hold and carefully open the reverse-action tweezers, see Fig. 4.10. The sample holder with the *MicroDCB tester* is placed onto the *kinematic mount* of the PAM and the distance of both steel trapezoids of the *MicroDCB tester* is increased to approximately 200 μm using the fine thread screw. The tweezers are opened until the specimen is loosely fixed and a small portion of super glue is applied to the tips of both steel trapezoids. The free end of the specimen is now placed between both steel trapezoids, and the tester is closed using the fine thread screw until the specimen is properly clamped and the tweezers can be retracted. It is assumed that the glue is entirely cured after one hour. The *MicroDCB tester* can finally be installed into the X-ray microscope after this period.

Crack initiation can be supported in different ways. A dedicated release layer is used in conventional DCB experiments, but this approach is not expected to be easily applicable for the miniaturized test, see section 4.2. As a consequence of Griffith's criterion, cracks are preferentially generated at notches due to the increased stress at their base. Three methods have been evaluated in this thesis to fabricate a notch.

The first approach uses the capabilities of FIB to do micromachining in advance of the cleaning procedure. The *MicroDCB* specimen is clamped in an upright position onto a suitable sample holder and subsequently transferred into the SEM/FIB system.

⁵This special visible light microscope belongs to the *NanoXCT-100*. A first XYZ stage has a *kinematic mount* where any sample holder of the X-ray microscope can be placed and a region of interest of the specimen can be identified within the field of view of the optical microscope. Its coordinates can be used to locate this region in the X-ray microscope later on. A second XYZ stage being placed vis-à-vis is free to manipulate any accessory. In particular, it is used to put gold markers onto the specimen.

4. In-situ 3D investigations of crack propagation

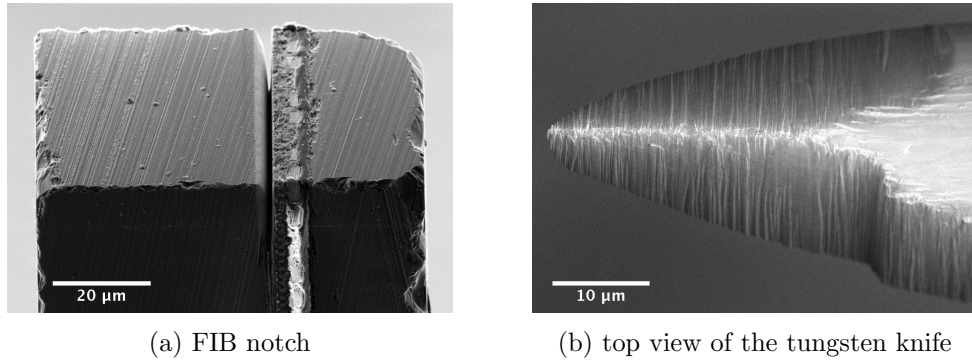


Figure 4.11.: Methods to notch a specimen.

The long axis of the specimen is aligned parallel to the ion beam, i.e. one end of the specimen faces the ion column. A common rectangular FIB milling box is used to etch the notch at an ion current of 6.5 nA. Fig. 4.11a shows an SEM micrograph of a specimen resulting of this procedure. This approach has a major drawback: The handling of the specimen gets more complex and time-consuming, because no sample holder is currently available, which is compatible with the SEM/FIB system and the PAM. Thus, there is an increased risk to accidentally damage the specimen after FIB milling.

The second approach utilizes a small knife to generate the notch inside the X-ray microscope. The end of a tapered tungsten wire ($\varnothing 200 \mu\text{m}$) is bent by 45° . A wedge having a width of approximately $30 \mu\text{m}$ and an angle of 40° is milled with FIB at its tip (Fig. 4.11b). The wire is mounted onto an additional motorized XYZ stage inside the X-ray microscope. The specimen is bonded to the *MicroDCB tester* as described above and aligned within the field of view of the X-ray microscope. The knife is subsequently moved underneath the end of the specimen. A notch is generated once the knife is eventually moved upwards until it penetrates the epoxy layer. The knife may stay at this position at the beginning of the *MicroDCB* experiment. Thus, an additional tensile load is applied onto the base of the notch.

In the third approach, a flawless razor blade is attached to the first XYZ stage of the PAM. The *MicroDCB* specimen is fixed with the reverse-action tweezers on the second XYZ stage (cf. Fig. 4.10). The edge of the razor blade is aligned parallel to the layers of the specimen. Once specimen and blade are located with the visible light microscope, the central part of the specimen containing the epoxy layer and the metallization layers is gently pushed against the blade until an initial crack is observed. The specimen is subsequently mounted to the *MicroDCB tester*.

4.5. Application to microelectronic products

This section summarizes experimental results and experiences regarding high-resolution investigations of recent microelectronics products with X-ray microscopy as well as investigations with the *MicroDCB tester*. Two sets of samples – type *A* and *B* – were

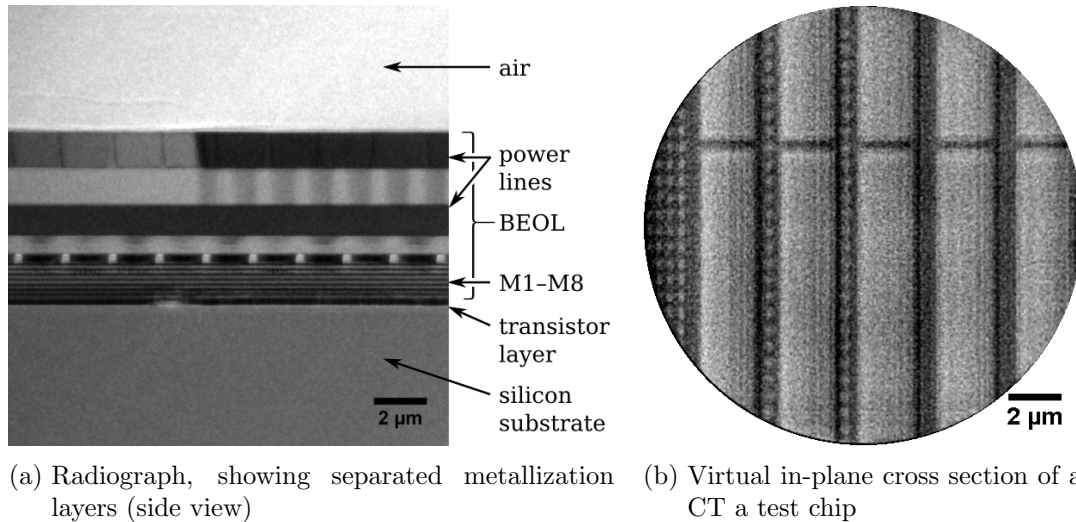


Figure 4.12.: High-resolution XRM investigations of microprocessors using the $40\times$ FZP.

prepared and tested. The corresponding results are discussed in this section. The choice of a suitable test wafer as well as the preparation itself was improved for type *B*.

High-resolution X-ray microscopy of microelectronics devices

The X-ray microscope *NanoXCT-100* is equipped with two Fresnel zone plates. The $10\times$ FZP has a field of view of $67 \times 67 \mu\text{m}^2$. The pixel size of the digital radiograph equals 65 nm. This lens is suitable to get an overview of the specimen. The $40\times$ FZP has a field of view of $16.5 \times 16.5 \mu\text{m}^2$ resulting in a pixel size of 16 nm. Since this lens provides best resolution, it is preferred for detailed investigations.

Fig. 4.12a displays a radiograph of a MicroDCB specimen. It shows a cross section of a microprocessor chip that was fabricated in 45 nm CMOS technology node. The normal of the original surface of the wafer is aligned perpendicularly with respect to the optical axis. The individual metallization layers are clearly resolved in the radiograph.

This example indicates, that, in principle, it should be possible to acquire acceptable tomographies of BEOL structures, i.e. individual copper lines will be resolved. However, it is known from experience, that the resolution of a tomographic reconstruction is worse than the resolution of its input data. This fact is evident, because all imperfections of the alignment of the microscope – e.g. regarding the orthogonality of all axes – and the post-processing of the data – e.g. alignment of all projections – represent sources of additional errors. Furthermore, the acquisition time of each projection of a tomography is usually reduced in comparison to single radiographs to keep the total acquisition time at moderate levels accepting a worse signal-to-noise ratio.

Few tomographic investigations of recent microelectronics devices (45 nm CMOS technology node) using the $40\times$ FZP were performed within the scope of the development of MLLs (chapter 3). A virtual cross section of the reconstructed volume is shown in Fig. 4.12b. In particular, it is noticed that the smallest features are not entirely resolved,

4. In-situ 3D investigations of crack propagation

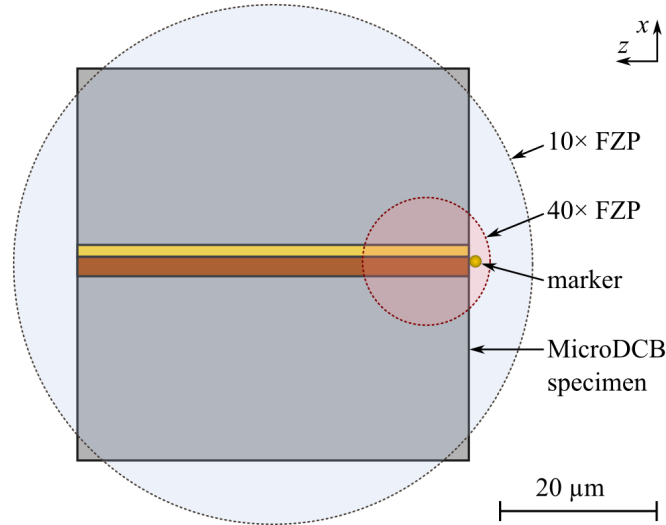


Figure 4.13.: Comparison of potentially reconstructed circular cross sections of a MicroDCB specimen at tomographies with the 10× and 40× FZP, true to scale. The high resolution tomography is limited to an area being close to the surface due to the necessity for a marker to align all projections.

but neighboring metallization layers can be differentiated. Thus, the performance of the microscope is sufficient to study crack propagation within such structures. It should be mentioned that this particular study used a different set-up of the X-ray microscope that is optimized for flat specimens [Krü+11]. The investigated chip was thinned to a thickness of approximately 60 μm. It is an inherent drawback of this kind of tomography for flat specimens, that only a subset of all necessary projections can be acquired. Thus, sampling in Fourier domain is incomplete (“missing cone”) and extended lateral features are insufficiently reconstructed. This approach causes additional artifacts, but it puts less demands on the preparation of the specimen.

MicroDCB specimens are prepared as bars with a quadratic cross section (section 4.4). This shape is generally preferred for tomographic investigations, because complete sampling is possible. However, the dimensions of the specimen are currently matched to the field of view of the 10× FZP. A tomography using the 40× FZP needs to be realized as *region of interest* tomography – i.e. it cannot be avoided that parts of the object, being located outside of the reconstructed volume, are visible within some projections. This is a well established approach. However, the contrast is typically reduced. The tomography has to be acquired close to a surface of the specimen in consequence of the need for a marker being visible in all projections. Fig. 4.13 illustrates this issue. A central area can be investigated, if no marker is needed. This may be achieved with advanced image processing [Bra06], e.g. using cross-correlation of subsequent projections or measured and calculated projections. Unfortunately, the layout of a chip shows a high degree of translational symmetry, which is why these methods are expected to fail. A more promising approach was recently shown. In this case, markerless alignment is

achieved with external monitoring of the movement of the sample holder [Wan+12].

Results with sample type A

A first set of MicroDCB specimens was prepared using a test wafer with structures manufactured in 45 nm CMOS technology node. The fabrication of this wafer was stopped before back-end processing, i.e. no solder bumps exist. Hence, the complete BEOL stack with all metallization layers is present and the surface is still flat. A cross section of this chip is shown in Fig. 4.12a.

Specimens were prepared as described in section 4.4 with two exceptions: First, *M-Bond 601* (*Ted Pella, Inc.*, Redding, CA, USA) was used as adhesive. Second, the specimen was thinned at both sides by grinding and lapping prior to sawing. Thus, batch processing of several specimens as shown in Fig. 4.8 was not possible⁶ and each bar was sawed individually.

Flawless specimens were finally selected and mounted to the *MicroDCB tester*. *Gorilla super glue* (*Gorilla Glue, Inc.*, Cincinnati, OH, USA) was used as adhesive. The curing time was at least one hour. The *MicroDCB tester* applies a certain compressive pre-load onto the specimen. An almost load-free state can be achieved, if the displacement of the piezo actuator is increased in 250 nm steps and radiographs are acquired simultaneously. The procedure is stopped, once some motion in subsequent radiographs is detected – i.e. the loose holder starts moving and a slight relaxation of the epoxy layer is seen. If required, this routine can easily be automated using advanced image processing methods in the future. A further increase of the displacement initiates and opens the crack. Bonding was renewed, if the crack initiation was not successful because one side of the specimen detached from the holder.

Fig. 4.14 shows a stitched radiograph of a specimen that was mounted to the tester. The specimen was well aligned with respect to the sample holder. A kind of meniscus is seen for the super glue, which is an indication for good wetting characteristics. The sample holder appears opaque because of the short attenuation length of iron at 8.0 keV. A crack was spontaneously initiated and subsequently driven while the displacement of the actuator was increased. A stitched radiograph of the same loaded specimen is shown in Fig. 4.15. A small part at the lower end of the left beam was ruptured during preparation without having consequences for the experiment.

Unfortunately, the crack runs along the interface between epoxy and the original surface of the test wafer (Fig. 4.15). Other experiments with specimens being equally prepared showed similar results – a crack was initiated in three of five attempts. In particular, no cracking was observed inside the BEOL stack. It is expected, that a major reason of this behavior is related to the so-called power lines at the top of the BEOL stack. Those lines are rather large in comparison to metal lines in layers M1 to

⁶Specimens are torn off if the second trench is sawed directly after the first cut. This can be avoided, if the mounting adhesive is heated meanwhile to fill the first cut with adhesive what results in a more stable mount of the bar.

4. In-situ 3D investigations of crack propagation

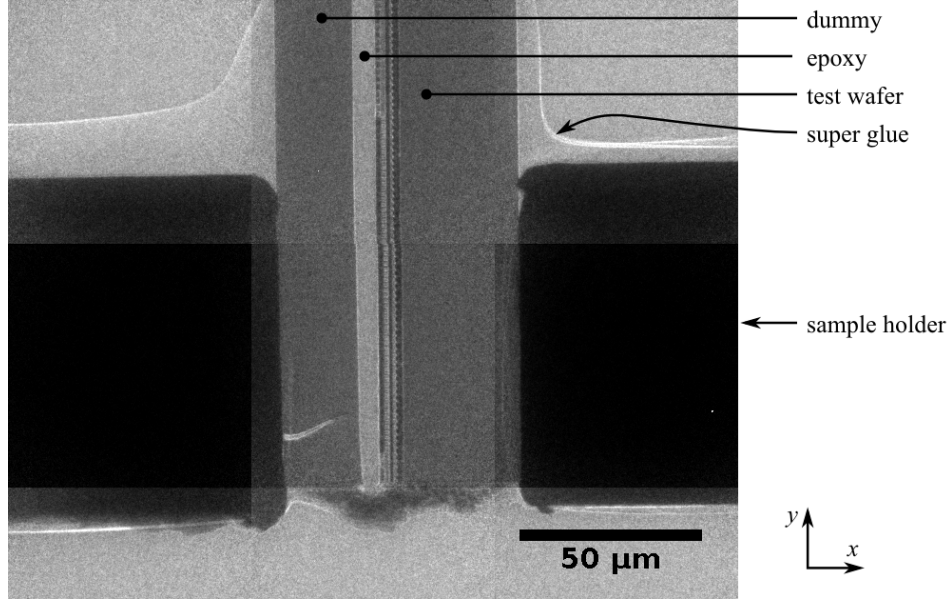


Figure 4.14.: Stitched image of nine radiographs, $10\times$ FZP, Zernike phase contrast. It shows a specimen inside the mount of the *MicroDCB tester*, cf. Fig. 4.5.

M8 underneath. Hence, they act as a crack stop. The chance that an existing crack changes its plane from the interface epoxy/wafer through the power lines to the region of interest is assumed to be negligible. This fact is critical, because the former interface seems to be preferred for spontaneous crack initiation.

Nevertheless, this experiment allows a first evaluation of the *MicroDCB tester*. It is possible to estimate some basic mechanical parameters, such as forces and energy release rates. In addition, the capability to run a tomography under load can be tested. Dimensions are measured in Fig. 4.15. A crack length a of $319\mu\text{m}$ is observed at an opening o of $26\mu\text{m}$. The epoxy layer will be neglected due to its large compliance. Both beams have different heights: $h_1 = 21.6\mu\text{m}$ and $h_2 = 37.7\mu\text{m}$. The width t of the specimen is approximately $60\mu\text{m}$. Young's modulus of silicon is approximated⁷ as $E = 130\text{ GPa}$ [HNK10]. The bonded area equals approximately $60 \times 80\mu\text{m}^2$.

Thus, the critical energy release rate for crack propagation G_c for the interface epoxy/wafer as well as the applied force F_{mount} and tensile stress σ_{mount} at the mount can be estimated using eqs. 4.7 and 4.1:

$$G_c = 27\text{ J} \cdot \text{m}^{-2} \quad (4.11)$$

$$F_{\text{mount}} = 13\text{ mN} \quad (4.12)$$

$$\sigma_{\text{mount}} = 2.8\text{ MPa} \quad (4.13)$$

The value of G_c is larger than typical values being measured for the BEOL stack, partic-

⁷Single crystalline silicon has anisotropic elastic properties with cubic symmetry. Using Young's modulus and assuming isotropic behavior is here done for convenience to get a rough estimate.

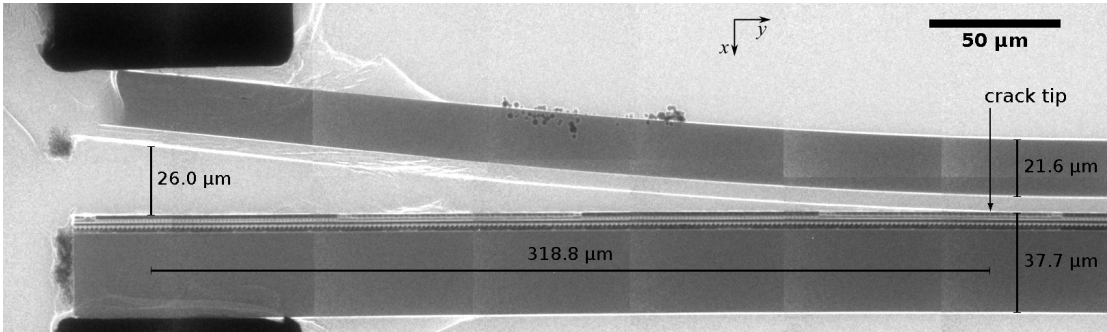


Figure 4.15.: Stitched radiograph of a MicroDCB specimen under load. The image is rotated clockwise by 90° in contrast to other figures.

ularly if low-k or ultra low-k materials are used (compare Fig. 4.2). Therefore, it can be expected, that a crack within the region of interest can be easily driven with this fixture. The value of tensile stress is moderate at this length of the crack. The tensile strength of a typical super glue – *Loctite 435* (*Henkel AG & Co. KGaA*, Düsseldorf, Germany) – is specified with 30 MPa on steel [Hen10]. However, a lower value has to be expected for this kind of micro-bonding, e.g. due to environmental effects and partial curing of this very small amount of glue during the mounting procedure.

A tomography of this specimen was acquired *in-situ*, i.e. the displacement of the actuator was hold at a certain position using closed-loop operation. The $10 \times$ FZP and Zernike phase contrast were used. 401 projections were acquired ranging from -90° to 90° à 30 s at binning 2. The overall acquisition time was approximately 3.5 h. Three projections of this series are shown in Fig. 4.16. The projections were aligned and reconstructed using *Bead Aligner* (see p. 21) and *XMReconstructor 9.0*, respectively. Appropriate virtual cross sections of the reconstructed volume are collected in Fig. 4.17. The images show no significant artifacts that indicate any disturbing motion of the specimen. Details are well restored with respect to the rather short acquisition time. In particular, few cracks are seen inside the epoxy layer (Figs. 4.17a and 4.17c). In summary, the experimental results show first evidence of the feasibility of the miniaturized double cantilever beam test.

Results with sample type B

The selection and preparation of suitable samples was slightly modified with regard to the experiences with samples of type A. At first, a different wafer was chosen for MicroDCB specimens. This test wafer was fabricated in 45 nm CMOS technology node. Processing stopped after four metallization layers. Thus, no large so-called power lines are existing, which might act as a barrier for crack propagation. Second, the same epoxy as used for macroscopic experiments was selected and dicing was automated using the pattern of Fig. 4.8 prior to the second grinding step. Third, the method to mount the specimen was improved. The initially used susceptible set-up with vacuum tweezers to manipulate the

4. In-situ 3D investigations of crack propagation

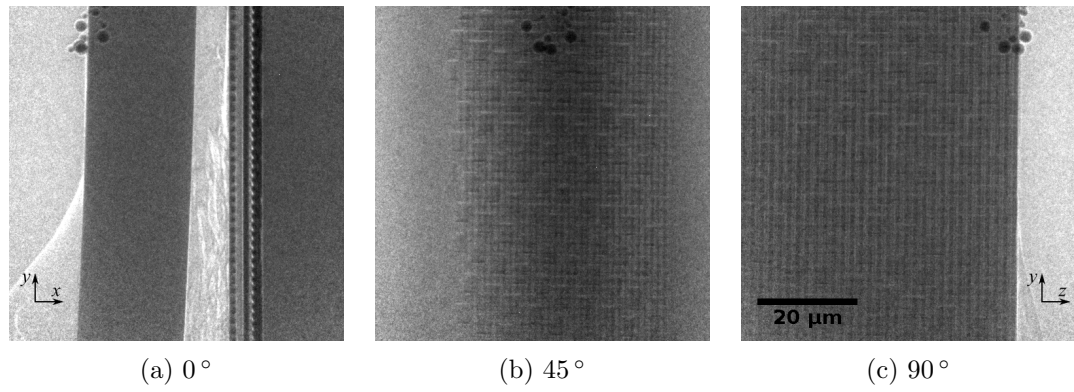


Figure 4.16.: Projections of the tomography at different angles. Zernike phase contrast, 10× FZP.

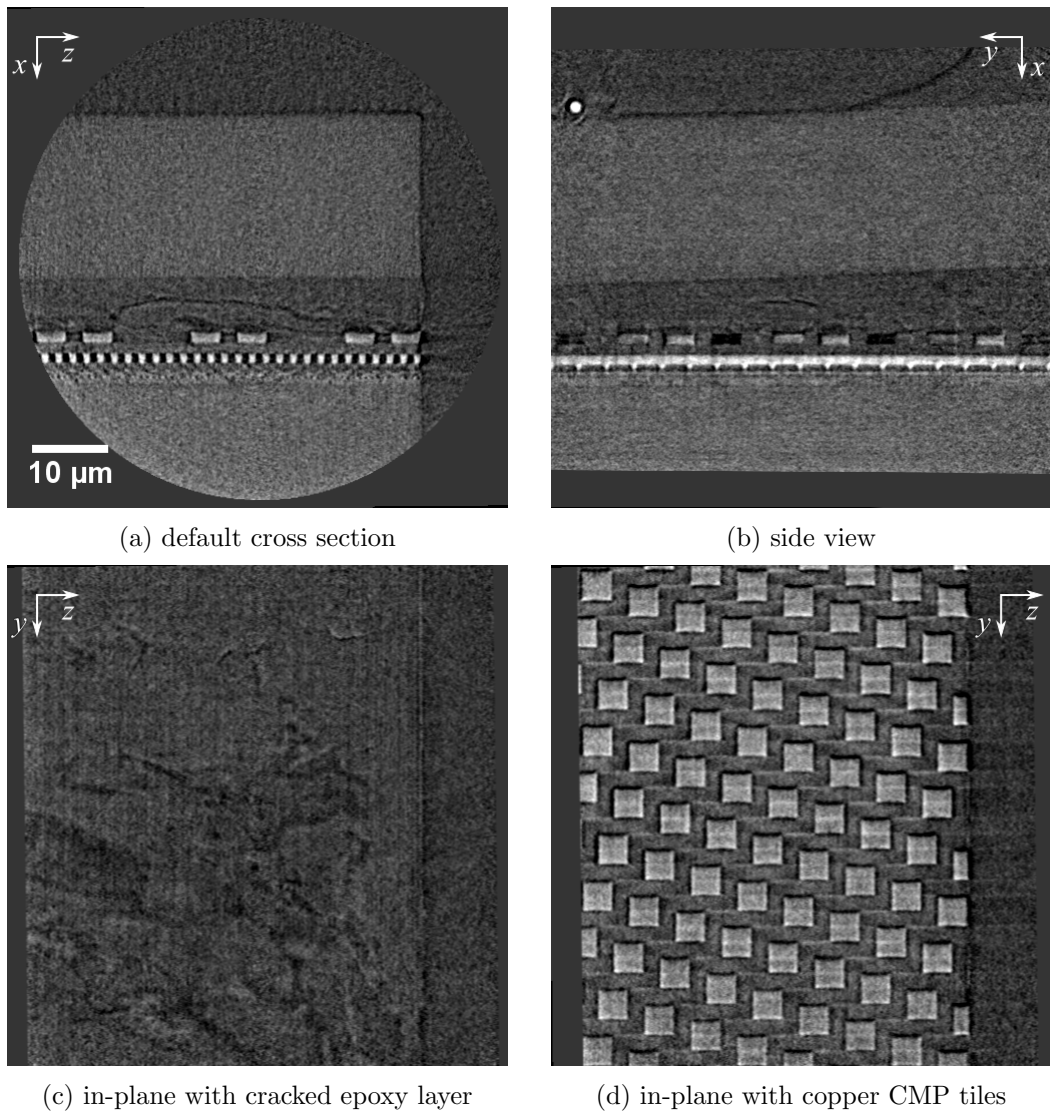


Figure 4.17.: Four virtual cross sections of the reconstructed volume.

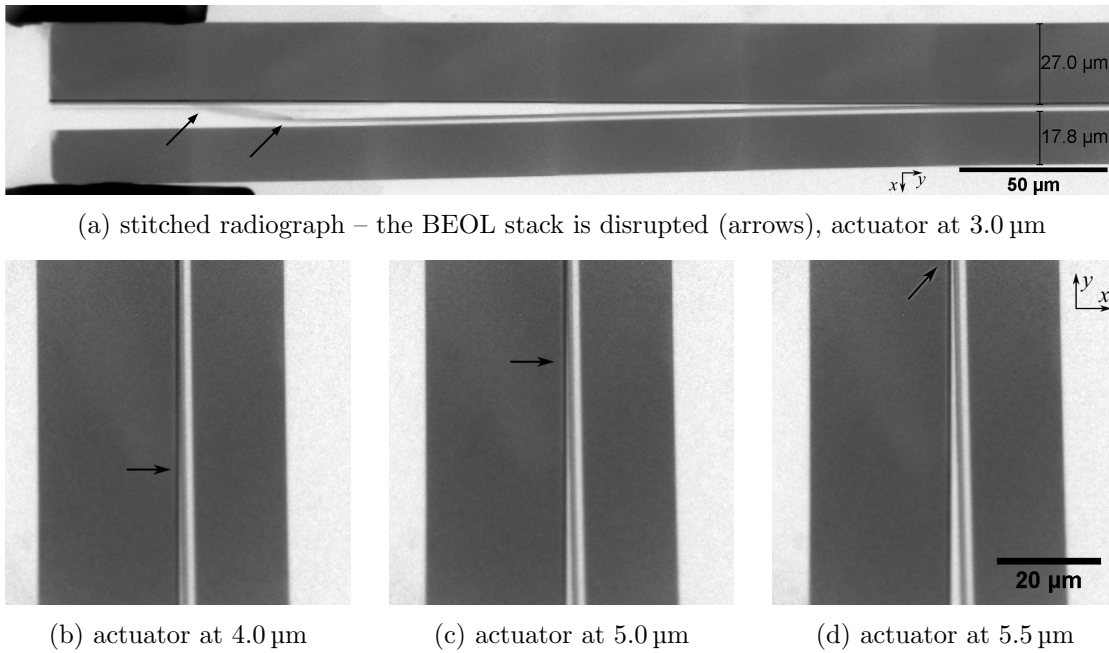


Figure 4.18.: MicroDCB experiment at a sample of type B (radiographs, absorption contrast, $10\times$ FZP). (b) to (d) show the same field of view, i.e. the sample stage was not moved while the crack was driven.

specimen underneath a stereo microscope was dismissed. The PAM-based method using reverse-action tweezers significantly decreased the risk of sample loss during mounting. The entire procedure is described in section 4.4. Those modifications are considered as substantial improvement of sample preparation. In particular, time and efforts were reduced, and the procedure became more reliable.

No spontaneous crack formation was observed for these samples in contrast to the former experiments with samples of type A. Thus, three methods were evaluated to facilitate crack initiation – FIB notching, the use of a tungsten knife inside the X-ray microscope, and the use of a razor blade at the PAM (see pp. 85 – 86). FIB notching and the application of the tungsten knife did not result in a successful experiment. This is assumed to be caused by the short depth of the generated notch. The use of a razor blade turned out to be the method of choice for this kind of specimens.

Two examples will be shown to demonstrate basic capabilities of the MicroDCB experiment. In both cases, an arbitrary flawless specimen was selected and mounted to the *MicroDCB tester*. The displacement of the actuator was increased in few steps of $0.5\ \mu\text{m}$, and either radiographs or tomographies were acquired at a constant displacement.

The first specimen is assumed to originate from a homogeneous region at a central part of the chip, because no particular features are observed in the radiograph. Fig. 4.18a shows a stitched radiograph of the specimen at the beginning of the experiment. The BEOL stack was disrupted, i.e. one part is still attached to the original wafer, and another part was released from the original wafer still being bonded to the epoxy and

4. In-situ 3D investigations of crack propagation

the dummy wafer, see arrows in Fig. 4.18a. Crack propagation during increase of the displacement of the actuator is seen in Figs. 4.18b to 4.18d. The crack was driven until the maximum displacement of the actuator of $13\ \mu\text{m}$ was reached. Dimensions were measured at suitable radiographs: $a = 618\ \mu\text{m}$, $o = 30.5\ \mu\text{m}$, $h_1 = 27.0\ \mu\text{m}$, $h_2 = 17.8\ \mu\text{m}$, $t = 60\ \mu\text{m}$, and $b = 60\ \mu\text{m}$. Thus, the parameters related to fracture mechanics can be estimated using eqs. 4.10 and 4.9:

$$\begin{aligned} G_c &= 5.5\ \text{J} \cdot \text{m}^{-2} \\ F_{\text{mount}} &= 4.4\ \text{mN} \end{aligned}$$

The previous experiment at samples of type A showed a hinged support due to a partial detachment of the adhesive (Fig. 4.15). In this experiment, the mount almost acts as a fixed support for both beams. The calculated value of G_c is in the expected range for ULK materials (cf. Fig. 4.2).

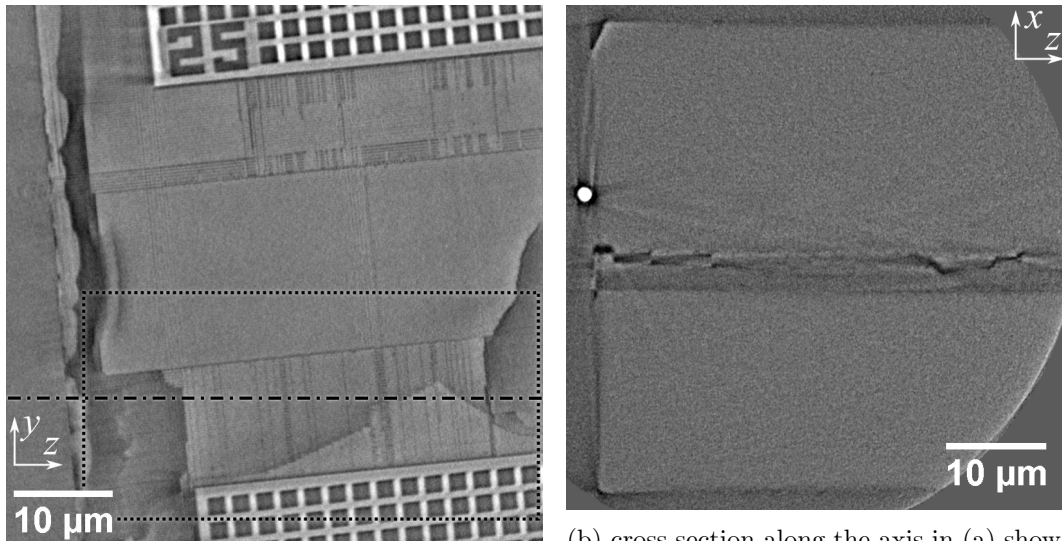
The second specimen of type B was investigated in more detail. Several tomographies were acquired at the region of the crack front for this specimen at different load steps⁸. The specimen is assumed to originate from a test structure within a scribe line of the wafer. In particular, numbered contact pads with a size of $40 \times 40\ \mu\text{m}^2$ are well centered within the MicroDCB specimen. The initial crack is trapped between two of these pads, which appear as a massive rectangular structure at the bottom and at the top inside the reconstructed virtual cross section in Fig. 4.19a. Few effects of cracking are seen at the bottom close to the contact pad. Fig. 4.19c contains a collection of cross sections of this region at several depths. The formation of the complex crack front is well reconstructed. In particular, no crack is seen in M1 (depth = $2.28\ \mu\text{m}$), whereas a crack through the metallization layer is seen for subsequent layers – for instance at $1.63\ \mu\text{m}$.

Fig. 4.19b contains a cross section being oriented perpendicularly to the long axis of the specimen. The crack front has a steplike shape, i.e. it crosses several interfaces and metallization layers. Fig. 4.20 shows two virtual cross sections at the same position of the specimen at two load steps. Some crack propagation is noticed beside the contact pad. However, the existent contact pads in this specimen act as an efficient crack-stop structure and they inhibit a continuous crack propagation through the specimen.

These experiments provide the proof of concept of the MicroDCB experiment. In particular, crack propagation through the BEOL stack was achieved and investigated by CT. One of both specimens of type B contained a number of contact pads, which acted as efficient crack stops. Thus, no continuous crack propagation was observed in

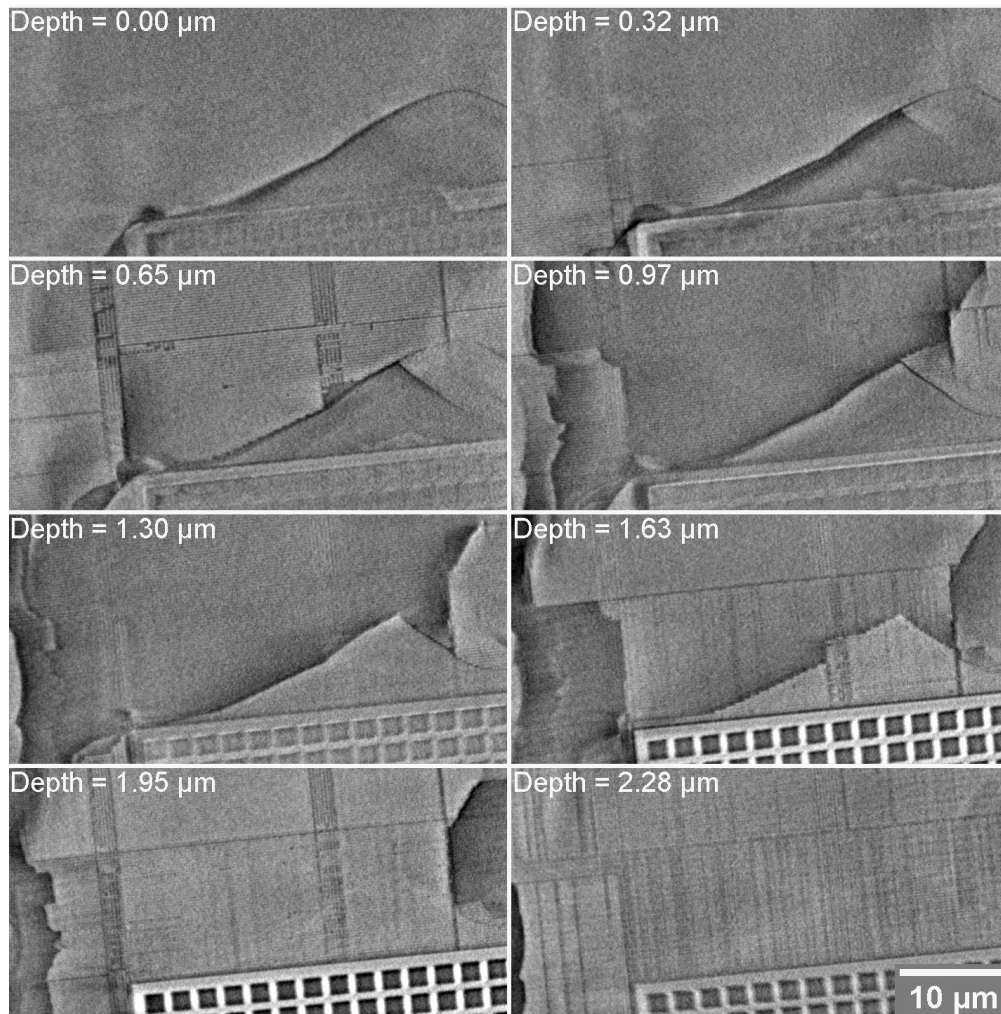
⁸Typical acquisition parameters: 601 projections ranging from -90° to $+90^\circ$ à 210 s at binning 1 ($1024 \times 1024\ \text{px}$) using the $10\times$ FZP in Zernike phase contrast. In total 40 h including reference image acquisition.

4.5. Application to microelectronic products



(a) in-plane cross section in the BEOL stack

(b) cross section along the axis in (a) showing the crack crossing several layers



(c) virtual in-plane cross sections at several depths of the indicated area in (a) showing a complex crack front

Figure 4.19.: Tomography of the volume containing the crack front between two contact pads (Zernike phase contrast, $10\times$ FZP, actuator at $2.5\ \mu\text{m}$).

4. In-situ 3D investigations of crack propagation

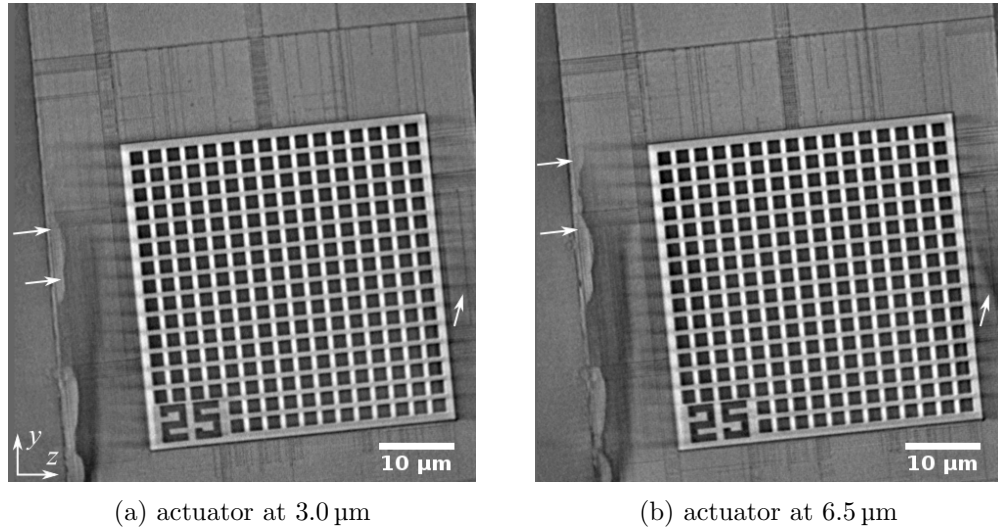


Figure 4.20.: In-plane cross sections in the BEOL stack. The investigated region was moved away from the mount compared to Fig. 4.19a. Crack propagation is observed after the increase of the position of the actuator (arrows).

contrast to the other specimen. Further aspects that have to be considered for future experiments will be summarized in chapter 5.

4.6. Examples of further applications

The application of the MicroDCB test is – as well as the macroscopic DCB test – not limited to investigations of samples from semiconductor industry. But it has to be considered, that the scope of this set-up is the visualization of three-dimensional or time-dependent effects during crack propagation. The investigation of plane films under load will be unspectacular, unless time dependent effects are expected or a lateral structure is present – e.g. alternating regions with different adhesion properties.

The DCB test has already been applied to other materials systems that fulfill such conditions. Some applications are seen in the field of medicine and biology. Natural tissues have a rather complex structure that may influence crack propagation. For instance, skin [Wu+07] and bone [Mor+10] are subjects of recent DCB investigations, and microscopic studies can be of interest. The latter system was already studied with XRM [And+10]. Hard coatings are used in industrial application. In contrast to semiconductor industry, there are lower requirements to the quality of the layer deposition due to technical and economical reasons. Thus, local defects occur, which might originate from fabrication or events like impacts and scratches during operation. They may affect the mechanical stability of the hard coating. Such issues can be investigated with this or similar set-ups within an X-ray microscope. A microscopic DCB study on hard coatings was published using scanning electron microscopy at elevated temperatures [Liu+13].

4.6. Examples of further applications

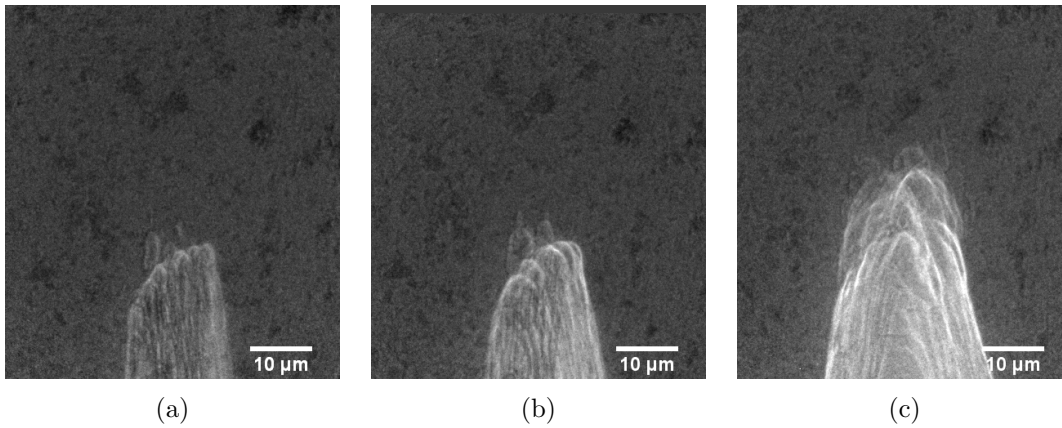
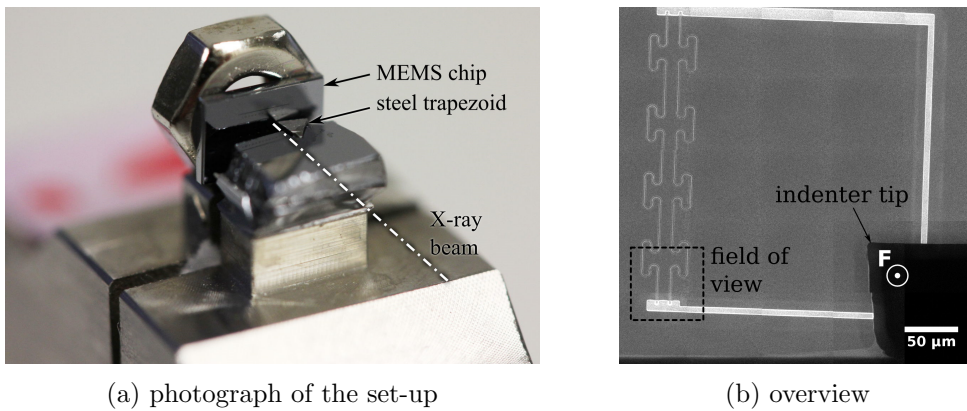
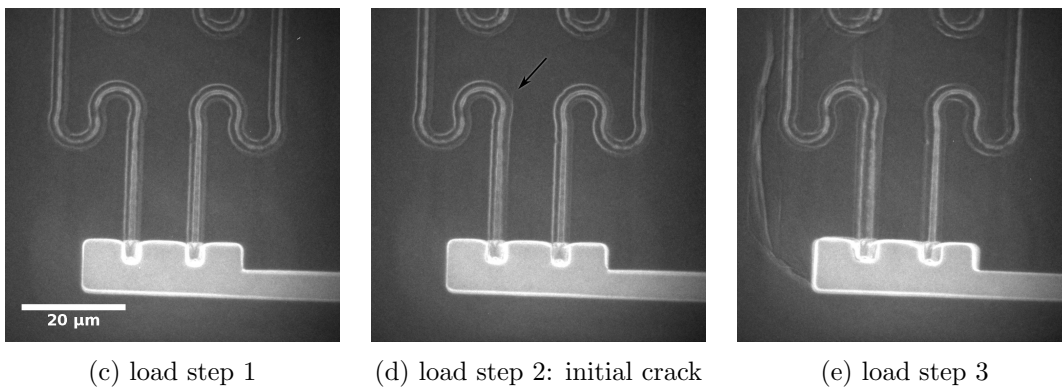


Figure 4.21.: Nafion tear test at three load steps. Zernike phase contrast, 10× FZP.



(a) photograph of the set-up

(b) overview



(c) load step 1

(d) load step 2: initial crack

(e) load step 3

Figure 4.22.: Bending test of a MEMS device [KD12] using the *MicroDCB tester* (Zernike phase contrast, 10× FZP).

4. In-situ 3D investigations of crack propagation

Some additional results of two basic mechanical experiments using the *MicroDCB tester* will be briefly presented to demonstrate further applications:

Nafion filled with platinum particles was used for first experiments to evaluate basic operation and handling of the tester [JD11]. This material has a heterogeneous structure due to the addition of microscopic particles, which may influence cracking. Bars with outer dimensions of approximately $0.1 \times 0.1 \times 2 \text{ mm}^3$ were prepared with a razor blade and a notch was cut in one end of the specimen. Fig. 4.21 shows three radiographs of the crack tip. Crack propagation was achieved with abrupt movements of the actuator to compensate for creep of the viscoelastic material. A complex crack front is observed due to the heterogeneous material.

The *MicroDCB tester* was used in a different configuration to act as a kind of micro-indentation system. Here, the failure mechanism in a microelectromechanical system (MEMS) under mechanical load was investigated [KD12]. The center of the chip is thinned by etching its back side to a thickness of approximately $80 \mu\text{m}$. A kind of cantilever was fabricated, which is released from its surrounding at three sides and the fourth side is electrically isolated from the substrate (Fig. 4.22b). The isolation is realized with a meander-shape trench structure being filled with silicon dioxide. This trench represents the weak part of the system. The chip was mounted vertically on top of the *MicroDCB tester* using a temporary set-up. A steel trapezoid is mounted on the other side to act as an indenter perpendicular to the surface of the cantilever (Fig. 4.22a). Radiographs were acquired while the load was increased. In total, four experiments were done. In one case, an initial crack was observed at the base of one arch of the meander structure (Fig. 4.22d) prior to the catastrophic failure (Fig. 4.22e). Such studies reveal the critical locations of the MEMS design, in particular if the initial crack is observed. The observations are supposed to be compared with results of finite element analysis, which predict positions with stress concentrations. Thus, the design can be modified to specifically avoid crack initiation at these positions.

5. Conclusions and outlook

The results of this thesis show, that crossed partial multilayer Laue lenses can be used for full-field X-ray microscopy (section 3.6). These lenses were integrated in a laboratory X-ray microscope using Cu-K α radiation with a photon energy of $E = 8.05$ keV. They have a focal length of 8.0 mm and a size of the aperture of 48 μm . Sub-100 nm resolution was demonstrated with prototype MLLs at a reasonable efficiency in comparison to the presently used Fresnel zone plates. In particular, Cu-K β radiation turned out to be critical, and it needs to be suppressed with a nickel filter, if a capillary condenser is used to provide the illumination of the specimen.

The fabrication of a single MLL is based on a silicon wafer that is coated with a multilayer stack of alternating WSi₂ and Si layers. The thicknesses of those layers follow the zone plate law, and only a section of the complete aperture starting at the outermost, thinnest layers and ending at the thicker layers at one side of the optical axis is actually deposited. Thus, a *partial* MLL is obtained, which shows one-dimensional focusing and imaging behavior. Each lens is prepared on a wafer stripe, which is obtained by precision sawing (section 3.2). The micromachining capabilities of a focused ion beam system are subsequently utilized to mill the eventual lens device on the stripe. In particular, its thickness in beam direction is adjusted to the intended application and photon energy. Two of these single MLLs with matched focal lengths are assembled in series to *crossed* MLLs as a compact lens device by glue bonding. This approach reduces the necessary effort to align the lenses for applications in full-field and scanning XRM. Both single MLLs are obtained from the same wafer, since a slight gradient in layer thickness is employed to achieve different focal lengths.

Section 3.3 describes a set of methods to perform an extensive characterization of the multilayer stack and of individual MLLs using in-house XRM and SEM without any need for experiments with synchrotron radiation. Thus, a prompt feedback to the preparation is possible. The optical properties of single and crossed MLLs were simulated with two approaches using geometrical optics and physical optics (section 3.4). Both types of simulations provide complementary information of the imaging and focusing properties of these diffractive lenses. Particularly, an image formation aside the optical axis, which is preferred for partial MLLs, turned out to be mandatory to separate the image from partially diffracted beams.

Section 3.7 summarizes general results of measurements using synchrotron radiation, which provide a more detailed characterization of single and crossed MLLs using transmission imaging and ptychography. Wedged MLLs – or more precisely diffractive lenses

5. Conclusions and outlook

with an ideal geometry [Sch06; Yan+07] – are necessary to get X-ray foci in the single nanometer range. The method to realize the wedged geometry by a stress layer, which is presented in section 3.8, is expected to be a promising approach to obtain such lenses. First experiments with synchrotron radiation proved an increased diffraction efficiency in comparison to a tilted MLL with same dimensions. The incline of the relative layer tilt θ along the height of the MLL h can be adjusted to the photon energy independently of the used multilayer coating to obtain optimized MLLs for X-ray focusing and imaging applications. A method to measure $\theta(h)$ using laboratory XRM, and thus, to quantify the geometrical modification prior to the application at synchrotron radiation facilities, is presented in section 3.3.

In general, the quality of the multilayer coating, the preparation and assembly of the crossed MLLs, and the stability of the experimental set-up need to be improved in future. Regarding full-field imaging, the present illumination is not assumed to be optimal for MLLs. The capillary condenser provides a rotationally symmetric hollow cone illumination, which has a diameter of 70 μm . Thus, the illumination is much larger than the field of view of the lens and it was truncated with a custom-built pinhole. The less efficient *phase contrast condenser* was used to exclude issues caused by the significant background of direct beams, which were expected for the *absorption contrast condenser*. This decision traces back to the straight-forward approach based on FZP alignment, i.e. generating the image in the center of the condenser ring using the existing $\varnothing 60 \mu\text{m}$ pinhole. Theoretical and experimental results show, that an image formation aside the natural optical path is essential for the application of MLLs. Thus, it is expected that the *absorption contrast condenser* can be used as well. Nevertheless, the rotationally symmetric illumination is optimized for requirements of FZPs and crossed MLLs might benefit from a dedicated non-hollow illumination of the object plane, whose size is matched to the field of view of the MLLs. On the other hand, such an illumination does not fulfill the typical requirements for Zernike phase contrast. Hence, it needs to be investigated if X-ray microscopy using crossed partial MLLs allows Zernike phase contrast imaging. Liquid-metal-jet X-ray sources [HOH03] allow larger power densities within the X-ray focus. The typical focus size of such a source is in the order of 10 μm and a gallium-based anode [Ote+08] is able to provide Ga-K α radiation with a high brilliance. It is obvious, this kind of source is apparently interesting to be used for laboratory X-ray microscopy.

Wedged MLLs are of interest for scanning XRM to enhance resolution and efficiency. This approach cannot be directly transferred to full-field imaging of extended objects [Sch06]. However, this issue is not yet sufficiently investigated in theory. In particular, resolution and efficiency will have contrary requirements at highest resolution, because a thinner MLL enlarges the accepted field of view but decreases diffraction efficiency. A moderately wedged MLL might reduce this trade-off to a certain extend.

Complete MLLs were investigated in section 3.5. The assembly of this kind of lenses using two partial MLLs has extreme requirements regarding tolerances. In addition,

these symmetric lenses show enhanced side lobes in case of X-ray focusing in comparison to a partial MLL with the same effective size of the aperture. This effect is caused by the mandatory beamstop, which blanks the central part of the aperture [YC12]. It is not expected that such a symmetric lens improves the directional imaging capabilities of serial crossed MLLs due to the image formation aside the optical axis. To summarize, partial MLLs are preferred to complete MLLs, because of the less complex fabrication and better optical performance. This finding is in agreement with [YC12].

Circular MLLs are another approach to realize Fresnel zone plates with high aspect ratios. Thus, no mixed-order imaging occurs. It can be assumed that this kind of lenses will be in particular beneficial for imaging. To date, available manufacturing processes and substrates – homogeneous and precise deposition on perfectly round wires – do not fulfill the geometrical requirements of such a diffractive lens. Hence, MLLs are expected to be a suitable approach to reach theoretical limits regarding resolution and efficiency in hard X-ray microscopy. To what extent volume diffraction limits or advances full-field imaging needs to be studied. In any case, emerging restrictions apply to both, circular and planar multilayer Laue lenses, whereas MLLs provide better experimental possibilities at the moment.

✱

The double cantilever beam test was successfully transferred to a miniaturized set-up in this thesis. The custom-made *MicroDCB tester* was integrated in the commercial X-ray microscope *NanoXCT-100*. Specimens originating from a microelectronics test chip were prepared as a sandwich-like structure with outer dimensions of $50 \times 50 \times 1000 \mu\text{m}^3$ to match the field of view of the X-ray microscope. Two other examples of in-situ crack observation at a Pt-filled Nafion foil and at a MEMS device were presented to emphasize related experiments. The specimens are mounted on the top of the fixture. This solution does not put any constraints to acquire tomographies, i.e. a full rotation is possible and no shadowing due to adjacent parts of the fixture occurs.

Crack propagation within the BEOL stack of the test chip was achieved under load. Radiographs along the crack front were used to monitor the overall crack propagation after each increase of the displacement of the actuator. Tomographies were subsequently acquired at fixed displacements for detailed studies. No distortions were detected in the reconstructed dataset. This is a clear indication that the present set-up is able to perform this kind of in-situ investigations.

One randomly selected specimen contained several contact pads, which act as a crack-stop structure. Hence, a continuous crack propagation through the BEOL stack was not observed, but few locations with crack growth were identified. The behavior at both sidewalls of the specimen differs from the behavior at its center. Thus, it is concluded that microcracks at the sidewalls originating from the mechanical preparation have a significant influence on crack initiation and crack propagation. It is recommended for

5. *Conclusions and outlook*

future experiments to improve sample preparation to minimize such artifacts – e.g. by using a more gentle dicing blade or by polishing the sidewalls after sawing. This fact is of particular importance, because the finally considered studies using the 40× FZP are currently limited to the edge of the specimen (cf. Fig. 4.13), unless tomographies without the need for a marker can be acquired.

The experiments of this study showed the general capability of the MicroDCB experiment, but the random selection of specimens limited the significance of the results. Thus, a proper target preparation of a dedicated area of a test chip should be considered for following studies. Since the miniaturized and macroscopic DCB test provide complementary information, both experiments are supposed to be combined to obtain a comprehensive characterization of suitable test structures to address current and future challenges regarding reliability of microelectronics products.

A. Listings

Table A.1.: Overview of the fabricated MLLs. Horizontal lines inside the table indicate separate MLLs on different stripes. For crossed (+) and complete (||) MLLs, width and thickness for both single MLLs is given in subsequent rows. \sphericalangle indicates wedged geometry.

Name	Coating	FIB date	Width [μm]	Thickness [μm]		+	\sphericalangle	Comment
5741-0	PS 5741	27.07.2011	4×28	7.6, 2.5, 5.5, 13.0				4 thicknesses
5741-1	PS 5741	12.11.2011	16	5.8				
5741-2	PS 5741	12.11.2011	16	10.6				
5741-3	PS 5741	12.11.2011	16	13.5				
5741-RT	PS 5741	12.12.2011	20	14				resolution target
5741-C1	PS 5741	08.02.2012	65 65	6.8 6.6		yes		
5741-4	PS 5741	18.01.2012	200	3.5 – 45				wedge
5741-5	PS 5741	18.01.2012	65	6.5				
5741-6	PS 5741	18.01.2012	65	35				
5741-7	PS 5741	18.01.2012	65	13				
6056-R1	PS 6056	26.04.2012	63	4				
6053-1	PS 6053	27.04.2012	65	3				
6053-3	PS 6053	27.04.2012	65	4				
6056-M1	PS 6056	27.04.2012	63	3				
6056-M3	PS 6056	27.04.2012	63	4				
5741-2	PS 5741	25.07.2012	64	13.5				
5741-3	PS 5741	25.07.2012	64	19.5				
6053-4	PS 6053	27.07.2012	63	7.7				
6053-5	PS 6053	27.07.2012	63	11.1				
6056-1	PS 6056	26.07.2012	63	8.9				
6056-2	PS 6056	26.07.2012	63	10.7				
6056-C1	PS 6056	27.07.2012	63 63	10.8 11.3		yes		

A. Listings

6056-C2	PS 6056	18.09.2012	65 85	4 4	yes	
6056-P1	PS 6056	05.12.2012	100 100	5.2 4.8	yes	
6359-1	PS 6359	22.01.2013	65	5.25		
6359-2	PS 6359	18.01.2013	65	10.5		
6359-C1	PS 6359	17.01.2013	68 78	10.5 10.5	yes	
6359-FC	PS 6359	02.02.2013	75	10.5		free-cut
6056-3	PS 6056	23.01.2013	62	5.25		plus 6.5 μm Si
6056-4	PS 6056	23.01.2013	62	10.5		plus 6.5 μm Si
6056-P2	PS 6056	05.03.2013	65 65	4.0 4.2	yes	plus 6.5 μm Si
6056-W1	PS 6056	19.06.2013	62	5.25		yes
6056-W2	PS 6056	19.06.2013	62	10.5		yes
<i>Beamtime ESRF Mi1168</i>						
6359-CW1	PS 6359	25.10.2013	85 85	13 13	yes	yes
6359-SW1	PS 6359	25.10.2013	85	13		yes
6359-CW2	PS 6359	28.10.2013	85 85	8.0 8.0	yes	yes
6359-SW2	PS 6359	28.10.2013	85	8.0		yes
6359-CF2	PS 6359	28.10.2013	85 85	4.0 4.0	yes	no
6359-SF2	PS 6359	28.10.2013	85	4.0		no
6359-SF3	PS 6359	28.10.2013	85	8.0		no

Table A.2.: List of beamtimes at synchrotron radiation facilities

Title of the proposal			
Beamline	Experiment ID	Date	Days
Participants			
Adiabatically Focusing Lenses (AFLs) - Focusing Hard X Rays to Nanometer Dimensions			
PETRA III P06	I-20110799	April/May 2012	4
J. Patommel, A. Kubec, S. Niese, S.Ritter			
Multilayer laue lenses: Optics characterization and application in X-ray microscopy of integrated circuits			
PETRA III P06	I-20120182	August 2012	6
S. Braun, A. Kubec, S. Niese, J. Patommel			
Investigation of improved multilayer laue lenses for X-ray point focusing			
PETRA III P06	I-20120745	Februar 2013	4
S. Braun, A. Kubec, S. Niese, J. Patommel, M. Rühl			
Hard X-ray focusing by multilayer Laue lenses with focal lengths > 10 mm			
ESRF ID13	Mi1168	November 2013	6
A. Kubec, S. Braun, S. Niese, J. Patommel, K. Melzer			

B. Source codes

Linear drift correction of series of radiographs

The subsequent macro can be run in *ImageJ*. It processes an image stack containing all radiographs of one averaging series and applies a certain horizontal and vertical translation on each slice before they are averaged. The value of the shift is linearly increased for each slice up to a given maximum value. A hyperstack of averaged slices with varying maximum shifts in horizontal and vertical direction will be generated, if *Mosaic X* or *Mosaic Y* is set to any value greater than 1. Otherwise, all slices of the current stack are accordingly translated.

```
1 // global variables
2 var rds_dx = 0;
3 var rds_dy = 0;
4 var rds_mx = 1;
5 var rds_my = 1;
6
7 macro "Repair_drift_stack" {
8 // use line selection for initial guess of the shift?
9 getLine(x1, y1, x2, y2, lineWidth);
10 if(x1 != -1) {
11     rds_dx = x1-x2;
12     rds_dy = y1-y2;
13 }
14
15 // user input dialog
16 Dialog.create("Shift");
17 Dialog.addNumber("Center_shift_X", rds_dx, 1, 7, "px");
18 Dialog.addNumber("Center_shift_Y", rds_dy, 1, 7, "px");
19 Dialog.addNumber("Mosaic_X", rds_mx, 1, 7, "px");
20 Dialog.addNumber("Mosaic_Y", rds_my, 1, 7, "px");
21 Dialog.show();
22 rds_dx=Dialog.getNumber();
23 rds_dy=Dialog.getNumber();
24 rds_mx=Dialog.getNumber();
25 rds_my=Dialog.getNumber();
26 tit = getTitle();
27 rtit = getTitle()+"-DriftCorrected";
28 ttit = getTitle()+"-tmp";
29 imgwidth = getWidth();
30 imgheight = getHeight();
31
32 // create Hyperstack to find best shift values
33 if(rds_mx>1 || rds_my>1) {
34     run("Hyperstack...", "title=["+rtit+"]_type=32-bit_display=Grayscale_width="+imgwidth+"_
35         height="+imgheight+"_channels=1_slices="+rds_mx+"_frames="+rds_my+"_label");
36     for(ix=0; ix<rds_mx; ix++) {
37         for(iy=0; iy<rds_my; iy++) {
38             selectWindow(tit); wait(50);
39             run("Duplicate...", "title=["+ttit+"]_duplicate_range=1-"+nSlices);
40             for(i=2; i<=nSlices; i++) {
41                 setSlice(i);
42                 dx = (rds_dx - (rds_mx-1)/2 + ix) * (i-1)/(nSlices-1);
43                 dy = (rds_dy - (rds_my-1)/2 + iy) * (i-1)/(nSlices-1);
44                 run("Translate...", "x="+dx+"y="+dy+"_interpolation=Bicubic_slice");
45             };
46             run("Z_Project...", "start=1-stop="+nSlices+"_projection=Median");
47             run("Copy");
48             close();
49         }
50     }
51 }
```

B. Source codes

```
48         selectWindow(ttit); wait(50);
49         close();
50         selectWindow(rtit); wait(50);
51         Stack.setSlice(ix+1);
52         Stack.setFrame(iy+1);
53         run("Paste");
54         setMetadata("Label", "dx="+dx+"_dy="+dy);
55     }
56 }
57 }
58
59 // create final drift corrected stack
60 else {
61     run("Duplicate...", "title=["+getTitle()+"-DriftCorrected"]_duplicate_range=1-"+nSlices);
62     for(i=2;i<=nSlices; i++) {
63         setSlice(i);
64         dx = rds_dx*(i-1)/(nSlices-1);
65         dy = rds_dy*(i-1)/(nSlices-1);
66         run("Translate...", "x="+dx+"_y="+dy+"_interpolation=Bicubic_slice");
67     }
68 }
69 }
```

Measure Layer Thicknesses (ImageJ plugin)

The subsequent plugin can be run in *ImageJ*. It analyzes a line profile on e.g. an SEM image and calculates the widths of alternating layers.

```
1  import ij.*;
2  import ij.measure.*;
3  import ij.plugin.filter.PlugInFilter;
4  import ij.process.*;
5  import ij.gui.*;
6  import java.awt.*;
7  import java.util.*;
8
9  /**
10     (c) Sven Niese, Fraunhofer IZFP Dresden
11  */
12
13  public class Measure.Layer.Thicknesses implements PlugInFilter {
14
15     ImagePlus imp;
16     boolean normalizeIntensity = false;
17     double cutfac = 0.5;
18     boolean onTop = false;
19     double [] vv;
20     double [] xx;
21     double [] fitMarksX;
22     double [] fitMarksY;
23     double min = 0;
24     double max = 0;
25     double mid = 0;
26     int w = 0;
27     int l = 0;
28     int f = 0; // for fitMarks
29     Plot p = null;
30     static PlotWindow pw1 = null;
31     static PlotWindow pw2 = null;
32
33     public int setup(String arg, ImagePlus imp) {
34         if (IJ.versionLessThan("1.17j"))
35             return DONE;
36         this.imp = imp;
37         return DOES_8G+DOES_16+DOES_32;
38     }
39
40     public void run(ImageProcessor ip) {
41         Roi roi = imp.getRoi();
42         if(roi==null || !roi.isLine()) {
43             IJ.showMessage("Plugin_needs_line_selection");
44             return;
45         }
46     }
```

```

46
47 // close old windows
48 if(pw1 != null && !pw1.isClosed()) pw1.close();
49 if(pw2 != null && !pw2.isClosed()) pw2.close();
50
51 String unit = "[" + imp.getCalibration().getUnit() + "]";
52 Line line = (Line)roi;
53 vv = line.getPixels();
54 l = vv.length;
55 xx = new double[l];
56 fitMarksX = new double[l];
57 fitMarksY = new double[l];
58 double [] midPositions = new double[l];
59 double length = line.getLength();
60 double summin=0, summax=0;
61 int nmin=0, nmax=0, m=0;
62
63 for(int i=0; i<l; i++)
64     xx[i] = length*i/(l-1);
65
66 if(normalizeIntensity){
67     SquareFunction sfunc = new SquareFunction();
68     double mean = Stats.mean(vv);
69     double [] para = new double[3];
70     para[0] = 0.;
71     para[1] = 0.;
72     para[2] = mean;
73     sfunc.setFitData(xx, vv);
74     sfunc.setParameter(para);
75     try {
76         sfunc.doFit();
77         for(int i=0; i<l; i++)
78             vv[i] = vv[i] * mean / sfunc.getFitValue(xx[i]);
79     } catch (Exception e){
80         IJ.log("Hoppla_" + e.toString());
81         e.printStackTrace();
82     };
83 }
84
85 min = Stats.min(vv);
86 max = Stats.max(vv);
87 mid = (min+max) / 2;
88
89 for(int i=0; i<l; i++) {
90     if(vv[i] < mid) {
91         summin += vv[i];
92         nmin++;
93     } else {
94         summax += vv[i];
95         nmax++;
96     }
97 }
98
99 min = summin / nmin;
100 max = summax / nmax;
101 mid = (min+max) / 2;
102 onTop = vv[0]>mid;
103
104 double [] x = {xx[0],xx[l-1]};
105 double [] y = {min,min};
106 p = new Plot("Layer_thickness", "Position_"+unit, "Value", xx, vv);
107 p.setColor(Color.BLACK);
108 p.draw();
109 p.setColor(Color.BLUE);
110 p.addPoints(x, y, Plot.LINE);
111 y[0] = max; y[1] = max;
112 p.addPoints(x, y, Plot.LINE);
113
114 for(int i=1; i<l; i++) {
115     if((!onTop && vv[i]<mid) || (!onTop && vv[i]>mid)) {
116         midPositions[m++] = findMidPos(i);
117         i += w;
118         onTop = !onTop;
119     }
120 }
121
122 double [] midVal = new double[m];
123 midPositions = resizeArray(midPositions, m);

```

B. Source codes

```
124     for(int i=0; i<m; i++)
125         midVal[i] = mid;
126     p.setColor(Color.RED);
127     p.addPoints(midPositions, midVal, Plot.TRIANGLE);
128
129     fitMarksX = resizeArray(fitMarksX, f);
130     fitMarksY = resizeArray(fitMarksY, f);
131     p.setColor(Color.BLUE);
132     p.addPoints(fitMarksX, fitMarksY, Plot.CIRCLE);
133
134     pw1 = p.show();
135     pw1.setLocation(1,1);
136
137     ResultsTable r = new ResultsTable();
138     double [] idx = new double[m-1];
139     double [] widths = new double[m-1];
140     double [] idxAvg = new double[(m-1)/2];
141     double [] avgWidth = new double[(m-1)/2];
142     for(int i=0; i<m-1; i++) {
143         idx[i] = i+1;
144         widths[i] = midPositions[i+1] - midPositions[i];
145         r.incrementCounter();
146         r.addValue("Width_"+unit, widths[i]);
147         if(i%2==1) {
148             idxAvg[i/2] = i+0.5;
149             avgWidth[i/2] = (widths[i-1]+widths[i])/2;
150             r.addValue("Avg_width_"+unit, avgWidth[i/2]);
151         }
152     }
153
154     p = new Plot("Layer_thickness", "Index", "Width_"+unit, idx, widths);
155     p.draw();
156     p.setColor(Color.BLUE);
157     p.addPoints(idxAvg, avgWidth, Plot.CIRCLE);
158     pw2 = p.show();
159     pw2.setLocation(1,pw1.getHeight()+1);
160     r.show("Layer_thickness");
161 }
162
163 private double findMidPos(int i) {
164     double d = (max - mid) * cutfac;
165     int iLeft = 0;
166     int iRight = l-1;
167     for(int j=i; j>=0; j--)
168         if( Math.abs(vv[j]-mid) > d ) {
169             iLeft = j;
170             break;
171         }
172
173     for(int j=i; j<l; j++)
174         if( Math.abs(vv[j]-mid) > d ) {
175             iRight = j;
176             break;
177         }
178
179     w = iRight - i;
180
181     int l2 = iRight - iLeft + 1;
182     double [] xx2 = new double[l2];
183     double [] vv2 = new double[l2];
184     double [] vv2Fit = new double[l2];
185
186     for(int j=0; j<l2; j++) {
187         vv2[j] = vv[iLeft+j];
188         xx2[j] = xx[iLeft+j];
189     }
190     fitMarksX[f] = xx2[0];
191     fitMarksY[f++] = vv2[0];
192     fitMarksX[f] = xx2[l2-1];
193     fitMarksY[f++] = vv2[l2-1];
194
195     CurveFitter sfunc = new CubicFunction();
196     double [] para = new double[4];
197     para[0] = 0.;
198     para[1] = 0.;
199     para[2] = 0;
200     para[3] = mid;
201     sfunc.setFitData(xx2, vv2);
```

```

202     sfunc.setParameter(para);
203     try {
204         sfunc.doFit();
205     } catch (Exception e){
206         LinearFunction lfunc = new LinearFunction();
207         double [] lpara = new double [2];
208         lpara [0] = 0.;
209         lpara [1] = mid;
210         lfunc.setFitData(xx2, vv2);
211         lfunc.setParameter(lpara);
212         try {
213             lfunc.doFit();
214             sfunc = lfunc;
215         } catch (Exception e2){
216             IJ.log("Hoppla_" + e2.toString());
217             e2.printStackTrace();
218             return 0.;
219         }
220     }
221
222     for(int j=0; j<12; j++)
223         vv2Fit[j] = sfunc.getFitValue(xx2[j]);
224
225     p.setColor(Color.RED);
226     p.addPoints(xx2, vv2Fit, Plot.LINE);
227
228     try {
229         double res = sfunc.fitFindXbyNewton(mid, xx[i]);
230         return res;
231     } catch (Exception e) {
232         IJ.log("Hoppla_" + e.toString());
233         e.printStackTrace();
234         return 0.;
235     }
236 }
237
238 private double [] resizeArray(double [] array, int newSize) {
239     if(newSize<1 || newSize>array.length)
240         return array;
241     double [] newArray = new double [newSize];
242     for(int i=0; i<newSize; i++)
243         newArray[i] = array[i];
244     return newArray;
245 }
246
247 private class LinearFunction extends CurveFitter{
248     public double fitFunction(double x, double [] p, double [] pder){
249         // y = a*x + b;
250         double a = p[0];
251         double b = p[1];
252         if(pder!=null){
253             pder[1] = x; // a
254             pder[2] = 1; // b
255         }
256         return a*x + b;
257     }
258
259     @Override
260     public double fitFunctionDer(double x) {
261         return parameter[0];
262     }
263 }
264
265 private class SquareFunction extends CurveFitter{
266     public double fitFunction(double x, double [] p, double [] pder){
267         // y = a*x^2 + b*x + c;
268         double a = p[0];
269         double b = p[1];
270         double c = p[2];
271         if(pder!=null){
272             pder[0] = x*x; // a
273             pder[1] = x; // b
274             pder[2] = 1; // c
275         }
276         return a*x*x + b*x + c;
277     }
278
279     @Override

```

B. Source codes

```
280     public double fitFunctionDer(double x) {
281         return 2*parameter[0]*x+parameter[1];
282     }
283 }
284
285 private class CubicFunction extends CurveFitter{
286     public double fitFunction(double x, double [] p, double [] pder){
287         // y = a*x^3 + b*x^2 + c*x + d;
288         double a = p[0];
289         double b = p[1];
290         double c = p[2];
291         double d = p[3];
292         if(pder!=null){
293             pder[0] = x*x*x; // a
294             pder[1] = x*x;   // b
295             pder[2] = x;     // c
296             pder[3] = 1;    // d
297         }
298         return a*x*x*x + b*x*x + c*x + d;
299     }
300
301     @Override
302     public double fitFunctionDer(double x) {
303         return 3*parameter[0]*x*x+2*parameter[1]*x+parameter[2];
304     }
305 }
306
307 }
```

Eval Knife Edge (ImageJ plugin)

The subsequent plugin can be run in *ImageJ*. It analyzes a series of knife edge scans, typically provided as EDF file. The width of the transition is calculated and plotted.

```
1  import ij.*;
2  import ij.measure.*;
3  import ij.plugin.filter.PlugInFilter;
4  import ij.process.*;
5  import ij.gui.*;
6  import java.awt.*;
7  import java.util.*;
8
9  public class Eval.Knife.Edge implements PlugInFilter {
10
11     ImagePlus imp;
12
13     public int setup(String arg, ImagePlus imp) {
14         if (IJ.versionLessThan("1.17j"))
15             return DONE;
16         // Registration may help static fields from being reset but may
17         // also prevent 'Compile and Run' from reloading this class.
18         IJ.register(Eval.Knife.Edge.class);
19         this.imp = imp;
20         return DOES_8G+DOES_16+DOES_32;
21     }
22
23     public void run(ImageProcessor ip) {
24         int h = ip.getHeight();
25         int w = ip.getWidth();
26         double [] fwhm = new double[h];
27         double [] ypsilons = new double[h];
28         double direction = ( ip.getf(0,0) < ip.getf(w-1,0) ? 1 : -1 );
29         String unit = "[" + imp.getCalibration().getUnit() + "]" ;
30
31         ResultsTable r = new ResultsTable();
32         ImageProcessor ip2 = new FloatProcessor(w, h);
33         ImageProcessor ip3 = new FloatProcessor(w, h);
34         ImageProcessor ip4 = new FloatProcessor(w, h);
35
36         for(int y=0; y<h; y++) {
37             ErfFunction EF = new ErfFunction();
38             double [] para = new double[4];
39             double [] xx = new double[w];
```



```

40     double [] yy = new double[w];
41
42     for(int x=0; x<w; x++) {
43         xx[x] = x;
44         yy[x] = ip.getf(x,y);
45     }
46
47     para[0] = (yy[w-1]-yy[0])/2; // amp
48     para[3] = (yy[w-1]+yy[0])/2; // offset
49     para[2] = 3; // width
50     para[1]=Math.PI;
51     for(int x=0; x<w && para[1]==Math.PI; x++) {
52         if(para[0]>0 && yy[x] > para[3])
53             para[1] = x; // xc
54         if(para[0]<0 && yy[x] < para[3])
55             para[1] = x;
56     }
57
58     EF.setFitData(xx, yy);
59     EF.setParameter(para);
60     try {
61         EF.doFit();
62         fwhm[y] = 1.665 * EF.parameter[2] * imp.getCalibration().pixelWidth;
63         ypsilons[y] = imp.getCalibration().getY(y);
64
65         r.incrementCounter();
66         r.addValue("Position_"+unit, ypsilons[y]);
67         //r.addValue("Height", EF.parameter[0]);
68         r.addValue("FWHM_"+unit, fwhm[y]);
69         r.addValue("Center_"+unit, imp.getCalibration().getY(EF.parameter[1]));
70         //r.addValue("Offset", EF.parameter[3]);
71     } catch (Exception e){
72         IJ.log("Hoppla_" + e.toString());
73         e.printStackTrace();
74     }
75 }
76
77 double amp = EF.parameter[0];
78 double sigma = EF.parameter[2] / Math.sqrt(2.);
79 int xoffset = (int)Math.round(w/2-EF.parameter[1]);
80 float ww = w;
81 for(int x=0; x<w; x++) {
82     ip2.setf(x, y, (float)EF.getFitValue(x));
83     ip3.setf(x, y, (float)(amp*Math.exp(-(x+.5-ww/2)/(2./sigma/sigma))));
84     int x2 = x - xoffset;
85     if(x2<0) x2 = 0;
86     if(x2>=w) x2 = w-1;
87     ip4.setf(x, y, ip.getf(x2,y));
88 }
89 }
90 ImageStack stack = new ImageStack(w, h);
91 stack.addSlice("Fit", ip2);
92 stack.addSlice("Aligned", ip4);
93 stack.addSlice("Deviation", ip3);
94 ImagePlus imp2 = new ImagePlus("Knife_Edge_Eval_of_"+imp.getTitle(), stack);
95 imp2.show();
96 imp2.setCalibration(imp.getCalibration());
97 r.show("Knife_Edge_Evaluation");
98 Plot p = new Plot("Knife_Edge_Evaluation", "Position_"+unit, "FWHM_"+unit, ypsilons, fwhm);
99 p.addPoints(ypsilons, fwhm, Plot.TRIANGLE);
100 p.show();
101 }
102
103 private class GaussFunction extends CurveFitter{
104     public double fitFunction(double x, double [] p, double [] pder){
105         if(pder!=null){
106             double v=Math.exp(-(x-p[1])*(x-p[1])/p[2]/p[2]);
107             pder[0]=v; // A/(w*sqrt(2*pi))
108             pder[1]=2*(x-p[1])/p[2]/p[2]*v*p[0]; // xc
109             pder[2]=2*(x-p[1])*(x-p[1])/p[2]/p[2]/p[2]*v*p[0]; // w
110             pder[3]=1.; // y0
111         }
112         return p[0]*Math.exp(-(x-p[1])*(x-p[1])/p[2]/p[2])+p[3];
113     }
114 }
115
116
117 private class ErfFunction extends CurveFitter{

```

B. Source codes

```
118 public double fitFunction(double x, double [] p, double [] pder){
119     double amp = p[0];
120     double xc = p[1];
121     double width = p[2];
122     double offset = p[3];
123
124     if(pder!=null){
125         double [] h = new double [p.length];
126         h[0] = h[3] = 0.1; // dummy
127         h[1] = 0.1;
128         h[2] = 0.1;
129         double [] pder2 = dfridr(x, p, h);
130         pder[0] = erf((x-xc)/width);
131         pder[1] = pder2[1];
132         pder[2] = pder2[2];
133         pder[3] = 1.;
134     }
135
136     return amp*erf((x-xc)/width)+offset;
137 }
138
139 // source: http://introcs.cs.princeton.edu/java/21function/ErrorFunction.java.html
140 // fractional error in math formula less than 1.2 * 10 ^ -7.
141 // although subject to catastrophic cancellation when z in very close to 0
142 // from Chebyshev fitting formula for erf(z) from Numerical Recipes, 6.2
143 public double erf(double z) {
144     double t = 1.0 / (1.0 + 0.5 * Math.abs(z));
145     // use Horner's method
146     double ans = 1 - t * Math.exp(-z*z - 1.26551223 + t * ( 1.00002368 + t * ( 0.37409196
147         + t * ( 0.09678418 + t * (-0.18628806 + t * ( 0.27886807 + t * (-1.13520398 + t *
148         ( 1.48851587 + t * (-0.82215223 + t * ( 0.17087277))))))));
149     if (z >= 0) return ans;
150     else return -ans;
151 }
152
153 // fractional error less than x.xx * 10 ^ -4.
154 // Algorithm 26.2.17 in Abramowitz and Stegun, Handbook of Mathematical.
155 public double erf2(double z) {
156     double t = 1.0 / (1.0 + 0.47047 * Math.abs(z));
157     double poly = t * (0.3480242 + t * (-0.0958798 + t * (0.7478556)));
158     double ans = 1.0 - poly * Math.exp(-z*z);
159     if (z >= 0) return ans;
160     else return -ans;
161 }
162 }
```

MLL Tilt Evaluation (ImageJ plugin)

The subsequent plugin can be run in *ImageJ*. It analyzes one or two stacks containing aligned tilt series of an aperture of an MLL. The resulting map shows the relative layer tilt.

```
1 import ij.*;
2 import ij.gui.*;
3 import ij.process.*;
4 import ij.plugin.*;
5 import ij.plugin.filter.*;
6 import ij.measure.Calibration;
7 import ij.plugin.frame.Recorder;
8 import ij.macro.Interpreter;
9
10 /**
11  * Evaluate NanoXCT tilt series images of wedged or otherwise elastically deformed MLL
12  */
13 public class MLL.Tilt.Evaluation implements Plugin {
14
15     private static String title1 = "";
16     private static String title2 = "";
17     private static int mode = 0;
18     private static float angleStep = 0.01f;
```

```

19 private static boolean fine = true;
20 private static boolean debug = false;
21 private int maxShift = 15;           // window for correlation calculation
22
23 /**
24  * Main routine
25  */
26 public void run(String arg) {
27     // Input dialog -> show window titles for selection
28     int[] wList = WindowManager.getIDList();
29     if (wList==null) {
30         IJ.noImage();
31         return;
32     }
33     String[] titles = new String[wList.length];
34     String[] modes = { "2_images", "Horizontal", "Vertical" };
35     for (int i=0; i<wList.length; i++) {
36         ImagePlus imp = WindowManager.getImage(wList[i]);
37         if (imp!=null)
38             titles[i] = imp.getTitle();
39         else
40             titles[i] = "";
41     }
42     GenericDialog gd = new GenericDialog("Wedged_MLL_tilt_evaluation", IJ.getInstance());
43     String defaultItem = title1.equals("") ? titles[0] : title1;
44     gd.addNumericField("Angle_step_size", angleStep, angleStep<0.01?4:3);
45     gd.addChoice("Image1:", titles, defaultItem);
46     defaultItem = title2.equals("") ? titles[0] : title2;
47     gd.addChoice("Image2:", titles, defaultItem);
48     gd.addChoice("Correlation_mode:", modes, modes[mode]);
49     gd.addCheckbox("Fine_evaluation", fine);
50     gd.addCheckbox("Debug", debug);
51     gd.showDialog();
52     if (gd.wasCanceled())
53         return;
54     angleStep = (float)(gd.getNextNumber());
55     int index1 = gd.getNextChoiceIndex();
56     int index2 = gd.getNextChoiceIndex();
57     mode = gd.getNextChoiceIndex();
58     fine = gd.getNextBoolean();
59     debug = gd.getNextBoolean();
60     title1 = titles[index1];
61     title2 = titles[index2];
62     ImagePlus img1 = WindowManager.getImage(wList[index1]);
63     ImagePlus img2 = WindowManager.getImage(wList[index2]);
64     ImagePlus img3 = null;
65
66     // calculate result
67     if (mode==0)
68         img3 = calculate(img1, img2);
69     else
70         img3 = calculate(img1, mode==1);
71     img3.getProcessor().multiply(angleStep);
72
73     // Show result
74     if (img3!=null) {
75         img3.show();
76         img3.getProcessor().setMinAndMax(-0.3, 0.3);
77     }
78 }
79
80 /**
81  * Calculation routine: take depth profiles of each pixel in both images, do a
82  * correlation and determine the offset of both information. The resulting image
83  * contains the offset map.
84  */
85 ImagePlus calculate(ImagePlus img1, ImagePlus img2) {
86     // Meta information
87     int size = img1.getStackSize();
88     int w = img1.getWidth();
89     int h = img1.getHeight();
90     if (size != img2.getStackSize() || w != img2.getWidth() || h != img2.getHeight()) {
91         IJ.error("Images_must_have_same_dimensions");
92         return null;
93     }
94
95     // Create stack objects and empty images for the results
96     ImageStack is1 = img1.getStack();

```

B. Source codes

```
97     ImageStack is2 = img2.getStack();
98     ImageStack isVis = null; // just for visualization & debugging
99     FloatProcessor [] ipVis = null;
100    FloatProcessor ip3 = new FloatProcessor(w, h);
101    ImagePlus img3 = new ImagePlus("Result", ip3);
102    ImagePlus imgVis = null;
103
104    if(debug) {
105        isVis = new ImageStack(w, h);
106        ipVis = new FloatProcessor[2*maxShift+1];
107        for(int i=0; i<2*maxShift+1; i++) {
108            ipVis[i] = new FloatProcessor(w, h);
109            isVis.addSlice(ipVis[i]);
110        }
111        imgVis = new ImagePlus("Result_Visualization", isVis);
112    }
113
114    // Get depth profiles
115    float [] line1 = new float[size];
116    float [] line2 = new float[size];
117    for(int y=0; y<h; y++) {
118        for(int x=0; x<w; x++) {
119            for(int z=0; z<size; z++) {
120                line1[z] = (float)(is1.getVoxel(x, y, z));
121                line2[z] = (float)(is2.getVoxel(x, y, z));
122            }
123            // put correlation value to ip3
124            ip3.setf(x, y, correlate(line1, line2, size, x, y, ipVis));
125        }
126        IJ.showProgress(1.*y/h);
127        if(IJ.escapePressed())
128            break;
129    }
130
131    if(debug) imgVis.show();
132    return img3;
133 }
134
135 /**
136  * Calculation routine: take depth profiles of each pixel in the image and also a
137  * reference in its center (horizontal/vertical line), do a correlation and determine
138  * the offset of both information. The resulting image contains the offset map.
139  */
140 ImagePlus calculate(ImagePlus img1, boolean horizontal) {
141     // Meta information
142     int size = img1.getStackSize();
143     int w = img1.getWidth();
144     int h = img1.getHeight();
145
146     if(horizontal)
147         img1.setRoi(new Line(1, h/2, w, h/2));
148     else
149         img1.setRoi(new Line(w/2, 1, w/2, h));
150
151     // Create stack objects and empty images for the results
152     ImageStack is1 = img1.getStack();
153     ImageStack isVis = null; // just for visualization & debugging
154     FloatProcessor [] ipVis = null;
155     FloatProcessor ip2 = new FloatProcessor(horizontal?w:h, size);
156     FloatProcessor ip3 = new FloatProcessor(w, h);
157     ImagePlus img3 = new ImagePlus("Result", ip3);
158     ImagePlus imgVis = null;
159
160     if(debug) {
161         isVis = new ImageStack(w, h);
162         ipVis = new FloatProcessor[2*maxShift+1];
163         for(int i=0; i<2*maxShift+1; i++) {
164             ipVis[i] = new FloatProcessor(w, h);
165             isVis.addSlice(ipVis[i]);
166         }
167         imgVis = new ImagePlus("Result_Visualization", isVis);
168     }
169
170     // Get depth profiles
171     float [] line1 = new float[size];
172     float [] line2 = new float[size];
173     int n = 0;
174 }
```

```

175     if(horizontal)
176         for(int y=(int)(h*5./11); y<h*6./11; y++, n++)
177             for(int x=0; x<w; x++)
178                 for(int z=0; z<size; z++)
179                     ip2.setf(x, z, ip2.getf(x,z) + (float)(is1.getVoxel(x, y, z)));
180     else
181         for(int x=(int)(w*5./11); x<w*6./11; x++, n++)
182             for(int y=0; y<h; y++)
183                 for(int z=0; z<size; z++)
184                     ip2.setf(y, z, ip2.getf(y,z) + (float)(is1.getVoxel(x, y, z)));
185     ip2.multiply(1./n);
186
187     for(int y=0; y<h; y++) {
188         for(int x=0; x<w; x++) {
189             for(int z=0; z<size; z++) {
190                 line1[z] = (float)(is1.getVoxel(x, y, z));
191                 line2[z] = (float)(ip2.getf(horizontal?x:y, z));
192             }
193             // put correlation value to ip3
194             ip3.setf(x, y, correlate(line1, line2, size, x, y, ipVis));
195         }
196         IJ.showProgress(1.*y/h);
197         if(IJ.escapePressed())
198             break;
199     }
200
201     if(debug) imgVis.show();
202     return img3;
203 }
204
205 /**
206  * Do the correlation of two line profiles
207  */
208 private float correlate(float [] line1, float [] line2, int size, int x, int y,
209     FloatProcessor [] visu) {
210     int n = 2*maxShift+1;
211     double [] v = new double[n]; // correlation value
212     int ii;
213     double maxV = 0.f;
214     int maxI = 0;
215     double sumY=0., sumXY=0., minV = 0.;
216     GaussFunction GF = new GaussFunction();
217
218     // Calculate correlation values for shifts from -maxShift to +maxShift
219     for(int i=-maxShift; i<=maxShift; i++) {
220         ii = i+maxShift;
221         v[ii] = 0.f;
222         for(int z=0; z<size; z++) {
223             int zz = z-i;
224             if(zz<0) zz += size;
225             if(zz>=size) zz -= size;
226             v[ii] += line1[z] * line2[zz];
227             if(debug)
228                 visu[ii].setf(x, y, (float)v[ii]);
229         }
230
231         // Find maximum & minimum
232         if(v[ii] > maxV) {
233             maxV = v[ii];
234             maxI = i;
235         }
236         if(v[ii] < minV || ii==maxShift)
237             minV = v[ii];
238     }
239
240     // get values around peak
241     double [] xF = new double[9];
242     double [] vF = new double[9];
243     if(maxI-4>=-maxShift && maxI+4<=maxShift)
244         minV = Math.min(v[maxI-4+maxShift], v[maxI+4+maxShift]);
245
246     for(int i=maxI-4; i<=maxI+4; i++) {
247         if(i>=-maxShift && i<=maxShift) {
248             sumY += (v[i+maxShift] - minV);
249             sumXY += (v[i+maxShift] - minV)*i;
250             xF[i-maxI+4] = i;
251             vF[i-maxI+4] = v[i+maxShift];
252         }
253     }

```

B. Source codes

```
252     }
253     if (!fine)
254         return (float)(sumXY/sumY); // Return center of gravity
255
256     // Fit & return center of correlation function
257     double [] FP=new double[4];
258     FP[0]=vF[4]-vF[0]; FP[1]=maxI; FP[2]=3; FP[3]=vF[0];
259     GF.setFitData(xF, vF);
260     GF.setParameter(FP);
261     try{
262         GF.doFit();
263     } catch (Exception e) {
264         IJ.log("Hoppla_(fit_error)");
265         return -110;
266     }
267     if(GF.parameter[1] < -maxShift || GF.parameter[1] > maxShift)
268         return -100;
269     return (float)(GF.parameter[1]);
270 }
271
272 // Fit x & y values to a Gaussian curve
273 // Uses class CurveFitter by Dr. P. Krueger
274 private class GaussFunction extends CurveFitter{
275     public double fitFunction(double x, double [] p, double [] pder){
276         if(pder!=null){
277             double v=Math.exp(-(x-p[1])*(x-p[1])/p[2]/p[2]);
278             pder[0]=v;
279             pder[1]=2*(x-p[1])/p[2]/p[2]*v*p[0];
280             pder[2]=2*(x-p[1])*(x-p[1])/p[2]/p[2]/p[2]*v*p[0];
281             pder[3]=1.;
282         }
283         return p[0]*Math.exp(-(x-p[1])*(x-p[1])/p[2]/p[2])+p[3];
284     }
285 }
286
287 }
```

Communication with the E-709 piezo controller

The communications protocol is rather simple. Each command consists of a command name that has a length of three characters, e.g. MOV. It is followed by parameters that are separated by spaces. A question mark has to be appended if a return value is expected, e.g. POS? to read the current position in microns. The following commands¹ are used to initialize the controller and to move the actuator in steps of 1 μm in closed-loop operation – called *servo mode* by *Physik Instrumente*. Finally, the voltage is set to zero and the controller can be switched off.

```
CCL 1 advanced      # enable advanced mode
SPA 5 0x07000201    # limit rate of voltage to 5 V/s
VEL 1 0.5           # limit piezo velocity to 0.5 micron/s
SVA 1 10            # set voltage to 10 V
POS?                # query position
SVO 1 1             # enable servo mode
MOV 1 0             # goto zero position
MVR 1 1             # move by one micron
...
MOV 1 0             # goto zero position
SVO 1 0             # disable servo mode
SVA 1 0             # set voltage to 0 V
```

The speed of the change of the voltage is limited to few $\text{V}\cdot\text{s}^{-1}$ in open-loop operation to avoid abrupt movements of the piezo actuator. This parameter is only available in advanced mode at a certain address inside the volatile memory – thus the CCL command is necessary. The VEL command limits the velocity of the actuator in closed-loop operation. Further information are given in the manual of the controller [PI11].

A console application was written to automatically increase the position of the actuator during the acquisition of a series of radiographs. The application *XrmDirMon* is executed in a command prompt with two parameters: the file name of the current TXRM file² and the step size in μm . It basically monitors changes of the TXRM file. The actuator is moved by the given step size whenever a new radiograph is appended to the file. A typical call is:

```
#> XrmDirMon.exe "01 MicroDCB Test.txrm" 0.25
```

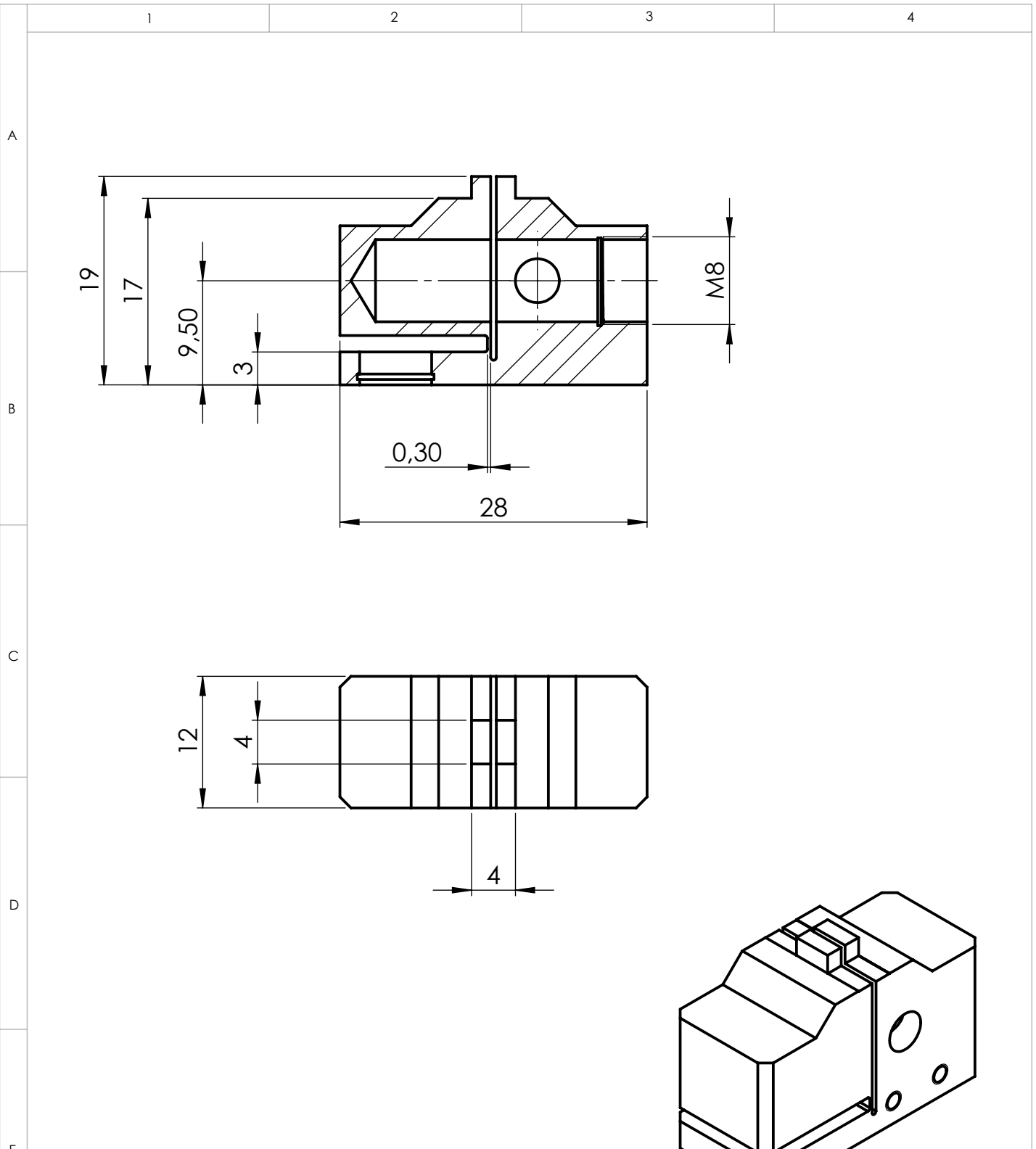
¹Comments in each line start with #. They are only given for explanation and not sent to the controller.

²This file type is used in *XMController* to store a series of radiographs in *averaging* or *tomography* mode.

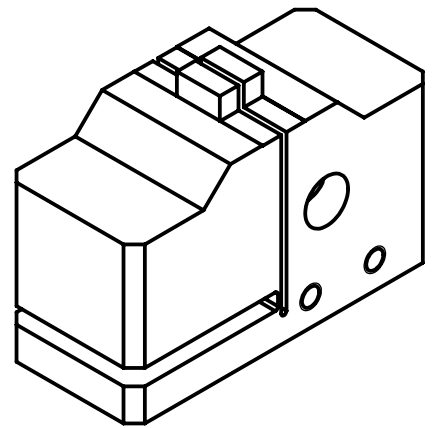
C. Technical drawings

- *MicroDCB tester* main part (1 page)
- MicroDCB sample holder (1 page)
- Pattern to cut multiple sample holders out of a sheet steel. (1 page)

Schutzvermerk nach DIN 34 beachten



Vereinfachte Zeichnung,
nicht für Fertigung vorgesehen



Allgemeintoleranzen DIN ISO 2768 - m K	Oberflächen DIN ISO 1302	Maßstab 2:1	A4	Position	Menge 1
---	-----------------------------	-------------	----	----------	---------

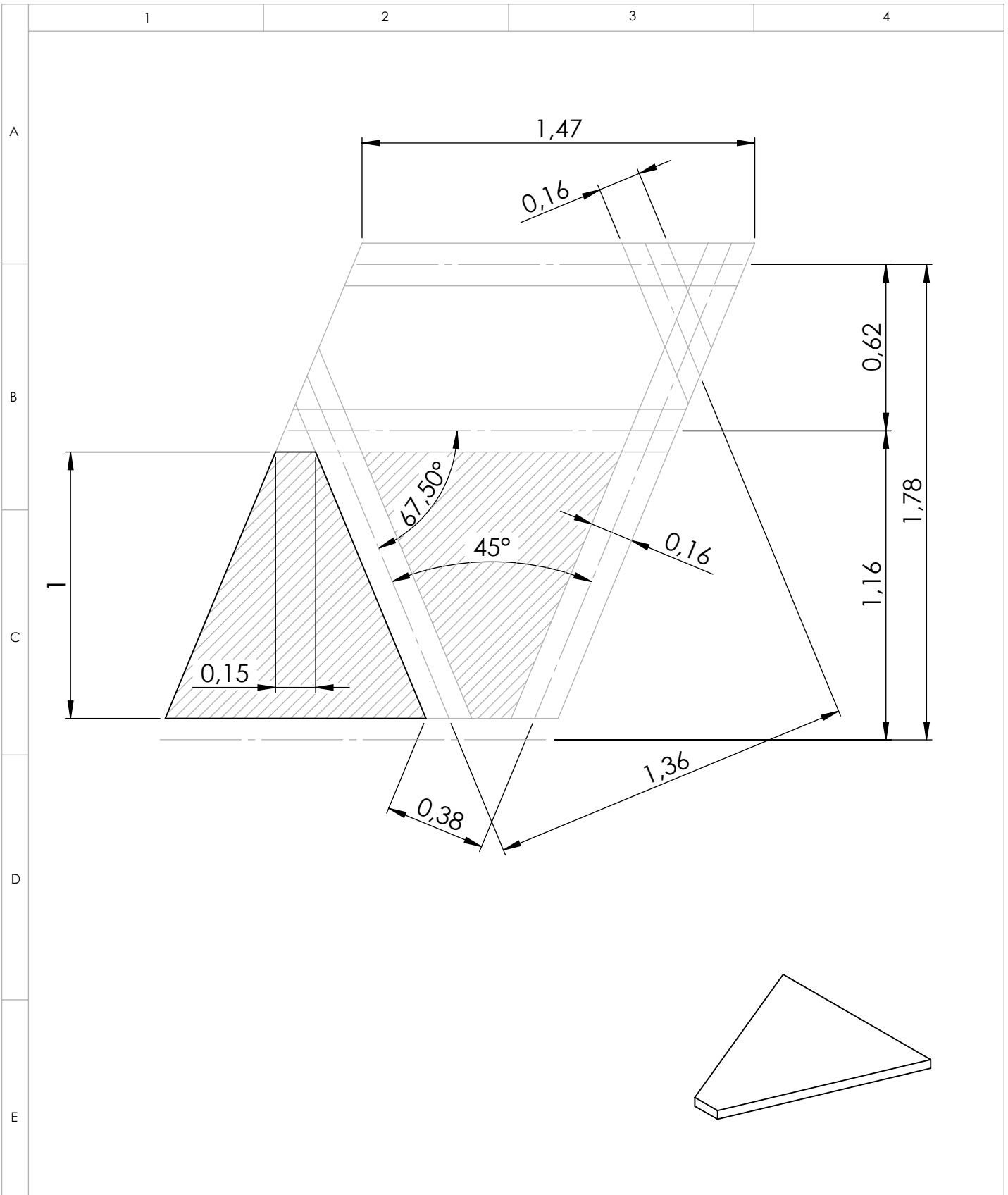
Form- und Lage- toleranzen DIN ISO 1101	Werkstück- kanten DIN 6784	Gewicht kg	Werkstoff 1.4404 (X2CrNiMo17-12-2)		
---	----------------------------------	---------------	---------------------------------------	--	--

A	keine Änderung			Datum	Name	MicroDCB Tester
				Bearb. 04.11.2013	S. Niese	
				Gepr.		
				Norm		


 DIN 6, Teil 1
 Proj. 1
 (ISO E)

Rev.	Änderung	Datum	Name	C:_Daten\Sven Niese\Konstruktion\Xradia\	Blatt 1	1 Bl.
------	----------	-------	------	---	------------	-------

Schutzvermerk nach DIN 34 beachten



Fraunhofer

IZFP

Allgemeintoleranzen
DIN ISO 2768 - m K

Oberflächen
DIN ISO 1302

Maßstab 50:1

A4

Position

Menge 1

Form- und Lage-
toleranzen
DIN ISO 1101

Werkstück-
kanten
DIN 6784

Gewicht
kg

Werkstoff
100 µm Stahlblech

A keine Änderung

Datum

Name

Bearb.

02.05.2011

S. Niese

Gepr.

Norm

MicroDCB Probenhalter



DIN 6, Teil 1
Proj. 1
(ISO E)

Blatt
1

Rev. Änderung

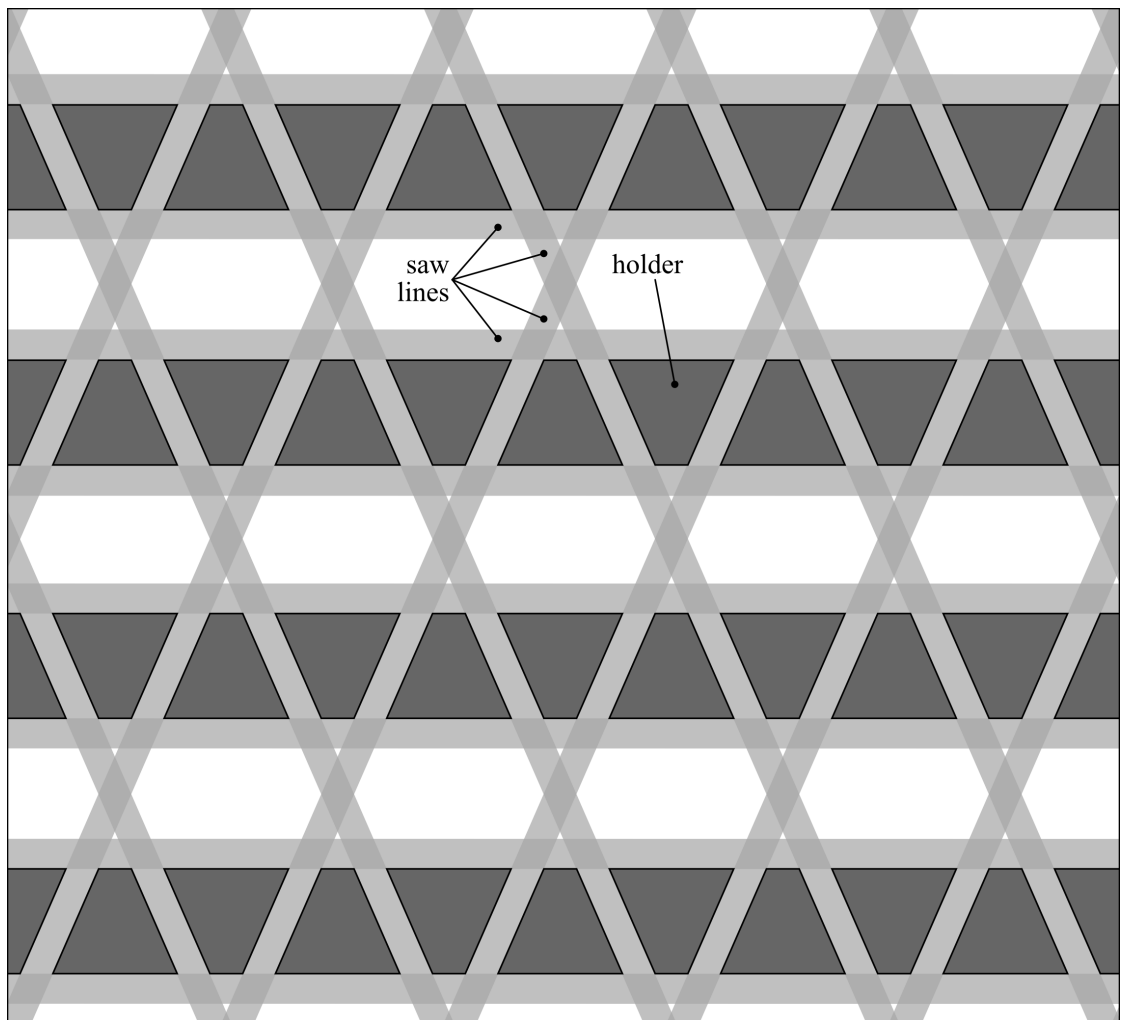
Datum

Name

1 Bl.

C. Technical drawings

Pattern to simultaneously cut multiple sample holders out of a sheet steel:



Bibliography

- [And+10] J. C. Andrews et al. “Nanoscale X-ray microscopic imaging of mammalian mineralized tissue”. In: *Microscopy and Microanalysis* 16.3 (2010), p. 327. DOI: 10.1017/S1431927610000231.
- [ATN50] *The siemens start test pattern ATN/XRESO-50HC was kindly provided by Prof. C. Schroer and Dr. J. Patommel (TU Dresden, Germany).*
- [Att99] D. Attwood. *Soft X-Rays and Extreme Ultraviolet Radiation*. Cambridge University Press, 1999.
- [Ban08] J. Banhart, ed. *Advanced Tomographic Methods in Materials Research and Engineering*. Oxford University Press, 2008. ISBN: 978-0-199-21324-5.
- [BR57] J. J. Benbow and F. C. Roesler. “Experiments on Controlled Fractures”. In: *Proceedings of the Physical Society. Section B* 70.2 (1957), p. 201. DOI: 10.1088/0370-1301/70/2/307.
- [Bra+13] S. Braun et al. “Multilayer Laue Lenses with Focal Length of 10 mm”. In: *Journal of Physics: Conference Series*. Vol. 425. 5. IOP Publishing, 2013, p. 052019. DOI: 10.1088/1742-6596/425/5/052019.
- [Bra06] S. S. Brandt. “Markerless Alignment in Electron Tomography”. In: *Electron Tomography*. Ed. by J. Frank. Springer New York, 2006, pp. 187–215. ISBN: 978-0-387-31234-7.
- [Bru+08] O. Brunke et al. “Comparison between x-ray tube-based and synchrotron radiation-based μ CT”. In: *Optical Engineering + Applications*. International Society for Optics and Photonics. 2008, 70780U–70780U.
- [BS07] K. J. Batenburg and J. Sijbers. “DART: a fast heuristic algebraic reconstruction algorithm for discrete tomography”. In: *IEEE International Conference on Image Processing, ICIP 2007*. Vol. 4. Sept. 2007, pp. IV133–IV136. DOI: 10.1109/ICIP.2007.4379972.
- [Bur13] G. Burkart. personal communication. 2013.
- [CH12] H. Czichos and M. Hennecke, eds. *HÜTTE – Das Ingenieurwissen*. 34th ed. Berlin: Springer, 2012. ISBN: 978-3-642-22849-0. DOI: 10.1007/978-3-642-22850-6.

Bibliography

- [Cha+89] P. G. Charalambides et al. “A Test Specimen for Determining the Fracture Resistance of Bimaterial Interfaces”. In: *Journal of Applied Mechanics* 56(1) (1989), pp. 77–82. DOI: 10.1115/1.3176069.
- [Che+11] T.-Y. Chen et al. “Full-field microimaging with 8 keV X-rays achieves a spatial resolutions better than 20 nm”. In: *Optics Express* 19.21 (2011), pp. 19919–19924. DOI: 10.1364/OE.19.019919.
- [Cnu+06] V. Cnudde et al. “Recent progress in X-ray CT as a geosciences tool”. In: *Applied Geochemistry* 21.5 (2006), pp. 826–832.
- [Con+08] R. Conley et al. “Wedged multilayer Laue lens”. In: *Review of Scientific Instruments* 79.5 (2008), pp. 053104–053104. DOI: 10.1063/1.2924209.
- [Con+11] R. P. Conley et al. “Zone compensated multilayer Laue lens and apparatus and method of fabricating the same”. English. WO 2011/142782 A9. 2011.
- [Dau+98] R. H. Dauskardt et al. “Adhesion and debonding of multi-layer thin film structures”. In: *Engineering Fracture Mechanics* 61.1 (1998), pp. 141–162.
- [Dau05] R. H. Dauskardt. *Delaminator – Adhesion Testing System*. Menlo Park, CA, USA, 2005.
- [DBR06] R. Davies, M. Burghammer, and C. Riekel. “An Overview of the ESRF’s ID13 Microfocus Beamline”. In: *Synchrotron Radiation in Natural Science* 5.1–2 (2006).
- [DBR09] R. J. Davies, M. Burghammer, and C. Riekel. “A combined microRaman and microdiffraction set-up at the European Synchrotron Radiation Facility ID13 beamline”. In: *Journal of Synchrotron Radiation* 16.1 (Jan. 2009), pp. 22–29. DOI: 10.1107/S0909049508034663.
- [Dör+13] F. Döring et al. “Sub-5 nm hard x-ray point focusing by a combined Kirkpatrick-Baez mirror and multilayer zone plate”. In: *Optics Express* 21.16 (2013), pp. 19311–19323.
- [DW14] G. Dhondt and K. Wittig. *CalculiX*. <http://www.calculix.de/>. 2014.
- [Fen+07] Y. Feng et al. “Nanofabrication of high aspect ratio 24 nm x-ray zone plates for x-ray imaging applications”. In: *Journal of Vacuum Science & Technology B: Microelectronics and Nanometer Structures* 25 (2007), p. 2004. DOI: 10.1116/1.2789447.
- [Gri+14] A. Grill et al. “Progress in the development and understanding of advanced low k and ultralow k dielectrics for very large-scale integrated interconnects—State of the art”. In: *Applied Physics Reviews* 1.1 (2014), p. 011306. DOI: 10.1063/1.4861876.
- [GS99] L. Giannuzzi and F. Stevie. “A review of focused ion beam milling techniques for TEM specimen preparation”. In: *Micron* 30.3 (1999), pp. 197–204.

- [Gul10a] E. Gullikson. *Filter Transmission*. http://henke.lbl.gov/optical_constants/filter2.html. 1995 – 2010.
- [Gul10b] E. Gullikson. *Index of Refraction*. http://henke.lbl.gov/optical_constants/getdb2.html. 1995 – 2010.
- [Gul10c] E. Gullikson. *X-Ray Attenuation Length*. http://henke.lbl.gov/optical_constants/atten2.html. 1995 – 2010.
- [Gut+13] P. Guttman et al. “Nanoscale spectroscopy and tomography with the HZB X-ray microscope: Applications in materials and life sciences”. In: *Journal of Physics: Conference Series*. Vol. 463. 1. IOP Publishing. 2013, p. 012032.
- [Hel+04] L. Helfen et al. “High-resolution three-dimensional imaging of flat objects by synchrotron-radiation computed laminography”. In: *Applied Physics Letters* 86 (2004), p. 071915. DOI: doi:10.1063/1.1854735.
- [Hen10] *Technisches Datenblatt – LOCTITE 435*. Henkel. Dec. 2010. URL: <http://tds.henkel.com/tds5/docs/435-DE.PDF>.
- [HGD93] B. L. Henke, E. Gullikson, and J. C. Davis. “X-Ray Interactions: Photoabsorption, Scattering, Transmission, and Reflection at $E = 50\text{--}30,000$ eV, $Z = 1\text{--}92$ ”. In: *Atomic Data and Nuclear Data Tables* 54.2 (1993), pp. 181–342. DOI: 10.1006/adnd.1993.1013.
- [HNK10] M. A. Hopcroft, W. D. Nix, and T. W. Kenny. “What is the Young’s Modulus of Silicon?” In: *Journal of Microelectromechanical Systems* 19.2 (2010), pp. 229–238. DOI: 10.1109/JMEMS.2009.2039697.
- [HOH03] O. Hemberg, M. Otendal, and H. Hertz. “Liquid-metal-jet anode electron-impact x-ray source”. In: *Applied Physics Letters* 83.7 (2003), pp. 1483–1485.
- [HS96] J. H. Hubbell and S. M. Seltzer. *Tables of X-ray Mass Attenuation Coefficients and Mass Energy-Absorption Coefficients from 1 keV to 20 MeV for Elements $Z = 1$ to 92 and 48 Additional Substances of Dosimetric Interest*. 1996. URL: <http://physics.nist.gov/PhysRefData/XrayMassCoef/cover.html>.
- [Hua+13] X. Huang et al. “11 nm hard X-ray focus from a large-aperture multilayer Laue lens”. In: *Scientific Reports* 3.3562 (2013). DOI: 10.1038/srep03562.
- [IBM07] IBM press room announcement. *IBM Airgap Microprocessor*. <http://www-03.ibm.com/press/us/en/presskit/21463.wss>. Viewed on Jan 22, 2014. May 3, 2007.
- [JD11] *The Nafion sample was kindly provided by R. Jia and R.H. Dauskardt (Stanford University, CA, USA)*.

Bibliography

- [Kam+03] N. Kamijo et al. “Microbeam of 100 keV x ray with a sputtered-sliced Fresnel zone plate”. In: *Review of Scientific Instruments* 74.12 (2003), pp. 5101–5104. DOI: 10.1063/1.1614882.
- [Kan+07] H. C. Kang et al. “Sectioning of multilayers to make a multilayer Laue lens”. In: *Review of Scientific Instruments* 78.4 (2007), pp. 046103–046103.
- [Kan+08] H. C. Kang et al. “Focusing of hard x-rays to 16 nanometers with a multilayer Laue lens”. In: *Applied Physics Letters* 92.22 (2008), pp. 221114–221114.
- [KB14] A. Kubec and S. Braun. personal communication. 2011 – 2014.
- [KB48] P. Kirkpatrick and A. V. Baez. “Formation of optical images by x-rays”. In: *Journal of the Optical Society of America* 38.9 (1948), pp. 766–773. DOI: 10.1364/JOSA.38.000766.
- [KD12] *The MEMS chip was kindly provided by B. Kaiser and C. Drabe (Fraunhofer IPMS Dresden, Department AMS, Germany).*
- [Kir74] J. Kirz. “Phase zone plates for x rays and the extreme UV”. In: *Journal of the Optical Society of America* 64.3 (1974), pp. 301–309. DOI: 10.1364/JOSA.64.000301.
- [KJ09] J. Kirz and C. Jacobsen. “The history and future of x-ray microscopy”. In: *J Phys Conf Ser.* Vol. 186. 012001. 2009, pp. 1–11.
- [KL41] A. Köhler and W. Loos. “Das Phasenkontrastverfahren und seine Anwendungen in der Mikroskopie”. In: *Naturwissenschaften* 29.4 (1941), pp. 49–61. DOI: 10.1007/BF01476460.
- [KN13] P. Krüger and S. Niese. *Bead Aligner*. Projection alignment plugin for ImageJ written in Java. In-house development of Fraunhofer IKTS-MD. 2013.
- [Koc+98] A. Koch et al. “X-ray imaging with submicrometer resolution employing transparent luminescent screens”. In: *Journal of the Optical Society of America A* 15.7 (1998), pp. 1940–1951. DOI: 10.1364/JOSAA.15.001940.
- [Koy+11] T. Koyama et al. “Development of Multilayer Laue Lenses; (2) Circular Type”. In: *The 10th International Conference on X-ray Microscopy*. Vol. 1365. AIP Publishing. 2011, pp. 100–103. DOI: 10.1063/1.3625314.
- [Krü+11] P. Krüger et al. “Improved Scanning Geometry to Collect 3D-Geometry Data in Flat Samples”. In: *The 10th International Conference on X-ray Microscopy*. Vol. 1365. 1. AIP Publishing. 2011, pp. 258–260.
- [Krü13] P. Krüger. *RayT*. Ray tracing software written in Java. In-house development of Fraunhofer IKTS-MD. 2013.
- [Krü14] P. Krüger. personal communication. 2010 – 2014.

- [KS88] A. C. Kak and M. Slaney. *Principles of Computerized Tomographic Imaging*. IEEE Press, 1988. URL: <http://www.slaney.org/pct/>.
- [Kub+14] A. Kubec et al. “Ptychography with Multilayer Laue Lenses”. In: *Journal of Synchrotron Radiation* (2014). submitted.
- [Lal+13] D. Laloum et al. “3D Void Imaging in Through Silicon Vias By X-Ray Nanotomography in An SEM”. In: *ISTFA 2013: Conference Proceedings*. ASM, 2013, pp. 7–11.
- [Lee+08] S. Lee et al. “Characterization of oxygen and nitrogen rapid thermal annealing processes for ultra-low-k SiCOH films”. In: *Journal of Materials Research* 23.3 (2008), pp. 856–861. DOI: 10.1557/JMR.2008.0106.
- [Len+99] B. Lengeler et al. “A microscope for hard x rays based on parabolic compound refractive lenses”. In: *Applied Physics Letters* 74.26 (1999), pp. 3924–3926. DOI: 10.1063/1.124225.
- [Liu+07] C. Liu et al. “Bonded Multilayer Laue Lens for focusing hard X-rays”. In: *Nuclear Instruments and Methods in Physics Research Section A: Accelerators, Spectrometers, Detectors and Associated Equipment* 582.1 (2007), pp. 123–125.
- [Liu+13] S. Liu et al. “Measuring the fracture resistance of hard coatings”. In: *Applied Physics Letters* 102.17 (2013), pp. 171907–171907.
- [LLS04] M. W. Lane, X. H. Liu, and T. M. Shaw. “Environmental effects on cracking and delamination of dielectric films”. In: *IEEE Transactions on Device and Materials Reliability* 4.2 (2004), pp. 142–147. DOI: 10.1109/TDMR.2004.829123.
- [LRK10] T. Liese, V. Radisch, and H. Krebs. “Fabrication of multilayer Laue lenses by a combination of pulsed laser deposition and focused ion beam”. In: *Review of Scientific Instruments* 81 (2010), p. 073710.
- [Mas+04] J. Maser et al. “Multilayer Laue lenses as high-resolution x-ray optics”. In: *Proc. SPIE*. Vol. 5539. 1. 2004, pp. 185–194. DOI: 10.1117/12.560046.
- [MB06] H. Mai and S. Braun. “Metal based thin films for electronics”. In: ed. by K. Wetzig and C. M. Schneider. Wiley-VCH, 2006. Chap. Multilayers for X-ray optical purposes, pp. 309–332. DOI: 10.1002/3527602534.ch2.
- [MG13] A. P. Merkle and J. Gelb. “The Ascent of 3D X-ray Microscopy in the Laboratory”. In: *Microscopy Today* 21.02 (2013), pp. 10–15.
- [Mim+09] H. Mimura et al. “Breaking the 10 nm barrier in hard-X-ray focusing”. In: *Nature Physics* 6.2 (2009), pp. 122–125.
- [Mon57] M. Montel. “The X-ray microscope with catamegonic roof-shaped objective”. In: *X-ray Microscopy and Microradiography* (1957), pp. 177–185.

Bibliography

- [Mor+10] J. Morais et al. “The double cantilever beam test applied to mode I fracture characterization of cortical bone tissue”. In: *Journal of the Mechanical Behavior of Biomedical Materials* 3.6 (2010), pp. 446–453. DOI: 10.1016/j.jmbbm.2010.04.001.
- [MS92] J. Maser and G. Schmahl. “Coupled wave description of the diffraction by zone plates with high aspect ratios”. In: *Optics Communications* 89.2 (1992), pp. 355–362. DOI: 10.1016/0030-4018(92)90182-Q.
- [Mun10] D. H. Munro. *Yorick*. <http://yorick.github.com>. Yorick is an interpreted programming language for scientific simulations or calculations, postprocessing or steering large simulation codes, interactive scientific graphics, and reading, writing, or translating large files of numbers. 2010.
- [Mur+] D. B. Murphy et al. *Introduction to Phase Contrast Microscopy*. <http://www.microscopyu.com/articles/phasecontrast/phasemicroscopy.html>. Viewed on Apr 17, 2014.
- [Naz+13] E. Nazaretski et al. “Performance and characterization of the prototype nm-scale spatial resolution scanning multilayer Laue lenses microscope”. In: *Review of Scientific Instruments* 84 (2013), p. 033701.
- [Nie+14a] S. Niese et al. “Fabrication of Customizable Wedged Multilayer Laue Lenses by Adding a Stress Layer”. In: *Thin Solid Films* (2014). DOI: 10.1016/j.tsf.2014.02.095.
- [Nie+14b] S. Niese et al. “Full-field X-ray microscopy with crossed partial multilayer Laue lenses”. In: 22.17 (2014), pp. 20008–20013.
- [Ote+08] M. Otendal et al. “A 9 keV electron-impact liquid-gallium-jet x-ray source”. In: *Review of Scientific Instruments* 79.1 (2008), pp. 016102–016102.
- [Pat+12] J. Patommel et al. *Adiabatically Focusing Lenses (AFL)*. Tech. rep. DESY annual report, 2012. URL: http://photon-science.desy.de/annual_report/files/2012/20122257.pdf.
- [PI11] *PI E-709 manual*. Physik Instrumente GmbH & Co. KG. 2011.
- [Rad17] J. Radon. “Über die Bestimmung von Funktionen durch ihre Integralwerte längs gewisser Mannigfaltigkeiten ein”. In: *Berichte über die Verhandlungen der Königlich-Sächsischen Gesellschaft der Wissenschaften zu Leipzig* 69 (1917), pp. 262–277.
- [Rar+90] H. Rarback et al. “Coherent radiation for x-ray imaging—the soft x-ray undulator and the X1A beamline at the NSLS”. In: *Journal of X-ray Science and Technology* 2.4 (1990), pp. 274–296. DOI: 10.1016/0895-3996(90)90017-G.
- [Ras13] W. Rasband. *ImageJ*, U. S. National Institutes of Health, Bethesda, Maryland, USA. <http://imagej.nih.gov/ij/>. 1997–2013.

- [RBD10] C. Riekkel, M. Burghammer, and R. Davies. “Progress in micro- and nano-diffraction at the ESRF ID13 beamline”. In: *IOP Conference Series: Materials Science and Engineering*. Vol. 14. 1. IOP Publishing. 2010, p. 012013.
- [Reh+09] S. Rehbein et al. “Ultrahigh-resolution soft-X-ray microscopy with zone plates in high orders of diffraction”. In: *Physical Review Letters* 103.11 (2009), p. 110801. DOI: 10.1103/PhysRevLett.103.110801.
- [RHB08] J. Rösler, H. Harders, and M. Bäker. *Mechanisches Verhalten der Werkstoffe*. 3. Vieweg+Teubner, 2008.
- [RNS82] D. Rudolph, B. Niemann, and G. Schmahl. “Status of the sputtered sliced zone plates for x-ray microscopy”. In: *1981 Brookhaven Conferences*. International Society for Optics and Photonics. 1982, pp. 103–105.
- [Rön98] W. C. Röntgen. “Über eine neue Art von Strahlen”. In: *Annalen der Physik* 300.1 (1898), pp. 1–11.
- [Ruh+12] A. Ruhlandt et al. “A combined Kirkpatrick-Baez mirror and multilayer lens for sub-10 nm x-ray focusing”. In: *AIP Advances* 2.1 (2012), pp. 012175–012175.
- [SA10] A. Sakdinawat and D. Attwood. “Nanoscale X-ray imaging”. In: *Nature Photonics* 4.12 (2010), pp. 840–848.
- [San10] C. Sander. “Methodische Untersuchungen zur Rissausbreitung in Metall-Dielektrikum-Schichtstrukturen für die Mikroprozessor-Technologie”. MA thesis. Technische Universität Berlin, Oct. 2010.
- [San14] C. Sander. personal communication. 2011 – 2014.
- [Sch+03] C. Schroer et al. “Nanofocusing parabolic refractive x-ray lenses”. In: *Applied Physics Letters* 82.9 (2003), pp. 1485–1487. DOI: 10.1063/1.1556960.
- [Sch+05a] G. Schena et al. “Detecting microdiamonds in kimberlite drill-hole cores by computed tomography”. In: *International Journal of Mineral Processing* 75.3 (2005), pp. 173–188.
- [Sch+05b] C. Schroer et al. “Hard x-ray nanoprobe based on refractive x-ray lenses”. In: *Applied Physics Letters* 87.12 (2005), p. 124103. DOI: 10.1063/1.2053350.
- [Sch+10a] C. G. Schroer et al. “Hard X-ray nanoprobe at beamline P06 at PETRA III”. In: *Nuclear Instruments and Methods in Physics Research Section A: Accelerators, Spectrometers, Detectors and Associated Equipment* 616.2 (2010), pp. 93–97.
- [Sch+10b] A. Schropp et al. “Hard x-ray nanobeam characterization by coherent diffraction microscopy”. In: *Applied Physics Letters* 96.9 (2010), pp. 091102–091102-3. DOI: 10.1063/1.3332591.

Bibliography

- [Sch06] C. Schroer. “Focusing hard x rays to nanometer dimensions using Fresnel zone plates”. In: *Physical Review B* 74.3 (2006), p. 033405. DOI: 10.1103/PhysRevB.74.033405.
- [Sch97] G. Schneider. “Zone plates with high efficiency in high orders of diffraction described by dynamical theory”. In: *Applied Physics Letters* 71.16 (1997), pp. 2242–2244. DOI: 10.1063/1.120069.
- [Sha+04] D. Shamiryman et al. “Low-k dielectric materials”. In: *Materials Today* 7.1 (2004), pp. 34–39. ISSN: 1369-7021. DOI: 10.1016/S1369-7021(04)00053-7.
- [SL05] C. G. Schroer and B. Lengeler. “Focusing hard X rays to nanometer dimensions by adiabatically focusing lenses”. In: *Physical Review Letters* 94.5 (2005), p. 054802. DOI: 10.1103/PhysRevLett.94.054802.
- [Spi94] M. Spies. “Transducer-modeling in general transversely isotropic media via point-source-synthesis: Theory”. In: *Journal of Nondestructive Evaluation* 13.2 (1994), pp. 85–99. DOI: 10.1007/BF00730959.
- [SRG88] G. Schmahl, D. Rudolph, and P. Guttman. “Phase contrast X-ray microscopy—experiments at the BESSY storage ring”. In: *X-ray microscopy II*. Springer, 1988, pp. 228–232. DOI: 10.1007/978-3-540-39246-0_40.
- [The11] P. Thevenaz. *TurboReg*. <http://bigwww.epfl.ch/thevenaz/turboreg/>, EPFL Biomedical Imaging Group. The purpose of this plugin is to register—in other words, to align or to match—two images, one of them being called the source image and the other the target image. July 2011.
- [Tho+01] A. Thompson et al. *X-ray data booklet*. Lawrence Berkeley National Laboratory, University of California, 2001.
- [Tka+06] A. Tkachuk et al. “High-resolution x-ray tomography using laboratory sources”. In: *Optics & Photonics*. International Society for Optics and Photonics. 2006, pp. 63181D-1–63181D-8. DOI: 10.1117/12.682383.
- [TRU98] P. Thévenaz, U. Ruttimann, and M. Unser. “A Pyramid Approach to Sub-pixel Registration Based on Intensity”. In: *IEEE Transactions on Image Processing* 7.1 (Jan. 1998), pp. 27–41. DOI: 10.1109/83.650848.
- [Wan+12] J. Wang et al. “Automated markerless full field hard x-ray microscopic tomography at sub-50 nm 3-dimension spatial resolution”. In: *Applied Physics Letters* 100.14 (2012), pp. 143107–143107. DOI: 10.1063/1.3701579.
- [WBH82] J. Whitney, C. Browning, and W. Hoogsteden. “A double cantilever beam test for characterizing mode I delamination of composite materials”. In: *Journal of Reinforced Plastics and Composites* 1.4 (1982), pp. 297–313. DOI: 10.1177/073168448200100402.

- [Wer+09] S. Werner et al. “Towards stacked zone plates”. In: *Journal of Physics: Conference Series*. Vol. 186. 1. IOP Publishing. 2009, p. 012079. DOI: 10.1088/1742-6596/186/1/012079.
- [Wit07] P. J. Withers. “X-ray nanotomography”. In: *Materials Today* 10.12 (2007), pp. 26–34. DOI: 10.1016/S1369-7021(07)70305-X.
- [Wu+07] K. S. Wu et al. “Time-dependant intercellular delamination of human stratum corneum”. In: *Journal of Materials Science* 42.21 (2007), pp. 8986–8994.
- [Yan+07] H. Yan et al. “Takagi-Taupin description of x-ray dynamical diffraction from diffractive optics with large numerical aperture”. In: *Physical Review B* 76.11 (2007), p. 115438. DOI: 10.1103/PhysRevB.76.115438.
- [Yan+10] H. Yan et al. “Multilayer Laue lens: a path toward one nanometer X-ray focusing”. In: *X-ray Optics and Instrumentation 2010* (2010). DOI: 10.1155/2010/401854.
- [Yan+11] H. Yan et al. “Two dimensional hard x-ray nanofocusing with crossed multilayer Laue lenses”. In: *Optics Express* 19.16 (2011), pp. 15069–15076. DOI: 10.1364/OE.19.015069.
- [YC12] H. Yan and Y. S. Chu. “Optimization of multilayer Laue lenses for a scanning X-ray microscope”. In: *Journal of Synchrotron Radiation* 20.1 (2012), pp. 89–97.
- [YDW07] W. Yun, F. W. Duerer, and Y. Wang. “X-ray microscope capillary condenser system”. US 7,170,969 B1. 2007.
- [Zer35] F. Zernike. “Das Phasenkontrastverfahren bei der mikroskopischen Beobachtung”. In: *Zeitschrift für technische Physik* 16 (1935), pp. 454–457.
- [Zer55] F. Zernike. “How I discovered phase contrast”. In: *Science* 121.3141 (1955), pp. 345–349.

List of publications

Papers

- [Sven Niese](#), Michael Hecker, Romy Liske, Yvonne Ritz, Ehrenfried Zschech, Henry Wojcik, Johann Bartha, Z. Wu, and Paul S. Ho. Assessment of mechanical properties of nanoscale structures for microprocessor manufacturing. In *STRESS-INDUCED PHENOMENA IN METALLIZATION: 11th International Workshop*, volume 1300, pages 147–152. AIP Publishing, 2010.
- [Sven Niese](#), Peter Krüger, and Ehrenfried Zschech. NanoXCT – A high-resolution technique for TSV characterization. In *STRESS MANAGEMENT FOR 3D ICS USING THROUGH SILICON VIAS: International Workshop on Stress Management for 3D ICs Using Through Silicon Vias*, volume 1378, pages 168–173. AIP Publishing, 2011.
- [Sven Niese](#), Peter Krüger, Adam Kubec, Roman Laas, Peter Gawlitza, Kathleen Melzer, Stefan Braun, and Ehrenfried Zschech. Fabrication of customizable wedged multilayer Laue lenses by adding a stress layer. *Thin Solid Films*, 2014. DOI:10.1016/j.tsf.2014.02.095.
- [Sven Niese](#), Peter Krüger, Adam Kubec, Stefan Braun, Jens Patommel, Christian G. Schroer, and Ehrenfried Zschech. Full-field x-ray microscopy with crossed partial multilayer Laue lenses. *Optics Express*, 2014. Accepted.

Papers (co-author)

- Peter Krüger, [Sven Niese](#), Ehrenfried Zschech, Jeff Gelb, and Michael Feser. Improved scanning geometry to collect 3D-geometry data in flat samples. *XRM 2010 proceedings*, 2010.
- John U. Knickerbocker, Lay Wai Kong, [Sven Niese](#), Alain Diebold, and Ehrenfried Zschech. *Advanced Interconnects for ULSI Technology*, chapter 3D Interconnect Technology, pages 437–490. WILEY, 2012.
- Jens Patommel, Susanne Hönig, Stephan Ritter, Maria Scholz, Frank Seiboth, Christian G. Schroer, Adam Kubec, [Sven Niese](#), and A. Jahn. Adiabatically focusing lenses (AFL). Technical report, DESY annual report, 2012.

List of publications

- Kong Boon Yeap, Malgorzata Kopycinska-Müller, Ude D. Hangen, Claudio Zambaldi, René Hübner, Sven Niese, and Ehrenfried Zschech. Nanometer deformation of elastically anisotropic materials studied by nanoindentation. *Philosophical Magazine*, 92(25-27):3142–3157, 2012.
- Stefan Braun, Adam Kubec, Maik Menzel, Sven Niese, Peter Krüger, Frank Seiboth, Jens Patommel, and Christian G. Schroer. Multilayer Laue lenses with focal length of 10 mm. In *Journal of Physics: Conference Series*, volume 425, page 052019. IOP Publishing, 2013.
- Kong Boon Yeap, Martin Gall, Christoph Sander, Sven Niese, Zhongquan Liao, Yvonne Ritz, Rüdiger Rosenkranz, Uwe Mühle, Jürgen Gluch, Ehrenfried Zschech, et al. An experimental methodology for the in-situ observation of the time-dependent dielectric breakdown mechanism in copper/low-k on-chip interconnect structures. In *Reliability Physics Symposium (IRPS), 2013 IEEE International*, pages 2F.1.1 – 2F.1.5. IEEE, 2013.
- Adam Kubec, Stefan Braun, Sven Niese, Peter Krüger, Jens Patommel, Michael Hecker, and Christian G. Schroer. Ptychography with multilayer Laue lenses. *Journal of Synchrotron Radiation*, 2014. Submitted.

Patents

- Sven Niese. Keilförmige mehrschichtige Laue-Linse und Verfahren zu ihrer Herstellung, DE102013005845B3, 2014.

Oral presentations

- Sven Niese, Alex Hsing, Jeff Gelb, Kevin Fahey, Reinhold H. Dauskardt, Peter Krüger, and Ehrenfried Zschech. In-situ dual cantilever beam test with tomographic access in x-ray microscopy. 3D Microstructure Meeting, Saarbrücken, Germany, 02–04 November 2011.
- Sven Niese, Rüdiger Rosenkranz, Yvonne Ritz, Peter Krüger, Ehrenfried Zschech. Analytical techniques for process development and failure analysis of 3D TSV structures. MicroCar 2013, Leipzig, Germany, 25–26 February 2013.
- Sven Niese, Adam Kubec, Peter Krüger, Stefan Braun, Andreas Leson, and Ehrenfried Zschech. Fabrication and mechanical behavior of multilayer Laue lenses. Nanoscale Multilayers '13, Madrid, Spain, 01–04 October 2013.
- Sven Niese, Alex Hsing, Jeff Gelb, Arno Merkle, Kevin Fahey, Reinhold H. Dauskardt, Peter Krüger, and Ehrenfried Zschech. In-situ observations of crack propa-

gation in patterned structures using x-ray microscopy. MRS Fall Meeting, Boston, USA, 01–06 December 2013.

Poster presentations

- Sven Niese, Peter Guttman, Lay Wai Kong, Peter Krüger, Gerd Schneider, Alain Diebold, and Ehrenfried Zschech. Through silicon via studies with SR and lab-based transmission x-ray microscopy. 2nd HZB-Joint User's Meeting, Berlin, Germany, 09–10 December 2010.
- Sven Niese, Peter Krüger, Stefan Braun, Jürgen Wolf, and Ehrenfried Zschech. TSV imaging applying lab-based nano transmission x-ray microscopy for 3D IC integration. 8th International Nanotechnology Conference, Tsukuba, Japan, 08–11 May 2012.
- Sven Niese, Alex Hsing, Jeff Gelb, Peter Krüger, Kevin Fahey, Reinhold H. Dauskardt, and Ehrenfried Zschech. In-situ dual cantilever beam test in x-ray microscopy based computed tomography. Nanofair 2012, Dresden, Germany, 12–13 June 2012.
- Sven Niese, Peter Krüger, Adam Kubec, Stefan Braun, Jens Patommel, Christian G. Schroer, and Ehrenfried Zschech. Multilayer Laue lenses for full-field hard x-ray microscopy. 22nd International Congress on X-Ray Optics and Microanalysis (ICXOM), Hamburg, Germany, 02–06 September 2013.
- Sven Niese, Alex Hsing, Jeff Gelb, Kevin Fahey, Reinhold H. Dauskardt, Peter Krüger, and Ehrenfried Zschech. Three-dimensional crack visualization in patterned layer structures by in-situ x-ray microscopy. Nanoscale Multilayers '13, Madrid, Spain, 01–04 October 2013.

Curriculum Vitae

Personal information

Date of birth	April 28 th 1985
Place of birth	Radebeul, Germany
Nationality	German

Education and employment

02/2010 – 05/2014	PhD studies BTU Cottbus, Chair Applied Physics and Sensors Fraunhofer IZFP-D, Division Micro- and Nano-Analysis
10/2004 – 01/2010	Study of materials science, TU Dresden
09/2003 – 06/2004	Civilian service
08/1991 – 06/2003	School, degree: Abitur

Danksagung

Ich möchte mich an dieser Stelle bei allen Betreuern, Kollegen und Freunden bedanken, die zum Gelingen dieser Arbeit beigetragen haben. Prof. Dr. Dieter Schmeißer danke ich für die Möglichkeit, an der BTU Cottbus-Senftenberg am Lehrstuhl für angewandte Physik/Sensorik zu promovieren. Prof. Dr. Ehrenfried Zschech danke ich insbesondere für die wissenschaftliche Betreuung dieser Arbeit, die Möglichkeit am Fraunhofer IZFP-D und später am DCN, TU Dresden zu arbeiten, sowie die Gelegenheiten, verschiedenste Dinge auszuprobieren, zu unterstützen und umzusetzen. Dr. Gerd Schneider vom Helmholtz Zentrum Berlin danke ich für die Diskussionen zur Vollfeldabbildung mit Multilayer-Laue-Linsen.

Dr. Peter Krüger vom IKTS-MD danke ich für die wissenschaftlich-technische Betreuung auf dem Gebiet der Röntgentechniken, welche unter anderem die zur Verfügung gestellten Quellcodes für ImageJ und Yorick und von RayT umfasst, sowie diverse Diskussionen und Anregungen zur Arbeit mit dem Röntgenmikroskop, der Mikro-CT und beim Programmieren und Schreiben mit einschließt. Yvonne Standke hat mich wann immer nötig im Präparationslabor und an der FIB unterstützt. Björn Fischer, Sven Reinert und Sascha Naumann waren im Röntgenlabor stets eine große Hilfe. Das gleiche gilt für Dr. Bernd Köhler, Dr. Uwe Mühle, Dr. Rüdiger Rosenkranz und Dr. Jürgen Gluch für die Arbeit an REM/FIB, die Unterstützung mit TEM und Diskussionen, sowie Jürgen Michauk und Susan Walter bei der Nutzung der Wafersäge. Dr. Martin Gall war u.a. bei Fragen zur Mikroelektronik immer der richtige Ansprechpartner; gleiches gilt für Christoph Sander bzgl. der Bruchmechanik und anderer Themen, sowie Edgar Schubert, Frank Macher, Elke Fischer und Christian Thieme bzgl. der Konstruktion und Fertigung von Bauteilen in der Werkstatt. Conrad Jung und Roman Laas haben mich als HiWis unterstützt. Weiterhin sei allen Kollegen für die angenehme Atmosphäre im Institut und gelegentliche, abwechslungsreiche Aufgaben und Diskussionen gedankt. Tatjana Heller, Martina Reich, Birgit Rüger, Madleen Frenzel, Dr. Lothar Haupt und Julia Rothe waren administrativ immer eine große Hilfe.

Die Entwicklung der Multilayer-Laue-Linsen erfolgte in enger Kooperation mit dem Fraunhofer IWS Dresden. Dr. Stefan Braun, Adam Kubec und Kathleen Melzer haben die Multischichten hergestellt, Synchrotron-Messzeiten organisiert und waren immer für Diskussionen und Vorschläge bzgl. der Schichtherstellung und der weiteren Prozessierung zu den eigentlichen Linsenelementen verfügbar. Vielen Dank dafür. Peter Gawlitza und Christoph Gruhne haben die Testbeschichtungen für die wedged MLL schnell und unkompliziert erledigt. Maximilian Rühl (IWS), Jens Patommel und Stephan Rit-

Danksagung

ter (TU Dresden) danke ich für die Unterstützung der Messzeiten. Prof. Dr. Christian Schroer danke ich für Diskussionen über Röntgenoptik und die generelle Unterstützung der Messzeiten und Labormessungen durch seine Arbeitsgruppe. Dr. Gerald Falkenberg, Dr. Gerd Wellenreuther und Ulrike Bösenberg seitens DESY, Beamline P06, sowie Dr. Manfred Burghammer und Michael Sztucki seitens ESRF, ID13 haben die Synchrotron-Messungen – teils bis spät in die Nacht – gut unterstützt. Dr. Michael Hecker von Globalfoundries Dresden danke ich für die Unterstützung und Zusammenarbeit im CoolAnalytics-Projekt. Prof. Dr. Jozef Keckes und Mario Stefanelli (Uni Leoben) haben uns eine Hartschicht-Probe für erste Nanobeugungsmessungen mit MLLs zur Verfügung gestellt und die Daten ausgewertet.

Unter anderem Dr. Kevin Fahey, Dr. Michael Feser, Jeff Gelb, Dean Hunt, Luke Hunter, Naomi Kotwal, Alan Lyon, Marty Leibowitz, Jay Steele, Dr. Claus Flachenecker, Daren Livett und Adrian Poteet von Xradia sei für die umfangreiche Unterstützung während des halbjährigen Aufenthaltes in der San Francisco Bay Area bei Xradia gedankt. In dieser Zeit sind die Prototypen des MicroDCB-Testers und eines kleinen Ofens entstanden und ich habe einiges in der Arbeit mit der NanoXCT dazugelernt. Ebenso danke ich Prof. Dr. Reinhold H. Dauskardt, Alex Hsing, Krysta Biniek und Ruiliang Jia von der Stanford University für die fachliche Unterstützung während des Aufenthaltes und insbesondere für die Idee, den MicroDCB-Test in Angriff zu nehmen.

Dr. Markus Löffler, Alexander Tahn, Linda Kriusk, Sayanti Banerjee und Jin Huang sei für die abschließende Zeit am DCN der TU Dresden gedankt. Ebenso danke ich Reiner Dietsch, Thomas Holz, Dr. Daniela Rogler und Bartek Lechowski von der AXO DRESDEN GmbH für die Diskussionen über eine angepasste Beleuchtungsoptik für MLL mittels Spiegeloptiken sowie Dr. Stephan Kleindiek, Klaus Schock und Jochen Sterr von Kleindiek Nanotechnik GmbH für die Unterstützung bei den ersten Experimenten zur in-situ Instrumentierung in REM und XRM. Dr. Günter Burkart, ECEMP, TU Dresden, danke ich für die Informationen bzgl. der Klebstoffe für den MicroDCB-Test.

Oliver Marbach, Dr. Peter Krüger, Adam Kubec und Christoph Sander danke ich zudem für das Korrekturlesen einzelner Kapitel.

Ich möchte mich weiterhin für die Förderung der Entwicklung der MLL für Laboranwendungen beim Bundesministerium für Bildung und Forschung (BMBF) bedanken, das die Untersuchungen im Rahmen des CoolSilicon-Clusters über das Projekt CoolAnalytics (SAB 75702/2583) gefördert hat.

Ich danke meinen Eltern, meiner Schwester und allen anderen Menschen aus meinem Familien- und Freundeskreis für die Unterstützung vor und während der Promotion.

Erklärung

Hiermit versichere ich, dass ich die vorliegende Arbeit ohne unzulässige Hilfe Dritter und ohne Benutzung anderer als der angegebenen Hilfsmittel angefertigt habe. Die aus fremden Quellen direkt oder indirekt übernommenen Gedanken sind als solche kenntlich gemacht. Die Arbeit wurde bisher weder im Inland noch im Ausland in gleicher oder ähnlicher Form einer anderen Prüfungsbehörde vorgelegt.

Hiermit erkläre ich, dass ich die bestehende Prüfungsordnung der Fakultät für Mathematik, Naturwissenschaften und Informatik der Brandenburgischen Technischen Universität Cottbus-Senftenberg anerkenne.

Es haben zuvor keine erfolglosen Promotionsversuche stattgefunden. Die Veröffentlichung der Dissertation verletzt keine bestehenden Schutzrechte.

Die vorliegende Arbeit wurde im Zeitraum von Februar 2010 bis Mai 2014 am Fraunhofer-Instituts für Zerstörungsfreie Prüfverfahren, Institutsteil Dresden IZFP-D – seit Januar 2014 Fraunhofer-Institut für Keramische Technologien und Systeme, Institutsteil Materialdiagnostik IKTS-MD – unter der wissenschaftlichen Betreuung von Herrn Prof. Dr. Dieter Schmeißer (BTU Cottbus-Senftenberg) und Herrn Prof. Dr. Ehrenfried Zschech (Fraunhofer IZFP-D/IKTS-MD) angefertigt.

Dresden, den 11.08.2014

Sven Niese